UNIVERSITY OF LIVERPOOL

Automatic Detection, Sizing and Characterisation of Weld Defects Using Ultrasonic Time-of-Flight Diffraction

Thesis submitted in accordance with the requirements of
the University of Liverpool for the degree of Doctor in Philosophy

By

Ali AbdulIlah Al-Ataby

June 2012

Abstract

Ultrasonic time-of-flight diffraction (TOFD) is known as a reliable non-destructive testing technique for weld inspection in steel structures, providing accurate flaw positioning and sizing. Despite all its good features, TOFD data interpretation and reporting are still performed manually by skilled inspectors and interpretation software operators. This is a cumbersome and error-prone process, leading to inevitable delay and inconsistency. The quality of the collected TOFD data is another issue that may introduce a host of error to the overall interpretation process. Manual interpretation focuses only on the compression waves portion of the collected TOFD data and overlooks the mode-converted waves region and considers it redundant. This region may provide useful and accurate flaw sizing and classification information when there is uncertainty or ambiguity due to the nature of the collected data or the type of flaw, and can reduce the number of supplementary (parallel) B-scans by utilising the (longitudinal) D-scans only. The automation of data processing in TOFD is required to minimise time and error and towards building a comprehensive computer-aided TOFD interpretation tool that can aid human operators.

This project aims at proposing interpretation algorithms to size and characterise flaws automatically and accurately using data acquired from D-scans only. In order to achieve this, a number of novel data manipulation and processing techniques have been specifically developed and adapted to expose the information in the mode-converted waves region. In addition, several multi-resolution approaches employing the Wavelet transform and texture analysis have been used in flaw detection and for de-noising and enhancing quality of the collected data.

Performance of the developed algorithms and the results of their application have been promising in terms of speed, accuracy and consistency when compared to human interpretation by an expert operator, using the compression waves portion of the acquired data. This is expected to revolutionise the TOFD data interpretation and be in favour of a real-time processing of large volumes of data. It is highly anticipated that the research findings of this project will increase significantly the reliance on D-scans to obtain high sizing accuracy without the need to perform further B-scans. The overall inspection and interpretation time and cost will therefore be reduced significantly.

To my mother Likaa Al-Samara'i, father Abdulilah Al-Ataby, brothers Dr Ammar and Hamza Al-Ataby, sister Eng Aisha Al-Ataby, wife Ayat Al-Qaysi and sons Mohammed and Hassan Al-Ataby.

Acknowledgements

I would like to express my sincere gratitude and gratefulness to my supervisor Dr Waleed Al-Nuaimy for his valuable supervision and support throughout the course of this work. I am especially thankful to E.ON Engineering, UK, for funding and supporting this work and to Dr Colin Brett in particular for his encouragement.

Special thanks and appreciation are also extended to all members of my family for their encouragement and patience, and to anyone who supported me during the work in this project.

Finally, I would like to dedicate my humble piece of work to the Department of Electrical Engineering and Electronics, University of Liverpool, as a symbol of appreciation and gratitude.

Contents

List of Figures

List of Tables

Acronyms

ADC	Analogue-to-digital converter
ANN	Artificial neural network
CA	Classification accuracy
CI	Computational intelligence
CM	Confusion matrix
CP	Classification precision
CT	Computerised tomography
CWT	Continuous Wavelet transform
dB	Decibel
DWT	Discrete Wavelet transform
ESIT	Embedded signal identification technique
FCMI	Fuzzy c-mean iterative algorithm
FCR	False call rate
FV	Feature vector
GLCM	The grey-level co-occurrence matrix
GUI	Graphical user interface
IC	Internal crack
LC	Lower crack
LOF	Lack of fusion
LOP	Lack of penetration
MRA	Multi-resolution analysis
NDE	Non-destructive evaluation
NDT	Non-destructive testing
NN	Neural network

NPI	Number of positive islands
OAA	One-against-all
OAO	One-against-one
PA	Phased array
PCS	Probe centre separation
PE	Pulse echo
POD	Probability of detection
PO	Porosity
PRF	Pulse repetition frequency
PSCT	Point source correlation technique
QA	Quality assurance
QP	Quadratic programming
RA	Relative area
SNR	Signal-to-noise ratio
SL	Slag line
SLT	Statistical learning theory
SV	Support vectors
SVM	Support vector machines
TL	Threadlike
TNI	Total number of islands
TOFD	Time-of-flight diffraction
UC	Upper crack
WAC	Wavelet approximation coefficient
WDC	Wavelet details coefficients
WPT	Wavelet packet transform

Nomenclature

v_L	The longitudinal (compression) wave velocity in the material
v_S	The shear wave velocity in the material
$\zeta,\ \nu$	Lame constants
ϵ	Material density
γ	Ultrasonic beam half-angle of the probe
λ	Wavelength of sound in medium
ϕ	Probe crystal diameter
F	Cut-off factor at the beam edge
θ	Refraction angle with respect to the normal to the surface
D	Thickness of the test plate (material thickness)
d	Depth
C	Continuous Wavelet transform coefficients
ψ	Mother Wavelet
$f(t)$	Time signal
D_i	Details Wavelet coefficient
Θ	Threshold
S_{RMSF}	RMS value of the filtered signal
N_{RMSN}	RMS value of the noise-only part of the raw signal
i	Integer loop counter
j	Integer loop counter
$P(i,j)$	The grey-level co-occurrence matrix
$p(i,j)$	The normalised grey-level co-occurrence matrix
g	Number of discrete intensity levels of an image function
I	Two-dimensional image

$\theta(i)$	Number of points with intensity i in an image
$h(i)$	Two-dimensional image intensity histogram
$\delta(i)$	Delta-Dirac impulse function
μ_h	Mean of two-dimensional image histogram
σ_h^2	Variance of two-dimensional image histogram
n	The patterns' dimension
m	The number of patterns
c	The number of clusters
$X=\{x_i\}$	The given patterns
$Y_0=\{y_{i0}\}$	The initial c cluster centres
N	Maximum number of iteration allowed
ε	A given tolerance
β	A tuning parameter which controls the degree of fuzziness in the process
$Y=\{y_i\}$	The final cluster centers
(χ_{ij})	The final matrix of membership values
it	The number of iterations performed
d_x	Depth of the defect tip
X	Offset of the defect from the axis between the two probes
t	Transit time
s	Half the PCS (distance from one probe to the centre line of the weld)
d_{max}	The maximum depth (the deepest point of the ellipse)
d_{min}	The minimum depth
d_{error}	The error expressed as a percentage of the minimum depth
f	A fraction
D_f	Focus depth
bw	Backwall signal

lw	Lateral wave signal
DZ_{lw}	The dead zone due to the lateral wave
DZ_{bw}	The dead zone due to the backwall
t_{lw}	The times-of-flight of the lateral wave and the backwall signal
t_{bw}	The times-of-flight of the backwall signal
t_{pl}	The durations of the lateral wave acoustic pulse
t_{pb}	The durations of the backwall acoustic pulse
Δd_s	Error in depth resulting from error in probe centre separation
Δs	Error in the probe centre separation
t_r	Time referenced to the lateral wave time
E_s	The maximum timing error due to sampling
f_s	The sampling frequency
ρ	The resolution
Δd_x	Error in depth resulting from error in lateral position of the flaw
M	Maximal margin
$\|\mathbf{W}\|$	Hyperplane normal weight vector
L	Lagrangian
E_r	The risk
E_e	The empirical error
$V(F)$	The VC-dimension
$K(x_i, x_j)$	Kernel function
$\sigma_p^2(k)$	The energy of the decomposed image at node (p, k)
R_k	The k^{th} region in the blob
A_R	Area of all regions in the defect window after thresholding
Extent	Area of the region divided by the area of the smallest rectangle
A_{blob}	area (total number of pixels) of the blob outlining all islands

$A_{relative}$	Area of regions in defect window divided by area of that window
A_{rect}	Area of the smallest rectangle containing
CM_{ij}	Element of the confusion matrix (CM)
t_{tl}	The time of the longitudinal-diffracted echoes from the defect top tip
t_{bl}	The time of the longitudinal-diffracted echoes from the defect bottom tip
t_{ts}	The time of the shear-diffracted echoes from the defect top tip
t_{bs}	The time of the shear-diffracted echoes from the defect bottom tip
L	Length (height) of the defect

Chapter 1

Introduction

1.1 Non-destructive testing

Non-destructive testing (NDT) or non-destructive evaluation (NDE) of materials has been an area of continued growth for over seventy years. In simple terms, it is a group of methods and techniques to carry out tests on objects without destroying them or changing their physical characteristics. The objects can range from small devices to heavy equipment with different geometrical shapes and materials. The need and use for NDT has increased dramatically in recent years for various reasons such as product safety, in-line diagnostics, quality control, health monitoring, and security testing, etc. Besides the practical demands, the progress in NDT has a lot to do with its interdisciplinary nature. Industrial NDT of manufactured items is usually undertaken when a product is likely to be placed under extreme or long periods of stress or wear, or if any component failure is liable to result in a major incident. NDT methods and techniques involve both hardware and software components and modules. While the emphasis in NDT has long been on

the hardware technology, there has been an increased realisation of the potential benefits of applying advanced signal processing techniques to the signals resulting from an NDT examination.

NDT is widely used in industry to detect, size, classify and evaluate different types of defects in materials, and it plays an important role whenever the integrity and safe operation of engineered components and structures are critical. Efficient and reliable NDT techniques are essential to ensure the safe operation of complex parts and construction in an industrial environment for evaluating service life, acceptability, verification and validation and risk. Automating the evaluation and inspection process can potentially lead to a reduction or elimination of the impact of human error, thus making the inspection process more reliable, reproducible, and faster. The most widely used conventional NDT techniques are ultrasonics, radiography, infrared thermography and computed tomography (CT) techniques.

NDT is not a direct measurement method, thus the nature and size of defects must be obtained through analysis of the signals obtained from inspection. Signal processing has provided powerful techniques to elicit information on defect detection, sizing, positioning and characterisation. Inspection signals were in general 1-D, utilising the very basic signal processing techniques. In case of 2-D inspection signals (images), the main processing methods include operations like image restoration and enhancement, morphological operators, Wavelet transforms, image segmentation, as well as object and pattern recognition. These methods facilitate the extraction of special information from the original images, which would not, otherwise, be obtainable. Moreover, 3-D image processing can provide advance information if an image sequence is available. Currently, NDT techniques have developed greatly due to recent advances in microelectronic systems and signal

and image processing and analysis.

Advanced signal processing techniques allow extracting of information not easily available from the NDT measurements and thus essentially extend the resolution of the measurement beyond what is offered by the physical system. These techniques are expected to address the main problems in NDT when performing the inspection or examination. Mainly, these problems are: high levels of noise, high reflectivity of the material under test, defects orientation, high attenuations and/or low amplitudes of the received inspection signals, cladding thickness effect, grain structure of the material under test and the low accuracy of sizing, positioning and characterisation of flaws, among others.

There are various NDT techniques available for testing metal components and they are generally divided into two classes depending on crack location, i.e.

a) Surface-opening cracks NDT techniques:

- Magnetic particle
- Dye penetrant
- Magnetic techniques
- Ultrasonics

b) Internal cracks NDT techniques:

- Radiography
- Ultrasonics

No single NDT method works for all flaw detection or measurement applications. Each of these methods has its own advantages and disadvantages when compared to other methods [1].

Ultrasonic NDT techniques are useful and versatile because they are sensitive to both surface-opening and internal cracks and discontinuities, have superior depth of penetration and are highly accurate in sizing and positioning of flaws. The electronic equipment used for ultrasonic testing provides instantaneous results with detailed images, which is highly convenient for signal and image processing techniques.

1.2 Weld defects

Welding is a complex technology, and in any manual or mechanised welding process (Figure 1.1), the quality of the resultant weld is a function of a large number of uncontrolled variables. A welding defect is defined as any flaw that compromises the usefulness of the finished weldment. The difficulty in controlling the welding process means that most welds will contain some defects even if no errors are made in the welding procedure. A total absence of defects however, is very rarely required, and is also costly to achieve. Instead, any given weld is usually tested alongside a set of quality assurance (QA) standards which state the number and extent of allowable flaws in the welded joint [2, 3, 4, 5].

Welding defect causes are broken down into the following categories [6]:

a) Poor process conditions (about 41% of cases)

b) Operator error (about 32% of cases)

c) Wrong technique (about 12% of cases)

d) Incorrect consumables (about 10% of cases)

e) Bad weld grooves (about 5% of cases)

NDT is a must in order to detect and monitor defects in welds. Figure 1.2 shows specimens having different shapes and containing welds.

(a) Manual welding

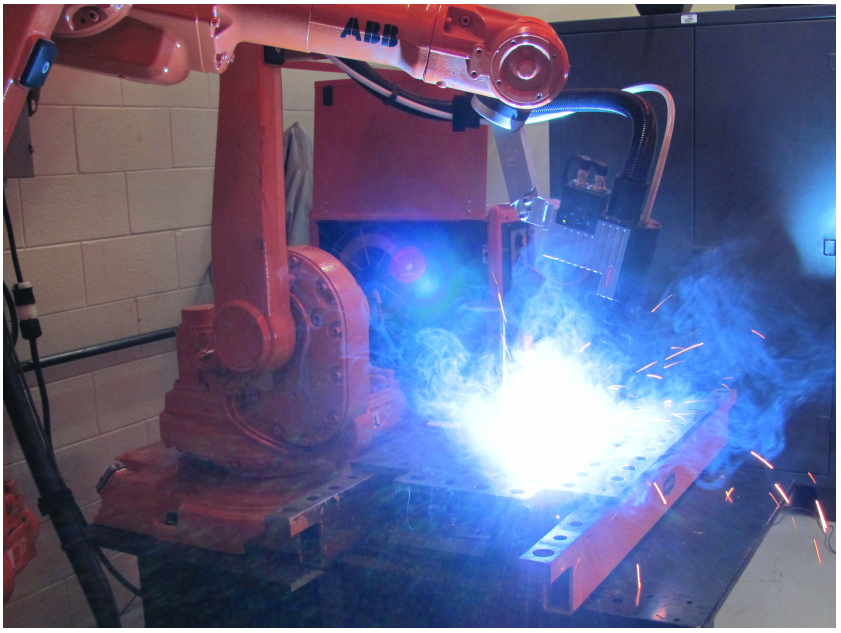

(b) Mechanised welding

FIGURE 1.1: Welding process

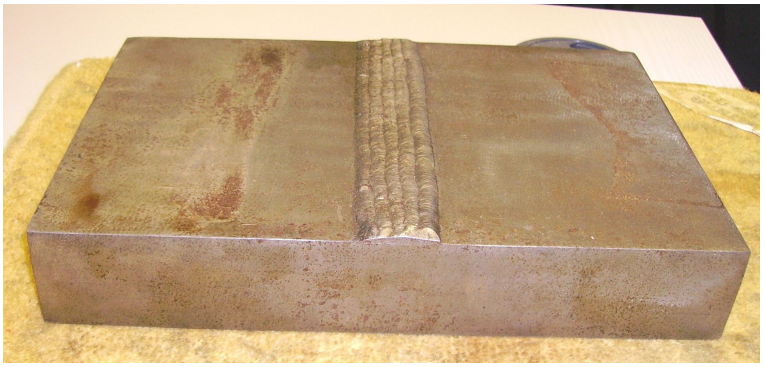

(a) An example of a specimen with a weld

(b) An example of a specimen with a weld

(c) An example of a specimen with a weld

FIGURE 1.2: Specimens with welds

1.3 Ultrasonic NDT methods and their strengths and weaknesses

Ultrasound is widely used in both medical and industrial inspections. In medical applications, the ultrasonic energy propagates in the tissues of the human body and the interactions of the sound with objects (like tumors for example) are recorded and displayed in the form of images for interpretation by a physician. In industrial NDT, ultrasonic waves are traveling in the components under test and the focus in this case is often on evaluating those components for flaws such as cracks.

Ultrasonic NDT methods are the most popular because of their capability in detecting and sizing cracks in a wide variety of locations and orientations in many materials used in engineering, and even for considerable thickness of material (e.g., greater than 300 mm in steel) [1, 5]. Other features of ultrasonic testing are flexibility, safety, and relative cost effectiveness. Moreover, ultrasonic testing can be quantitative and non-invasive or minimally invasive. The depth of penetration for flaw detection or measurement is superior compared to other NDT methods. It is highly accurate in determining flaw position and estimating size and shape, and can be used for other purposes such as thickness measurement. Minimal surface preparation is required in general.

Despite all the above good features of ultrasonic NDT, it suffers from some limitations. The surface of the component under test must be accessible to transmit ultrasonic energy. Ultrasonic NDT needs highly skilled operators and inspectors, hence extensive training is needed. Normally, it requires a coupling medium to endorse the transfer of ultrasonic energy into the component under test. Materials

that are rough in nature, small in size, irregular in shape, very thin or inhomogeneous are difficult to inspect. Cast iron, stainless steel and other coarse grained materials in general are very difficult to inspect due to low ultrasonic transmission and low SNR. With conventional ultrasonic NDT methods, linear defects that are oriented parallel to the ultrasonic beam may be overlooked. Reference standards and blocks are required for both equipment calibration and the characterisation of flaws.

Examples of ultrasonic NDT methods are pulse echo (PE), time-of-flight diffraction (TOFD) and phased-arrays (PA), among others. Time-of-flight diffraction is based on measuring the time-of-flight of ultrasonic waves diffracted from the tips of discontinuities originating from flaws. Echo strength in TOFD does not depend on the flaw orientation, allowing flaw sizes to be accurately determined (generally accurate to within ±2% of wall thickness, typically less than ±1 mm), with a high probability of detection of approximately 95% [2, 5].

1.4 Objectives and scope of work

The main objective of this research was to devise automatic interpretation algorithms and methods that work on TOFD data to detect, size and characterise defects in steel structures, with high accuracy and reliability, and minimum time to reduce one of the major bottlenecks found in practical inspections. The research took into consideration the problem of low quality of data and work on D-scan images only.

The following two points represent the main requirements of the project:

a) Developing automatic interpretation algorithms to size defects accurately in D-scan images only. Accordingly, the main target here is to assess the feasibility, limitations and any practical constrains of measuring the transverse position of a defect when performing D-scans by studying how the arcs of a defect indication vary with scan position, an information that would normally be obtained only from a B-scan image. This has not been addressed in literature before.

b) Utilising the information available in the mode-converted waves, which are usually overlooked and considered redundant. The anticipated utilisation will be in the areas of flaw detection, sizing and characterisation. Similarly, this has not been addressed in literature before.

1.5 Published work

A number of specialised publications have resulted as a direct outcome of the research presented in this thesis. These publications are as follows:

a) **Book publications:**

[1] A Al-Ataby and W Al-Nuaimy. Wavelet transform-multidisciplinary applications in NDT and Biometrics. In (Wavelet transforms and their recent applications in biology and geoscience). Dumitru Baleanu (editor). Publisher: InTech, ISBN: 979-953-307-538-8, 2012.

[2] A Al-Ataby and W Al-Nuaimy. Advanced signal processing techniques in NDT. In (Applied signal and image processing, multidisciplinary advancements). Rami Qahwaji (editor), Roger Green (editor) and Evor Hines (editor). Publisher: IGI Global, ISBN-10: 1609604776 EAN: 978-160-960-477-6, 2011.

b) **Journal publications:**

[1] A Al-Ataby and W Al-Nuaimy. Enhancing the accuracy of off-axis flaw sizing and positioning in TOFD D-scans using mode-converted waves, NDTMS RILEM Bookseriers, Vol 6, February 2012.

[2] A Al-Ataby, W Al-Nuaimy, C R Brett and O Zahran. Automatic detection and classification of weld flaws in TOFD data using wavelet transform and support vector machines, Insight - Non-Destructive Testing and Condition Monitoring (The Journal of the British Institute of Non-Destructive Testing), Vol 52, No 11, pp 597-602, November 2010.

[3] A Al-Ataby, W Al-Nuaimy and O Zahran. Towards automatic flaw sizing using ultrasonic time-of-flight diffraction, Insight - Non-Destructive Testing and Condition Monitoring (The Journal of the British Institute of Non-Destructive Testing), Vol 52, No 7, pp 336-371, July 2010.

c) **Conference publications:**

[1] A Al-Ataby A and W Al-Nuaimy. Mode-converted waves and D-scans for flaw sizing and characterisation in ultrasonic time-of-flight diffraction (TOFD), Proceedings of the 50^{th} Annual Conference of the British Institute for Non-Destructive Testing - NDT11, Telford, UK, 2011.

[2] A Al-Ataby and W Al-Nuaimy. Enhancing sizing accuracy of off-axis flaw TOFD D-scans using mode-converted waves, Proceeding of the 24^{th}

International Congress on Condition Monitoring and Diagnostic Engineering Management, Stavanger, Norway, 2011.

[3] A Al-Ataby and W Al-Nuaimy. Enhancing the accuracy of off-axis flaw sizing and positioning in TOFD D-scans using mode-converted waves, International Symposium on Nondestructive Testing of Materials and Structures-NDTMS11, Istanbul, Turkey, 2011.

[4] A Al-Ataby, W Al-Nuaimy and O Zahran. Towards automatic flaw sizing using ultrasonic time-of-flight diffraction, Proceeding of the Seventh International Conference on Condition Monitoring and Machinery Failure Prevention Technologies, Stratford-Upon-Avon, UK, 2010.

[5] A Al-Ataby, W Al-Nuaimy and C R Brett. Enhancing sizing resolution and off-axis flaw depth accuracy in D-scans using signal processing and mode-converted waves, Proceedings of the 49^{th} Annual Conference of the British Institute for Non-Destructive Testing - NDT10, Cardiff, UK, 2010.

[6] A Al-Ataby, W Al-Nuaimy, C R Brett and O Zahran. Wavelet transform and support vector machines (SVM) for automatic TOFD detection and classification of flaws, Proceedings of the 48^{th} Annual Conference of the British Institute for Non-Destructive Testing - NDT09, Blackpool, UK, 2009.

1.6 Thesis structure

This thesis is structured as follows:

Chapter 2 describes the ultrasonic TOFD basics with emphasis on its features, problems and applications. The chapter introduces also the concept of automatic TOFD interpretation system and its components.

Chapter 3 presents initial processing algorithms to enhance data quality. Pre-processing is an important step in order to prepare the collected TOFD data for subsequent processing. Its impact is very tangible when it comes to building a comprehensive automatic interpretation system using computer algorithms. The chapter also presents the techniques used to detect flaws automatically in TOFD images.

Chapter 4 presents automatic methods to size and locate flaws with high accuracy. Novel methods and algorithms will be used to obtain automatic flaw sizing and positioning information based on the compression waves region to help in obtaining accurate interpretation of data. Eventually, these algorithms help in reducing the overall interpretation time and minimising sizing and positioning error.

Chapter 5 presents a group of novel algorithms and techniques to build an automatic flaw characterisation stage using the support vector machines classifier. The input features to the classifier are Wavelet features along with other regional features. Flaw classification based on dimensionality will be discussed in this chapter as well.

Chapter 6 presents novel utilisations of the data available in the mode-converted returns for the purpose of accurate sizing and characterisation of weld flaws. The mode-converted shear waves utilisation is considered as an added value to obtain more useful and accurate results.

Chapter 7 illustrates the results after applying the proposed algorithms and methods on test samples. Also, it shows details regarding the built automatic interpretation tool and its features and capabilities.

Chapter 8 finalises the thesis by stating the conclusions, summarising the findings and proposing some future work and possible development areas.

Chapter 2

Ultrasonic Time-of-Flight Diffraction

2.1 Introduction

The high performance of the TOFD technique with regard to accurate sizing capabilities quickly led to industry acceptance of the technique. This chapter presents TOFD principles, latest work and data acquisition system and parameters, with overview of its features and limitations. The effects of these limitations on the performance of the technique are discussed. Furthermore, TOFD typical applications are presented. Finally, the concept and structure of an automatic TOFD interpretation system with its stages and the anticipated output are discussed.

2.2 Literature survey

Ultrasonic TOFD has received strong attention since the late 1970s as a technique to improve the sizing accuracy of flaws. Since then, lots of research work was carried out on fields like describing TOFD technique, discussing its reliability, TOFD systems development and hardware design and signal processing and analysis of TOFD data. However, work in the field of automatic TOFD interpretation is only recent, and a few number of research papers and articles can be found in literature. The discussion below shows a brief development life cycle of TOFD with some focus on automatic techniques.

The National NDT Centre at Hartwell (then part of the UK Atomic Energy Authority-UKAEA) asked Dr Maurice Silk to try developing an ultrasonic sizing technique that is more accurate than the conventional methods (PE at that time). In the early 1970s, Silk started the experimental work, with a focus on using the diffracted signals and the transit time delay to accurately measure the size and depth of the defects in steel structures. This work resulted in a new ultrasonic testing technique that was called TOFD. Then, Silk further developed the technique to improve sizing accuracy and the early results were very promising on artificial defects (the obtained accuracy was ± 0.2 mm) [7, 8]. Furthermore, Silk applied TOFD to inspect austenitic welds [9, 10, 11, 12] and the achieved sizing accuracy was ± 0.3 mm with defects deeper than 1.7 mm. Details of Silk's work can be found in a series of publications which focused on the potential improvement of defect sizing [12, 13, 14, 15, 16, 17, 18, 19]. The work described how TOFD can be used in accordance with the standard codes such as ASME XI code [20]. An important advancement was in 1990s when Silk proposed the use of advanced signal processing techniques and synthetic aperture focusing technique (SAFT) [21] to

improve the accuracy of data interpretation [22], followed by a major advancement when Silk concluded that the most accurate sizing technique can be achieved by the use of a parabolic shaped cursor to fit in turn to the wings of the flaw record and find the distance apart. Silk also investigated the probability of detection of flaws in noisy TOFD data and high probability was obtained at moderate levels noise [23].

After Silk, many researchers worked on studying TOFD principles and to expose its potential further like Trimborn [24], Mondal [25] and Brown [26]. Geus [27] gave an overview on the advances in transducers technology (the hardware side of TOFD) and also on the modelling and interpretation tools.

In the late of 1990s, some researchers demonstrated that TOFD can not be used as a stand-alone method to provide substantial precision in defect detection and sizing. Just [28], Erhard [29, 30] and Hecht [31] demonstrated that TOFD can be used as an additional inspection method for verification of PE or radiography techniques. Kreier *et al.* [32] confirmed this also by performing many tests on artificial and natural defects and reached to a conclusion that TOFD is not an alternative to PE but can be an addition to it in order to be able to detect and size a wide range of defects including the surface ones.

The researcher who had faith in TOFD at that time tried to prove otherwise. Geus [27] and Brown [26, 33, 34] demonstrated that TOFD can be used as a stand-alone inspection method and went even further to say that it can replace conventional techniques such as PE and radiography. Betti [35, 36] also demonstrated this by experimental comparison. Trimborn [37] measured the performance of TOFD and concluded that TOFD is an efficient technique for defect detection and sizing. Webber [38] and Krutzen [39] also demonstrated this by examples and

comparisons with other ultrasonic sizing techniques to prove that TOFD is an accurate sizing technique and that it can be used for detection and characterisation of flaws with high accuracy as well.

Baby *et al.* [40, 41, 42] was another researcher who highly contributed in the development of TOFD's sizing capabilities by investigating the sizing of cracks embedded in sub-cladding in B-scan images and obtained an accuracy of ± 0.2 mm with crack heights ranging from 1.68 mm to 19.04 mm in steel structures surfaces.

Some automatic attempts then started to emerge. Lawson [43, 44, 45, 46, 47] used image processing and multi-layer perceptron artificial neural network (ANN) to automate detection of weld defects. His focus was to perform the detection at elevated temperatures of up to 250° C. For that purpose, very high temperature probes are developed to give much better results in these high temperatures as the SNR was found to be decreased sharply [48, 49, 50].

Voon *et al.* [51] then developed a genetic-based inverse voting Hough transform method for automatic detection of parabolas in B-scan images to be able to perform automatic sizing. Maalmi *et al.* [52] had similar work in this area. Baskaran *et al.* [53, 54, 55] and Swamy *et al.* [56] proposed an automatic sizing method for vertical and inclined defects in thin plates ($6 - 10$ mm) in B-scan images by developing a TOFD system that was integrated with a developed embedded signal identification technique (ESIT) and point source correlation technique (PSCT). The achieved results were quite good compared to manual inspection and the performance in accuracy was 93% compared to 84% for manual inspection.

Moura *et al.* [57, 58] worked on automatic defect classification by using hierarchical and non-hierarchical linear classifiers to be able to classify different defect

categories in welds like lack of penetration, lack of fusion and porosity.

Zahran [2, 59] developed and implemented what can be considered as a first attempt towards a comprehensive automatic interpretation aid for TOFD D-scan data, with emphasis on accuracy, reliability, efficiency, minimum user interaction and simple output presentation in order to be suitable for in-site interpretation, thereby shifting part of the interpretation burden from a trained human operator to a machine.

Automatic TOFD data interpretation methods are of significance and interest to many researchers because of their benefits in terms of reducing the burden on human operators and, hence, reducing measurement errors, and ultimately, saving time and cost. The main interest in this area is to develop reliable and robust algorithms that are capable of producing results from data collected in different operating conditions and components that are characterised by having different shapes and sizes.

2.3 Ultrasonic waves in homogeneous and isotropic media

The term ultrasound is used to describe sound waves with frequencies that are above the audible range. While sound is a wave motion in gases such as air, the term is also used for elastic waves in solids. In general, wave motions in solids are more complex than those arising in gases. A gas can not support shear stress and so the particle displacement is always parallel to the direction of propagation of the waves. These waves consist of alternate regions of compression and rarefaction in a

periodic pattern. A solid body can support shear stress, so the displacement needs not be parallel to the direction of wave propagation. Accordingly, two distinct cases emerge: first the displacement is parallel to the direction of propagation and the wave is called a compression wave; second, the displacement is perpendicular to the direction of propagation and the wave is called a shear wave. In a shear wave, the displacement can be in any direction perpendicular to the direction of propagation. In an isotropic medium, remote from boundaries, all shear wave polarisations are equivalent but, at boundaries between media, the behaviour of the wave depends on the direction of polarisation. It is usual, therefore, to resolve a shear wave of arbitrary polarisation into components with mutually perpendicular polarisation directions defined with respect to the plane of the boundary [4, 5].

The compression wave is actually the primary wave, as it is the first signal to arrive at the receiver. Most TOFD studies carried out to date have used compression waves rather than shear waves for this very reason.

The symbols v_L and v_S will be used to denote the speeds of compression waves and of shear waves respectively. In an isotropic material, there can be only two distinct elastic constants and they are called Lamé constants. The compression and shear wavespeeds are related to these elastic constants of anisotropic material through the relations [5]:

$$v_L = \sqrt{\frac{\zeta + 2\nu}{\epsilon}} \tag{2.1}$$

$$v_S = \sqrt{\frac{\nu}{\epsilon}} \tag{2.2}$$

where ζ and ν are the Lamé constants and ϵ is the density. Shear waves travel at about half the speed of compressional waves (e.g. in Aluminium, 3.04 mm/μs compared to 6.42 mm/μs).

It is worth mentioning that in NDT applications, the amplitude of the waves is very small and so the materials behave in a linear elastic way. In other applications, where amplitudes may be large enough for non-linear behaviour to occur, wave propagation can be more complicated.

2.4 Ultrasonic TOFD overview

For a number of years, PE method was the most ultrasonic NDT method of choice. The PE method relies on the echo amplitude to size the flaw and the pulse travel time to locate the defect position and orientation [5]. It is based on the assumption that echoes from the planar features suitably angled travel back to the transducer. Though simple and inexpensive, it suffers from poor resolution for crack sizing when the echo is severely attenuated. Furthermore, the amplitude of the reflected echo may be influenced by many factors such as surface roughness, particles in the component under test, transparency and orientation of the flaw [5]. To overcome the limitations of the PE method, the ultrasonic TOFD was developed. It has higher accuracy in measuring the through-wall size of crack-like defects, and can be used in a wide range of material thickness. It has gained popularity because of its high probability of detection (POD), low false call rate (FCR), portability and most importantly, its intrinsic accuracy in flaw sizing and positioning, especially in depth [5, 60].

2.4.1 Diffraction process

TOFD is based on measuring the time-of-flight of ultrasonic waves diffracted from the tips of discontinuities originating from flaws. When an ultrasonic wave interacts with a crack, it results in the production of diffracted waves from the crack tips, in addition to any ultrasonic waves reflected from the surface of the crack. The diffracted waves are much weaker than the specularly reflected waves used in conventional ultrasonic inspection, but they radiate in all directions along the same plane as the incident ultrasonic waves as indicated in Figure 2.1.

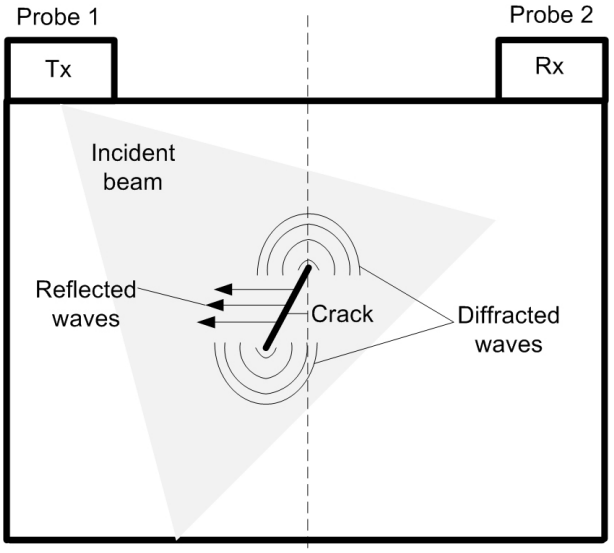

FIGURE 2.1: Representation of the diffraction process from crack tips

The phenomena of diffraction is nothing new and occurs with all types of waves, e.g. light and water waves. It is very well-known in light especially when it is passed through a slit or past an edge and contributes to the resolving power of telescopes and other optical instruments [4, 5].

2.4.2 TOFD arrangement

TOFD is mainly a flaw sizing technique that is based on locating the crack tips from the ultrasonic energy re-emitted by diffraction. The basic arrangement of TOFD consists of two probes in a pitch-and-catch configuration, with one probe acting as a transmitter and the second probe as a receiver (Figure 2.2). Such an arrangement provides a large volume for inspection and unambiguous measurement capabilities of the position and depth of the flaws. A single probe could be used but it is not recommended since it reduces the accuracy of locating the flaw tips. Figure 2.3 shows a equipment of TOFD.

Accordingly, two longitudinal broad beam probes are used in the transmitter-receiver arrangement, so that the entire flaw volume is flooded with ultrasound and, consequently, it can be inspected using a single scan pass along the inspection line (D-scan in this case), as shown in Figure 2.2 (a). When longitudinal waves are reflected or refracted it can be partially converted into shear waves (mode-converted echoes) with a lower speed (half roughly) than the longitudinal waves.

2.4.3 Scan types

TOFD equipment can be set up and used to produce two types of scans. The initial scan generally used for flaw detection and is called the non-parallel or longitudinal scan because the direction of scan is at right angles to the direction of the ultrasonic beam as illustrated in Figure 2.2 (b). The resultant scan is known as a D-scan since it produces a cross section along the weld. This type of scan is usually set up with as wide a beam spread as possible to inspect a larger volume with one scan. Since the probes straddle the weld, the weld cap does not interfere with the

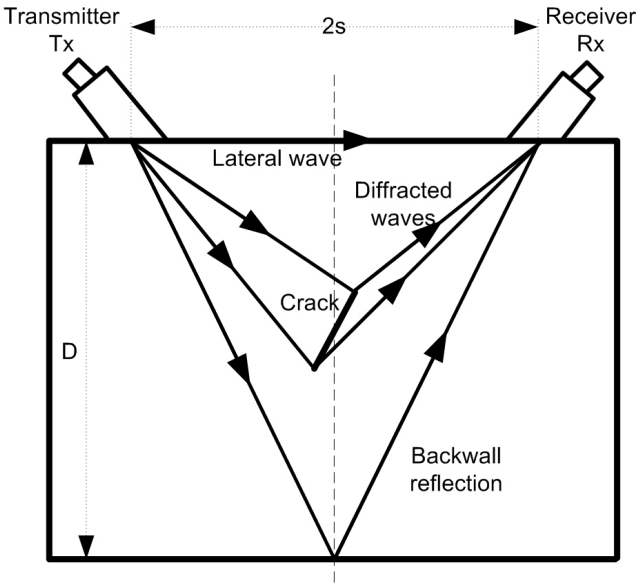

(a) General principle (D: thickness, 2s: probe separation)

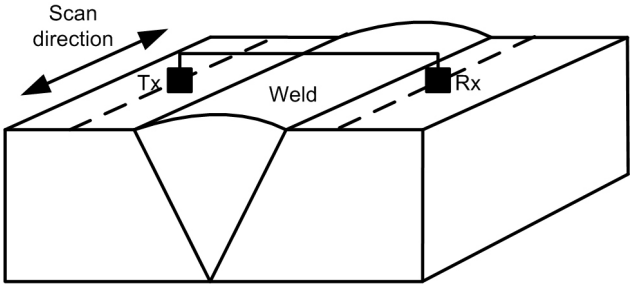

(b) D-scan

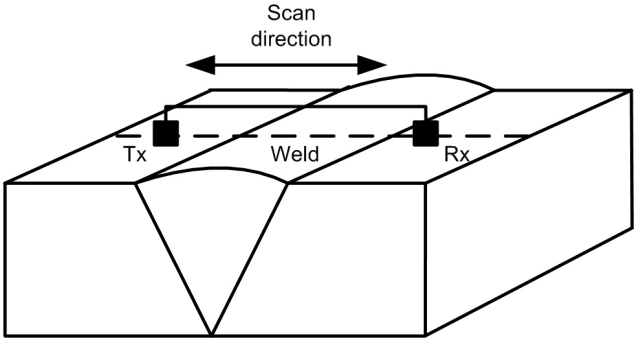

(c) B-scan

FIGURE 2.2: TOFD arrangement

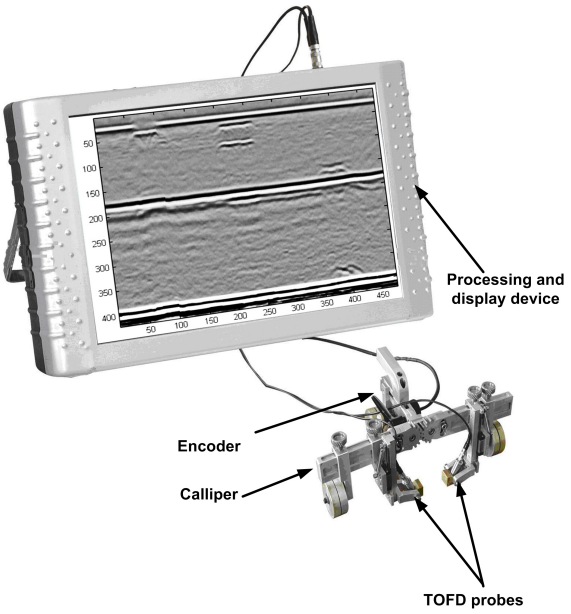

FIGURE 2.3: A typical TOFD equipment

scan. It is a very economical and fast inspection and is the most frequently carried out scan. Despite of all its good features, sizing and positioning of defects using D-scan are not accurate due to a combination of errors and limitations (will be explained later in Section 4.4).

The second type of scan is shown in Figure 2.2 (c) and is called the transverse or parallel scan. In this case, the direction of scan is parallel to the ultrasonic beam direction. The produced scan is called a B-scan since it produces a cross section across the weld. If there is a wide weld cap, it is difficult to carry out the scan and only a limited movement may be possible [2, 5]. This type of scan gives the most accurate measurement of depth because at some point within the scan the defect will lie equidistant between the two probes, a situation that leads to a minimum time-of-flight, and hence higher accuracy.

In practice, in order to make a reasonable guess as to the type of defect and to get the best sizing accuracy, a D-scan is normally followed by one or more B-scans at the estimated position of the flaw. While B-scans can potentially reduce the

depth and position uncertainty associated with D-scans, they are not carried out routinely as part of a weld inspection unless D-scans reveal flaw signatures, in which case they are implemented where needed. They are therefore incompatible with automated inspection regimes, and are both cumbersome and costly to deploy [5, 61, 62].

2.4.4 The collected data

The receiving probe collects the ultrasonic returns and converts them into voltages. These voltages represent the collected data that are digitised and stored on a portable computer or a device attached to the data acquisition platform. The data is collected at each point along the scanning line and forms signals which are called the A-scans. Figure 2.4 shows an A-scan with indications for a crack (indications 2 and 3).

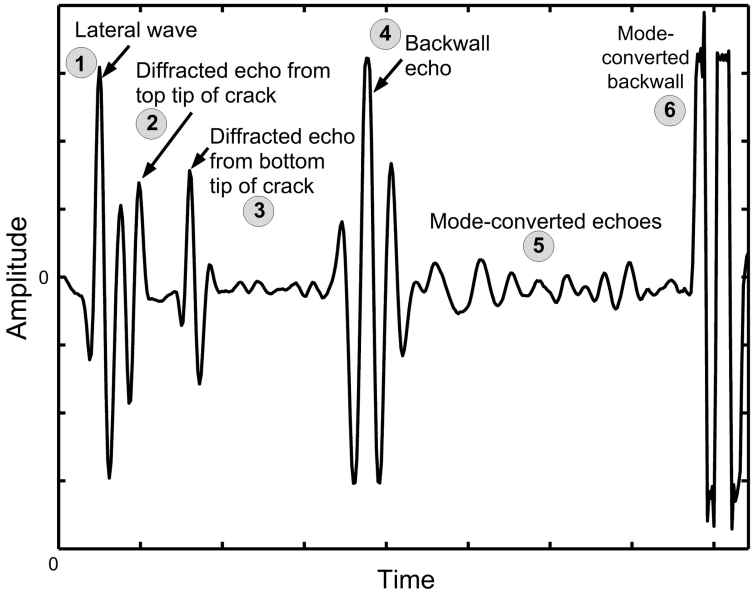

FIGURE 2.4: A typical A-scan representation

The A-scans can be stacked together side-by-side to form a two-dimensional D-scan or B-scan image depending on the relative scanning direction. If the A-scans are generated from the scanning along the length of the weld, then the resultant is a D-scan image as shown in Figure 2.5 (a), or if generated from parallel scanning across the weld, then the resultant is a B-scan image as shown in Figure 2.5 (b).

2.4.5 The observed signals

The probes that are used in TOFD equipment are compression wave probes. The transmitter probe transmits compression or longitudinal wave into the material during which it splits up into the desired compression wave at the required angle and into a shear wave at approximately half the angle of the compression wave. Thus, shear waves are present in the material but the resultant signals generally occur after the compression ones. Accordingly, the resultant TOFD inspection data can contain three different waves: waves that have travelled all the way as compression, waves that have travelled all the way as shear and finally, waves that have travelled part of the path as compression and part as shear.

When an ultrasonic wave encounters a flaw, it undergoes reflection and diffraction. Each flaw tip acts as a point source of diffracted energy over wider angles that is well suited for flaw detection and sizing as it is directly related to the true position and size of the flaw. The diffracted signals are often of lower amplitude than the reflected signals, depending on several factors like the nature of the crack tip, the crack orientation with respect to the probes, the compressive forces on the crack face and the material noisiness [3].

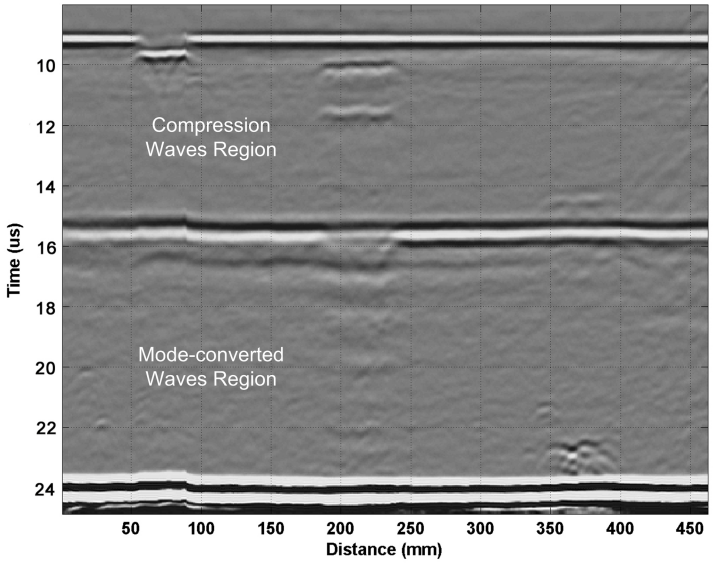

(a) A typical D-scan

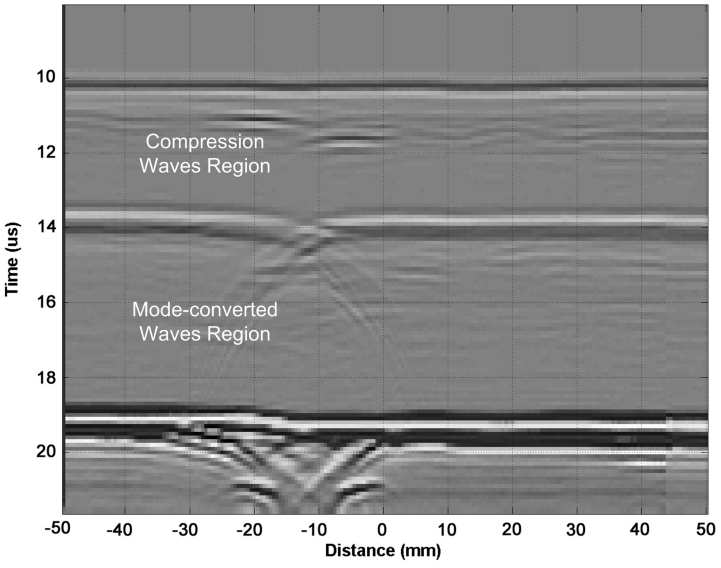

(b) A typical B-scan

FIGURE 2.5: Examples of TOFD D- and B-scan images

With reference to the A-scan signal (Figure 2.4), there are generally four signals that need to be observed during interpretation:

a) Lateral wave

In general, a weak lateral wave running between the two probes directly with compression velocity just below the surface of the metal is observed first. Since it travels in a straight line between the two probes then it takes a minimum time, and for a curved surface it travels straight across the material between the two probes as well. The lateral wave can be very week for large probe separation and may not even be recognisable. Because of the basic pitch-catch probe arrangement, the signals from the near surface region are very compressed in time and these signals may be hidden beneath the lateral wave. In the A-scan of Figure 2.4, the lateral wave is shown by indication 1.

b) Backwall signal

A much larger signal reflected from the backwall of the material and it comes after the lateral wave because of the distance travelled. It arises from both the longitudinal and the mode-converted waves reflected from the bottom surface. However, if the probe beams are directed at the upper part of the material or there is no suitable backwall then there may be no backwall signal. In the A-scan of Figure 2.4, the lateral wave is shown by indication 4.

c) Defect signals

If a crack is present in the material in the overlapping beam of the two probes then diffraction signals from the top and bottom tips are seen between the lateral wave and the backwall (indication 2 and 3 in Figure 2.4). These signals are generally much weaker than the backwall signal but stronger

than the lateral wave. If the defect has little height, then the signals from the top and the bottom may be overlapped. Thus, improving the resolution comes as an important requirement in such cases. Because the diffraction signals are so weak, they can not always be easily seen on a single A-scan, and it is only by successive scans in B- or D-scans because the pattern of the diffraction signals becomes clear.

d) Shear or mode-converted shear waves

After the compression backwall signal, a much larger signal generally appears and is a backwall shear reflected signal (indication 6 in Figure 2.4) that is often mistaken for the compression backwall signal. Between these signals, other signals are generally observed due to mode-conversion at a defect into shear waves (indication 5 in Figure 2.4), which then takes a longer time to arrive at the receiver. It is often very useful to collect signals in this region since genuine defect signals are repeated at longer times, and near surface defect signals may be clearer because they are spread out in time more for the shear waves. In practical scenarios, mode-converted waves are often overlooked and considered redundant when performing manual interpretation.

Mode-converted shear waves appear in the portion of the TOFD image immediately after the backwall echo (see Figure 2.5), and may provide an exceptional resolution of shallow flaws especially when the flaw is located closer (laterally) to one of the probes. In all cases, due to the lower speed of these echoes, they may provide better resolution of the flaws than in the compressional wave. Although this mode-converted data is often discarded because the diffraction signal is stronger for longitudinal waves than for shear waves and to gain benefits in

processing time, there are instances where examining the patterns in this portion can lead to meaningful insight into the geometry and nature of the flaws. Further details on the utilisation of the mode-converted waves will be presented in Chapter 6.

2.4.6 Phase relationship

When a wave in a medium with a higher acoustic impedance (or sound impedance, which indicates how much sound pressure is generated by the vibration of particles of a medium at a given frequency) is reflected at the interface with another medium which has a lower acoustic impedance (e.g. steel to water or steel to air), then it undergoes a phase change of 180°. This means that if a wave starts with a positive cycle before hitting a wall, then it will start with a negative cycle after the reflection from the wall. When a defect is present in a material, then the signal from the top tip acts as if it has undergone a reflection from a backwall, and a phase change of 180° occurs, i.e. the phase of the top tip is following that of backwall signal and starts with a negative cycle. The bottom of a defect, on the other hand, acts as if the wave runs without a major phase change and it follows the phase of the lateral wave, i.e. it starts with a positive cycle. An illustration of this concept is shown in Figure 2.6, with an A-scan having no defect in one case and a defect in the other. Theory shows that if two diffracted signals have opposite phase, then there is a high probability that there is a continuous crack between them. It is because the phase information that it is necessary to collect the TOFD unrectified signals digitally. It was found that signals diffracted from the flaw bottom are approximately 45° out of phase with the lateral wave, whereas

those diffracted or reflected from the flaw top are approximately 45° out of phase with the backwall echo [3, 4].

Thus, correct exploitation of phase information is important for characterising signals and in accurate sizing and positioning, and in many cases, these phase differences are not immediately apparent to a trained eye. This further emphasises on the need for automation. More details will be shown later in Sections 4.4.6 and 5.4 in this regard.

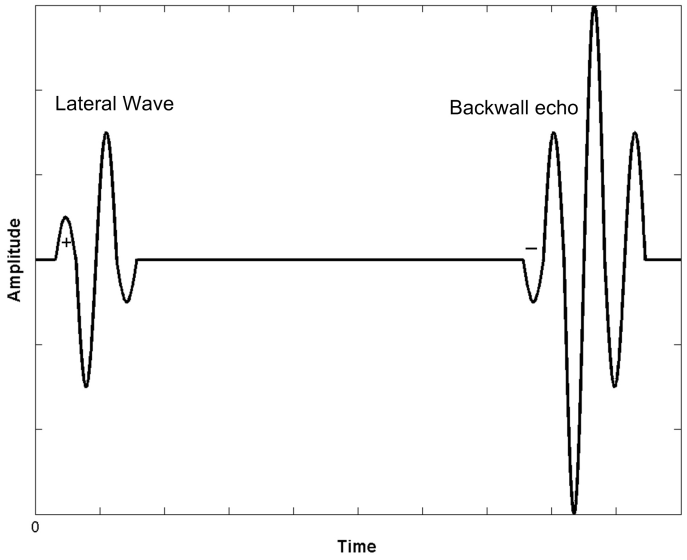

(a) A-scan without a defect

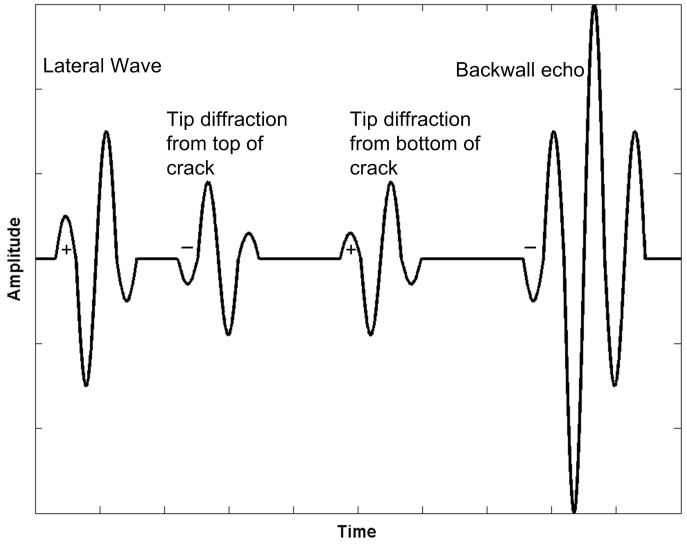

(b) A-scan with a defect

FIGURE 2.6: Phase relationship in an A-scan

2.5 TOFD system and data acquisition parameters

2.5.1 TOFD system

Legacy ultrasonic NDT inspections are carried out manually with angled shear wave or compression probes using an analogue flaw detector that facilitates one probe to be used at a time with no kept records of the observed ultrasonic signals. Since 1990, the TOFD analogue systems have tended to become computer-controlled with facilities like storage of data and set-up parameters, which makes the system easier to use. However, a small percentage of inspections have had to be mechanised and handle arrays of probes for reasons of speed (e.g. steel mill), safety (e.g. nuclear plant) or environment (e.g. under the sea). For these inspections, very sophisticated digital systems have been developed for handling arrays of probes, controlling mechanised scanners and recording the inspection data.

For TOFD inspection, the system needs to record the full unrectified A-scan at each inspection position or at least sufficient information to reconstruct it. A typical system block diagram for collecting TOFD data is shown in Figure 2.7. The system contains transmitter/receiver channels which are selected under processing unit (or computer) control in sequence by the multiplexer. The processing unit normally multiplexes at each inspection point around those channels which have been defined in the inspection set-up. In TOFD configuration, separate transmitter and receiver channels are defined for each pair of TOFD probes used in the inspection.

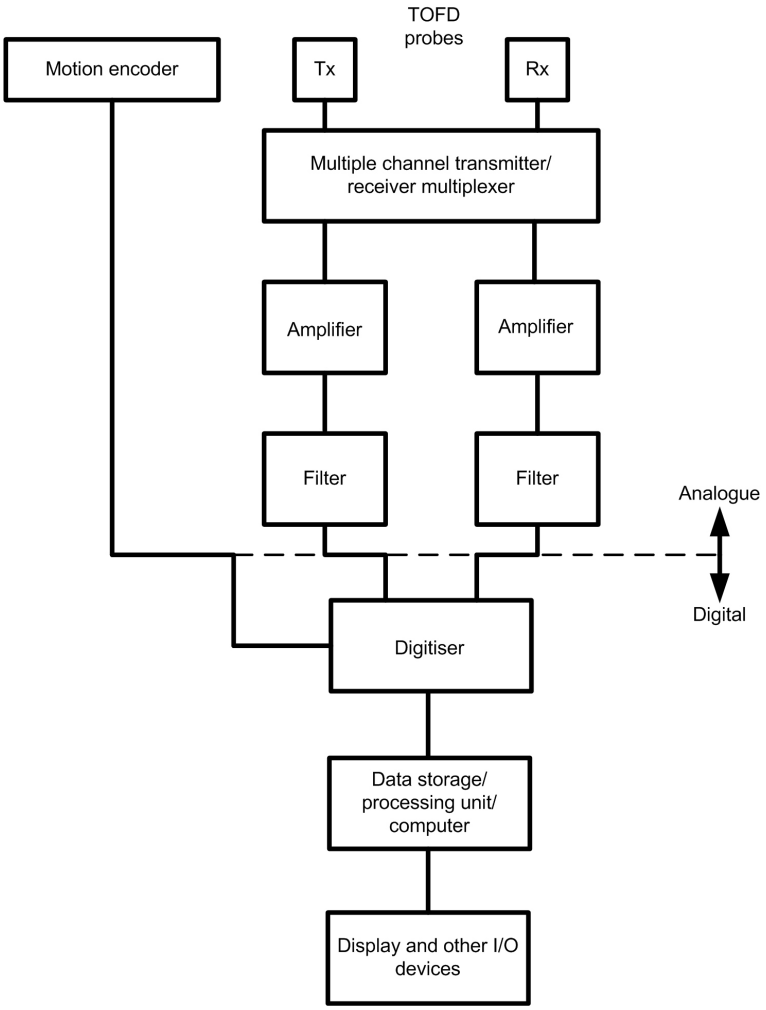

FIGURE 2.7: A typical block diagram of a system for collecting TOFD data

TOFD signals are weak in general and become even weaker if the probes are situated on some distance from the recording system. In this case, an amplification block is needed in the system. All TOFD systems feature an amplifier with a typical gain of about 70 dB, and in some cases, more amplification may be needed, thus battery operated amplifiers are used with gains of the order of 30 or 40 dB. These additional amplifiers have the advantage of having low electrical noise levels because they are not using the same main supply of the collection system.

Such systems are often electrically noisy, and there may be external electrical noise as well. Hence, it is usual to restrict the frequency bandpass of the amplifier

by means of filters to the spectrum of frequencies appropriate to the ultrasonic probes being used. While this may reduce the overall amplitude, it should improve the SNR of the amplified signals.

The resultant amplified and filtered analogue signals are then converted into a string of digital numbers by means of a digitiser (an analogue-to-digital converter, ADC) and stored for further processing by the processing unit. Additional components such as a display and other input/output devices are used to provide visual means to check the collected data and provide the ability to interact with the acquisition system. The system generally has provision for measuring probe position by means of the encoder input facility to calibrate the scanned distance.

The ultrasonic energy should penetrate the material under test with a specific angle, therefore, the probes are mounted on wedges of perspex or similar material with angles. A coupling material (couplant) must be presented between the wedges and the surface of the tested material in order for ultrasound to be transmitted with no losses in any air gap found between the surfaces. The distance between the two probes is called probe centre separation (PCS) and it should be fixed. Therefore, a calliper (see Figure 2.3) is used to joint the two probes with the required separation. A scan software is needed on the processing unit in order to store and process the collected signals.

2.5.2 TOFD probes

The transmitter and receiver probes are compression transducers which allows the conversion of electrical energy into ultrasonic energy and vice versa. The ultrasonic probe has two important characteristics, the centre frequency and crystal diameter,

and both probes should have the same centre frequency. The choice of probe is highly dependent on the application area, the objectives of the inspection and material characteristics. For most inspection applications, probes with centre frequencies between 2 MHz and 10 MHz and diameters of 3 to 20 mm crystal are suitable [4, 5].

Increasing the centre frequency of the probe has the following effects [2]:

- Shortens the wavelength,
- Improves flaw resolution,
- Shortens time duration of lateral wave,
- Decreases beam divergence,
- Increases near field length,
- Decreases penetration (higher attenuation), and
- Increases acoustic grain scatter.

Similarly, increasing the probe crystal diameter has the following effects:

- Increases output,
- Decreases beam divergence,
- Increases near field length, and
- Increases contact area, emission point closer to front of wedge.

The opposite can be said when decreasing the centre frequency and the probe crystal diameter of the probe.

To select appropriate probes centre frequency and crystal diameter, some compromise is necessary. However, for a general use, a 5 MHz broadband probe with a 6 mm diameter is recommended. Both the transmitter and receiver probes should have the same frequency within a tolerance of 20% [4].

2.5.3 The probe angle

The main factor affecting the choice of the probe angle (θ) is the required focus depth inside the material under test. This should be chosen in conjunction with a suitable PCS. In many applications, typical angles of 45°, 60° or 70° are appropriate.

The probe angle 45° provides higher resolution on the expense of lower volume of inspection coverage. Probe angle 70° provides higher volume of inspection coverage but with lower resolution. Considering that, the optimum angle for diffraction is between 60° and 70° [2, 4, 5]. Figure 2.8 shows the effect of changing probe angle on the inspection coverage and the resolution. A compromise is also necessary when choosing a suitable probe angle.

Probes of 60° are more suited to heavy wall materials where the (weaker) upper edge of a 45° beam may be attenuated by the long transit paths involved. Thinner wall materials may necessitate a wider probe separation than the optimum. In this case, the probe angle is increased to compensate for the increased PCS. Angles higher than 60° are rarely necessary on thin wall materials as the intensity of the

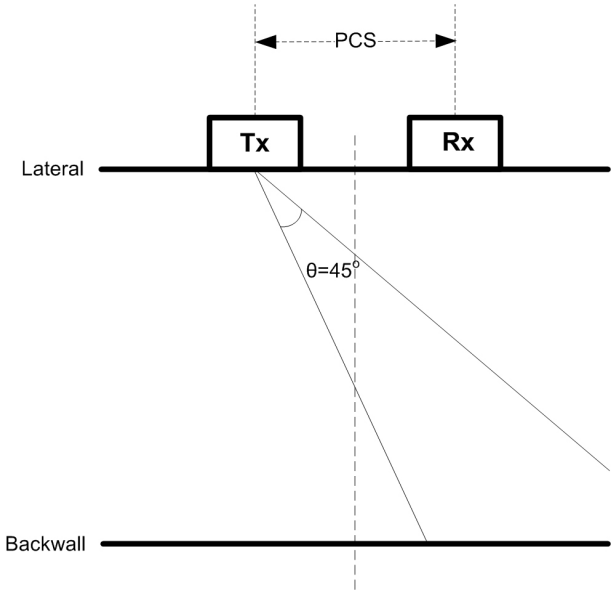

(a) 45°, narrow beam, lower inspection coverage, high resolution, narrow PCS and weak lateral wave

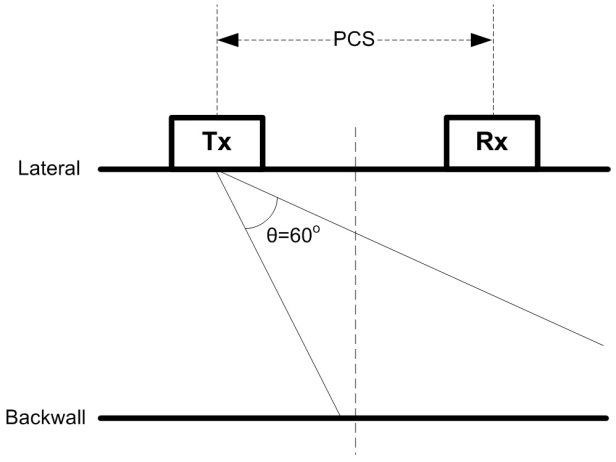

(b) 60°, wider beam, higher inspection coverage, medium resolution, wider PCS and good lateral wave

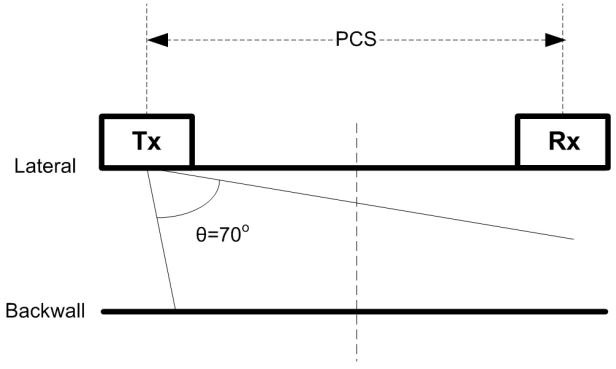

(c) 70°, widest beam, highest inspection coverage, low resolution, widest PCS and strong lateral wave

FIGURE 2.8: Effects of probe angle (θ) choice

lateral wave increases to unacceptably high values, making it more difficult to recognise near surface flaws. Knowledge of the precise beam angle is not necessary for TOFD inspection. Variation of $\pm 5^{\circ}$ from nominal does not affect the quality of inspection by any appreciable amount.

2.5.4 Beam spread considerations

One of the most important consideration in TOFD inspection is probe beam spread since generally the aim is to inspect a large volume of the component under test with as minimum number of scans as possible so that all flaws show up. In general, this is not usually difficult to achieve because of the refraction of the beam at the material surface and the common use of high beam. Hence, it is important to calculate the volume of coverage. With reference to Figure 2.9, the ultrasonic beam half-angle (γ) from a disc crystal oscillator is defined as [5]:

$$\sin \gamma = \frac{F\lambda}{\phi} \tag{2.3}$$

where λ is the wavelength of sound in medium, ϕ is the probe crystal diameter and F is a factor depending on the choice of cut-off factor at the beam edge, e.g. for 6 dB, $F = 0.51$ and for 20 dB, $F = 1.08$. Equation (2.3) confirms a well-known fact in ultrasonics that the widest beam spread can be obtained using the lowest probe centre frequency and the smallest crystal diameter. It is worth mentioning that the above equation is adequate for calculating the beam spread in beyond the near field [4].

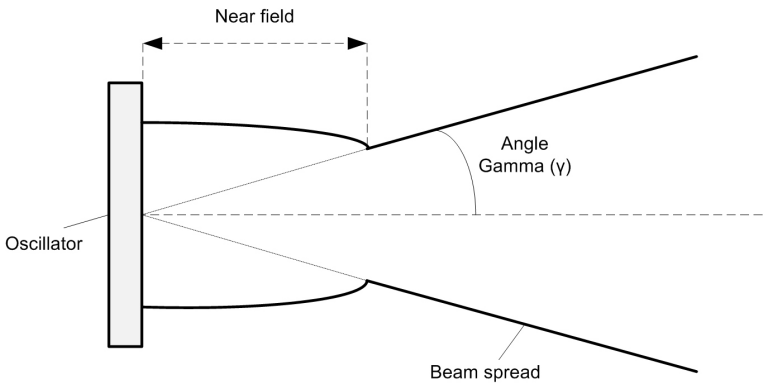

FIGURE 2.9: Definition of beam spread

In order to obtain longitudinal or compression waves into the metal at angles of typically 45°, 60° and 70°, a perspex wedge is attached to the transducer face and cut at an appropriate angle that can be calculated using Snell's law:

$$\frac{c_1}{c_2} = \frac{\sin\theta_1}{\sin\theta_2} \tag{2.4}$$

where c_1 is the velocity in the medium 1 (wedge), c_2 is the velocity in the medium 2 (steel), θ_1 is the refraction angle with respect to the normal to the surface in in the medium 1 and θ_2 is the refraction angle with respect to normal to surface in the medium 2.

The beam spread in the metal can be found using the beam spread in the wedge and then calculating the corresponding beam edge angles in the metal. Table 2.1 below summarises the beam spreads for a beam centre angle of 60° in steel. The beam spreads for various beam angles in steel are listed in the Table 2.2 for 5 MHz probes. As indicated in this table, the beam spread is not symmetrical about the beam centre because of Snell's law and any increase in frequency or crystal diameter rapidly reduces the beam spread.

TABLE 2.1: Beam spread for various probes for a beam centre angle 60^o [4]

Probe centre frequency (MHz)	Beam spread for centre angle 60 ° in steel		
	$\phi = 6$ mm	$\phi = 10$ mm	$\phi = 15$ mm
3	40.2 ° - 90 °	47.3 ° - 84 °	51.1 ° - 72.2 °
5	47.3 ° - 84 °	51.9 ° - 70.6 °	54.5 ° - 66.5 °
10	3.2 ° - 68.5 °	55.8 ° - 64.8 °	571 ° - 63.1 °

TABLE 2.2: Beam spreads for 5 MHz probes in steal [4]

Probe angle	Beam spread in steel		
	$\phi = 6$ mm	$\phi = 10$ mm	$\phi = 15$ mm
45 °	34.0 ° - 57 °	38.8 ° - 51.8 °	40.8 ° - 49.9 °
60 °	47.3 ° - 84 °	51.9 ° - 70.6 °	54.5 ° - 66.5 °
70 °	54 ° - 90 °	59.6 ° - 90 °	62.6 ° - 82.1 °

2.5.5 The PCS and focus depth

Probe centre separation distance is an important factor in identifying the area of interest inside the material under test. It should be selected so that to ensure adequate diffracted energy from flaw tips is obtained with acceptable resolution. It is generally recommended that the PCS is selected so that the focal point depth (D_f) to be at two-thirds of the material thickness [3, 4]:

$$D_f = \frac{2}{3}D \tag{2.5}$$

where D is the material thickness. This choice provides coverage of the majority of the weld unless a specific area of the weld is required to be inspected.

If the resultant coverage is not adequate with a single scan, then it is advisable to have more than one PCS values to fulfil all inspection requirements. If the focus depth is d mm, then the PCS for a probe angle θ is given by (see Figure 2.8):

$$PCS = 2D_f \tan\theta \tag{2.6}$$

When focusing at two-thirds of the material thickness, the PCS is given by:

$$PCS = \frac{4D}{3} \tan\theta \tag{2.7}$$

and when focusing at the backwall, the PCS is given by:

$$PCS = 2D \tan\theta \tag{2.8}$$

The PCS is so critical in flaw detectability and resolution. Needless to say that flaw sizing ability will be affected by the choice of the PCS as well. More details will be shown later in Section 4.5 in this regard.

2.5.6 Resolution and precision

Resolution defines the ability to separate two signals before they can correctly be identified. In TOFD, resolution will be the ability to distinguish between the top and bottom tip diffraction signals from one small crack. Resolution therefore sets a lower limit to the size of flaws for which top and bottom diffraction signals can be detected. It can be improved by:

- Using probes that produce short pulses (Section 2.5.8),
- Using probes with higher frequency (Section 2.5.2),
- Using probes with high damping,
- Reducing the PCS (Section 2.5.5), or

- Increasing the sampling frequency (Section 2.5.7).

The first three points are all dependent on probe specifications. The use of probes that produce short pulses are likely to be less affected by material attenuation, but the choice of high frequency probes depends on the thickness of metal and resultant attenuation. As mentioned previously, the trend is to choose lower frequency because of the beam spread considerations.

Generally speaking, it is more practical and realistic to tune both the PCS and the sampling frequency to enhance the resolution. The resolution of near surface flaws can be improved if the probes are brought closer together. Alternatively the resolution of flaws near the backwall can be improved if the flaws are close to the probe centre line. For other flaws, resolution may be aided by tuning the PCS in certain ways. Obviously, some compromise is necessary.

A mathematical formula is derived to assess the impact of tuning the PCS and the sampling frequency on the resolution. The derivation of this formula will be shown later in details in Section 4.5.

Precision is the accuracy with which the time of the arrival of the signal (peak or crossover point) can be made. The best that can be obtained is about one-tenth of the wavelength. For example, for a 5 MHz probe and ultrasound velocity in steel of 5960 m/s, the precision is about 0.1 mm [3]. This is the best that TOFD could achieve for accurate sizing. In practice, this can not be achieved with manual interpretation of D-scans because of various incorporated errors.

2.5.7 The sampling frequency

The obtained unrectified A-scans at each inspection position need to be stored for later processing and display. Accordingly, the analogue A-scan signals must be converted into a string of numbers by a process known as digitisation, which consists of sampling the analogue signals at regular intervals and then digitising by an eight-bit waveform digitiser. The amplitude of each sample along with the position and sign or phase information are passed to the processing unit or the computer for storage and processing.

In order to represent the frequency content of the digitised signals in the computer, the analogue waveform must be digitised with a digitising frequency of at least twice the maximum frequency in the waveform, i.e. there must be at least one sampling point in each half cycle of the wave. This is helpful in reconstructing the sampled signals to avoid signal aliasing problem, and it links itself to the well-known Nyquist theorem in communications (called the Nyauist limit or rate).

For reasonable amplitude reconstruction, a sampling rate of at least 5 times the probe centre frequency is commonly used (reliable to within 10% error). Thus, for a typical TOFD probe frequency of 5 MHz, a digitisation rate of at least 25 MHz should be used. Most digital ultrasonic systems nowadays employ a maximum digitisation rate in excess of 100 MHz, and a choice of several subdivisions of this maximum value. The use of higher digitisation rates than essential does not harm the process of measurement and gives rise to a better picture of the true A-scan shape, and hence, a higher resolution is acheived. The only drawback is that this may increase the size of the stored data, but with the advent of high capacity storage disks, this drawback has been largely overcome.

2.5.8 Pulse width control

An ultrasonic TOFD probe contains a piezo-electric crystal which vibrates when a voltage pulse is applied across it and, consequently, it produces a burst of ultrasound. The voltage pulse is produced by a transducer driver which produces a rectangular pulse with the adjustable pulse width (usually between 25 and 500 ns). The used voltage is in the range from 100 to 400 Volts, and is generally dependent on the probe frequency and the type of crystal element.

The pulse width is used to control the shape of the received signal. The first edge of the rectangular pulse sets the crystal element into oscillation while the second edge also sets the crystal element into oscillation again but the phase of the burst of ultrasound is 180° out of phase with the first set of oscillations. The two bursts of ultrasound generally overlap and interfere with one another.

Altering the pulse width causes cancellation or reinforcement of parts of the various cycles. If the two bursts of ultrasound where composed of a single frequency and the pulse width is set to one half of the period (100 ns for 5 MHz), then reinforcement takes place and a larger signal is obtained. If the pulse width is set to one period of the wave frequency (200 μs for 5 MHz), then after one period the two signals are out of phase and a smaller amplitude signal is obtained, but the ringing is reduced. This is a desirable feature for TOFD applications since in order to resolve signals from the top and bottom tips of small defects the signal should only last for a minimum number of cycles. In general, reducing the pulse width has the effect of increasing the resolution (more details are in Section 4.5).

2.5.9 Pulse repetition frequency

The pulse repetition frequency (PRF) is defined as the rate of firing the transmitter probe, i.e. the number of pulsing or firing the transmitter probe per second. It is generally set by the operator prior to the inspection process. If the scanning speed is relatively fast, then the PRF may have to be set as high as possible in order to ensure there is sufficient time for the data to be collected at the required scanning speed. Therefore, in data collection, the maximum PRF available in the data acquisition system is advisable to allow accurate volumetric coverage. Some data collection systems collect blank A-scans if there is no sufficient time at each sampling interval to collect the data. This can be avoided by:

- Reducing the scanning speed,
- Increasing PRF,
- Reducing the number of averages (Section 2.5.10),
- Reducing the length of A-scan to be digitised, or
- Reducing the digitisation rate (or the sampling frequency).

In certain circumstances, the sound waves can be reflected around the sample and appear at the receiver at a time which is after the next successive transmission pulse. This may give false signals (sometimes called ghosting effect) and must be avoided by reducing the PRF appropriately. On the other hand, low PRF selection can cause missing scan lines in the collected data. The maximum PRF available in TOFD commercial equipment is 15 kHz.

2.5.10 Filtering and averaging

As mentioned previously, the data acquisition system is often electrically noisy and there may be external electrical noise as well. Therefore, filtering the spectrum of frequencies is necessary and is performed using low-pass and high-pass filters in order to restrict the frequency band pass based on the ultrasonic probes being used. In practice, the minimum recommended range of the receiver bandwidth is between 0.5 and 2 times the nominal probe centre frequency, which is 2.5 MHz - 10 MHz in the case of 5 MHz probes.

Filtering improves the SNR on the expense of eliminating some spectrum component which may be useful in the classification of various defect classes.

As a way to reduce the electrical noise, an averaging process is recommended. Much of the noise is often due to random electrical signals which are picked up by the acquisition system and hence, this can be reduced by averaging a number of adjacent scans and use the average instead. If N successive A-scans are added together and the resultant sum is divided by N, then the SNR of a genuine signal over random noise is increased by square root of N. The consistent signal stays the same while the noise is reduced. This process is accomplished most effectively in the digitiser unit although it is often set on the acquisition software which generally allows averaging in factors of 2 and up to 256. A typical value would be N=16, which would provide a SNR enhancement of 4. If the signals are very noisy, then a factor of 256 may be necessary but because of the square root effect, the improvement factor is only 16. Thus, increasing the number of averages does not produce a linear increase in the SNR.

Signal averaging is very important for the collection of good quality diffraction.

Therefore, high signal averaging may be recommended provided that this is not affecting the scanning speed. When the noise nature is more complicated than just an electrical noise, or it is coherent rather than random, averaging may not be effective and enough, and in this case, more intelligent techniques are advisable. More details will be shown later in Section 3.2.1.

2.5.11 Calibration

Calibration is a part of the inspection procedure, and it incorporates carrying out a scan over a reference sample. It provides a record for the operator that the system works as specified during the inspection. It also helps to prevent mistakes and ensure that the operator is inspecting the correct depth range with the right parameters and probes. Calibration should be done before and after the inspection process (called pre- and post calibration)). The calibration provides the following:

- Checking the probes, leads and all electronics of the acquisition system and its peripherals.
- Reducing errors before inspection by giving the operator a chance to select suitable parameter values, e.g. correct PCS value.
- Post calibration ensures the inspection is valid. If anomalies are discovered, then the inspection should be repeated or justification provided.

Calibration samples must have known thicknesses and defect locations and sizes. They may also be required to demonstrate other TOFD characteristics like precision and resolution.

2.5.12 TOFD Software

The available software to operate most commercial TOFD inspection systems are very similar. These software provide the following capabilities:

a) Capturing, collecting and displaying the unrectified A-scans.

b) Facilitating setting up and altering all the ultrasonic and collection parameters.

c) Entering all data pertinent to the inspection (e.g. weld number, operator name,...etc) for entry into the file header information of the collected data.

d) Saving all the relevant inspection parameters for retrieval at a later date.

e) Controlling motor and encoder interface.

f) Displaying the B- or D-scan images and extracting and displaying individual A-scans.

g) Providing linear and parabolic cursors for the purpose of flaw sizing and positioning.

h) Displaying facilities such as scrolling, magnification of selected areas, contrast enhancement and cursor facilities for sizing selected indications.

These software do not provide any automatic interpretation information about flaws (e.g. type of flaws, size and location of flaws,...etc). All interpretations are done manually (and off-line) by a trained and skilled operator. In simple words, these software can be considered as just viewing tools that help in retrieving the

scans and their information. Till now, there is no comprehensive automatic tool that can provide automatic interpretation of the collected scan files.

Examples of some of the available commercial software are TomoView™ from Olympus and TD-Scan™ from AGR Field Operations.

2.6 TOFD features and limitations

2.6.1 TOFD features

TOFD is a powerful NDT technique, not only because of the accurate defect sizing capability but also detection in routine inspections. It has many advantages compared to conventional ultrasonic techniques (e.g. PE), which make it one of the preferable techniques in weld inspection. Some advantages of the technique are listed below [5, 24, 26, 30, 39, 48]:

a) Various evaluation projects have demonstrated that the technique combines a high POD (up to 95%) with a low FCR.

b) Defect height can be exactly determined, thus it is most suitable for monitoring growth or changes in previously known defects. It has a through wall sizing accuracy of ±1 mm and a crack growth monitoring capability of ±0.3 mm.

c) It is efficient in detection of all types of known defects.

d) It provides a permanent digital record of the inspection data with cross-section type views through the material.

e) Defect detection does not depend on the orientation, in contrast to the other techniques.

f) It offerers a relatively short inspection time because an entire volume can be inspected with a single pass along the inspection line. Accordingly, the accompanied cost is less than those of other testing techniques.

g) It is safe for the environment because it is radiation-free and does not need area evacuation.

h) The inspection can be performed at elevated temperatures (above 200° C).

2.6.2 TOFD limitations

Like any other NDT technique, TOFD suffers from some problems and limitations. The following are the common ones:

a) Critical stages of TOFD data interpretation are still performed off-line and manually by a human operator.

b) Interpretation can be actually a time-consuming and painstaking process, requiring high operator skills, alertness, consistency and experience, and accordingly, errors happen.

c) TOFD data acquisition and display configurations may sometimes introduce errors that cause a reduction in the acquired data quality, hence incorrect interpretation.

d) It suffers from a noticeable sizing error of off-axis flaws (that are not lying on the centre line between the transmitter and receiver probes) with D-scans due to the acquisition software misinterpretation.

e) Detection and sizing of surface and near-surface cracks are always a weakness in TOFD inspection systems because they may be masked by the lateral wave (it is called the blind zone). The same thing can be said for flaws near the backwall.

f) It is less suited to coarse-grained materials like austenitic stainless steel.

g) The amplitude of the diffraction signals does not depend on the size of the defects and a simple amplitude threshold can not be applied for selecting the important reportable defects (unlike PE inspection).

h) TOFD data interpretation is highly susceptible to noise. The acquired signals are of low amplitude and a gain must be provided by the equipment to amplify the signals. The noise will be amplified accordingly in this case.

i) Operators need to be highly trained and skilled.

Many of the above limitations are not serious and can be overcome. There has been a great evolution in the last few years in the development of TOFD transducers and data acquisition hardware to increase the reliability of the technique and reduce data errors.

It is among the main objectives of this research to propose signal processing algorithms and novel methods to overcome some or all of the serious limitations of TOFD. To achieve this goal, many automation algorithms and procedures are proposed along with the utilisation of the mode-converted waves to solve the problem

of sizing accuracy of surface, near-surface and off-axis cracks. Also, the research proposes some data quality enhancement techniques to minimise interpretation errors. More details of these remedies will be shown later in Chapter 6.

2.7 TOFD applications

NDT forms one important part of the QA procedure in assessing the quality of a welded joint. It is used mainly to detect any internal defects or imperfections within the weld joint itself. TOFD has proven to be a NDT method of choice for weld inspection. It has been adopted by industries such as petrochemical, nuclear, energy and others, and applied successfully to a wide range of applications such as pipelines inspection and for structural integrity of materials in general.

TOFD can be used as a technique for pre-service and in-service NDT. In this regard, the main uses are:

a) For accurate flaw sizing, since TOFD is one of the most accurate techniques especially for internal defects.

b) For screening and sizing. Since TOFD can detect all the flaws in the beam coverage irrespective of orientation, it has a high POD (as mentioned previously). The fact that inspection data is collected in B- or D-scan form also improves the detection of cracks in the presence of signals from geometric features such as mismatch, and weld defects such as excess penetration or undercut. Most welds can be rapidly screened by TOFD and checked whether they are free of significant flaws.

c) Change monitoring. TOFD is one of the most accurate methods available for measuring the growth of flaws.

Furthermore, TOFD can be used to observe and report microscopic degradation caused by fatigue, stress and chemical attacks. It can be used also to measure material thickness with high accuracy. Finally, TOFD can be used with some complex geometries such as railway tracks.

2.8 TOFD standards

The increasing interest in TOFD as a reliable NDT technique for accurate flaw sizing and positioning has led national, regional and international standardisation organisations to the development of many standards such as the British Standard BS 7706 [3], the European Standard EN 583-6 [63], the European Standard EN 15617 [64] and the International Organization for Standardization Standard ISO/DIS 10863 [65]. In addition to these standards, technical specifications such as CEN/TS 14751 [66], and inspection codes such as ASME XI [20] were developed. Furthermore, standards for automatic inspection such as ASTM E-1961-98 [67] and API 1104 [68] are heavily relied on and widely quoted. These standards and codes are highly recommended to ensure high POD and repeatability of sizing and positioning results.

British Standard BS 7706 [3] describes the theory of the TOFD technique and the criteria for selection of ultrasonic probes as well as the data acquisition configurations adopted. It also discusses the various sources of error and their effect on the

accuracy of the results. Most importantly perhaps, it provides detailed procedures and recommendations for the interpretation of the TOFD returns.

European Standard EN 583 [63] is introduced by the European Committee for Standardisation (CEN), and consists of six parts, with the final part devoted exclusively to TOFD. European Standard EN 15617 [64] specifies acceptance levels for TOFD of full penetration welds in ferritic steels from 6 mm up to 300 mm thickness.

International Organization for Standardization Standard ISO/DIS 10863 [65], which is the latest in this regard, specifies the application of TOFD technique to the semi- or fully automated ultrasonic testing of fusion-welded joints in metallic materials of minimum thickness 6 mm. It applies to full penetration welded joints of simple geometry in plates, pipes, and vessels, where both the weld and parent material are low-alloyed carbon steel. The standard permits assessment of TOFD indications for acceptance purposes. This assessment is based on the evaluation of transmitted, reflected and diffracted ultrasonic signals within a generated TOFD image.

The ASME Code [20] (Sections V, VIII and XI) describes the acceptance criteria for accurate defect sizing, as well as providing interpretation criteria for the most serious planar flaws.

ASTM standard E-1961-98 [67] covers the requirements for mechanised ultrasonic examination of welds inspection.

The API 1104 [68] standard also covers the procedures for ultrasonic testing as well as the acceptance standards to be applied to production welds inspected by

ultrasonics.

It should be mentioned that the above standards were taken into consideration when the work in this project was developed.

2.9 Overview of the proposed automatic TOFD data interpretation system

Although methods such as robotic scanning and computer-aided data acquisition are routinely used with ultrasonic TOFD, the critical stages of data processing and interpretation are still performed off-line and manually, depending heavily on the skill, experience and consistency of a trained operator. Mission-critical industrial applications have increased the pressure to complete the interpretation of inspection data in near real-time. This is, in fact, an important reason behind motivating researchers to develop computational tools that are capable of aiding the operators by automating the interpretation process.

The automation of TOFD data processing is an essential stage of a comprehensive inspection and interpretation system. In order to perform this task, advanced signal and image processing techniques are required to build interpretation algorithms that can function autonomously without the need for continuous intervention. This can be done through automatic configuration of the critical interpretation parameters according to the nature of the data and the acquisition settings.

An automatic interpretation system processes an inspection data file, which contains in its header scan information along with system's parameters and workpiece

specifications. Accordingly, no further inputs may be needed to the automatic interpretation system. The anticipated output of the system would be a report highlighting flaws (if any), their sizing and positioning information and their types. The system may offer some recommendations to the operators like performing further B-scans or off-set D-scans, repeating the scan,...etc.

A typical automatic interpretation system starts with pre-processing stage which provides initial processing to the input scan file. In TOFD, detection, sizing, positioning and classification of flaws are highly dependent on the quality of the collected data. Noise is such one important factor that affects the data quality and intelligent and effective techniques need to be devised to reduce or eliminate its effect without modifying the original data. Other pre-processing procedures may include adding gain to the received inspection signal, drift correction, scan alignment and enhancing the reference signals (e.g. lateral wave and backwall echo) that are used for accurate sizing and position purposes, among others.

The next stage includes detecting (highlighting) potential flaws in the scan image file. The output of this stage in the form of defect blobs is to be fed to two subsequent stages: sizing and position stage and classification stage. Sizing and positioning process is responsible for finding the dimensions and locations of flaws inside the component under test. Classification stage tries to identify the class of each flaw from a group of known types. It should be mentioned that new standards start to emphasise on the fact that sizing and positioning information is considered as an important input to the classification stage and future trend is to classify flaws according to their dimensions and locations only. The last stage is post processing that applies general steps to integrate a comprehensive output from all the previous stages by generating a user-friendly visual report which contains all the relevant

information. The report may also contain suggestions and recommendations to the inspectors for future scans. Post processing can apply acceptance criteria to check whether the obtained results match the standards.

It is worth mentioning that, as of now, such system is not meant to replace human operators but rather to act as an aiding tool for double checking the interpretation and to help in decision-making. Accordingly, the overall interpretation time would be less. A commercial realisation of such system that can process different scan files and component dimensions and shapes automatically has not been implemented yet. Accordingly, there is a real need to build such system, which can be considered as a breakthrough in TOFD data interpretation field. This research has developed a pilot of such system that is capable of generating an automatic inspection report readily understood by people that are not routinely involved in ultrasonics with a friendly GUI. Further details will be shown later in Section 7.6.

Figure 2.10 shows a block diagram of the proposed automatic TOFD data interpretation system, with all relevant stages and sub-stages. Details of these along with the incorporated methods and techniques will be shown in the next chapters.

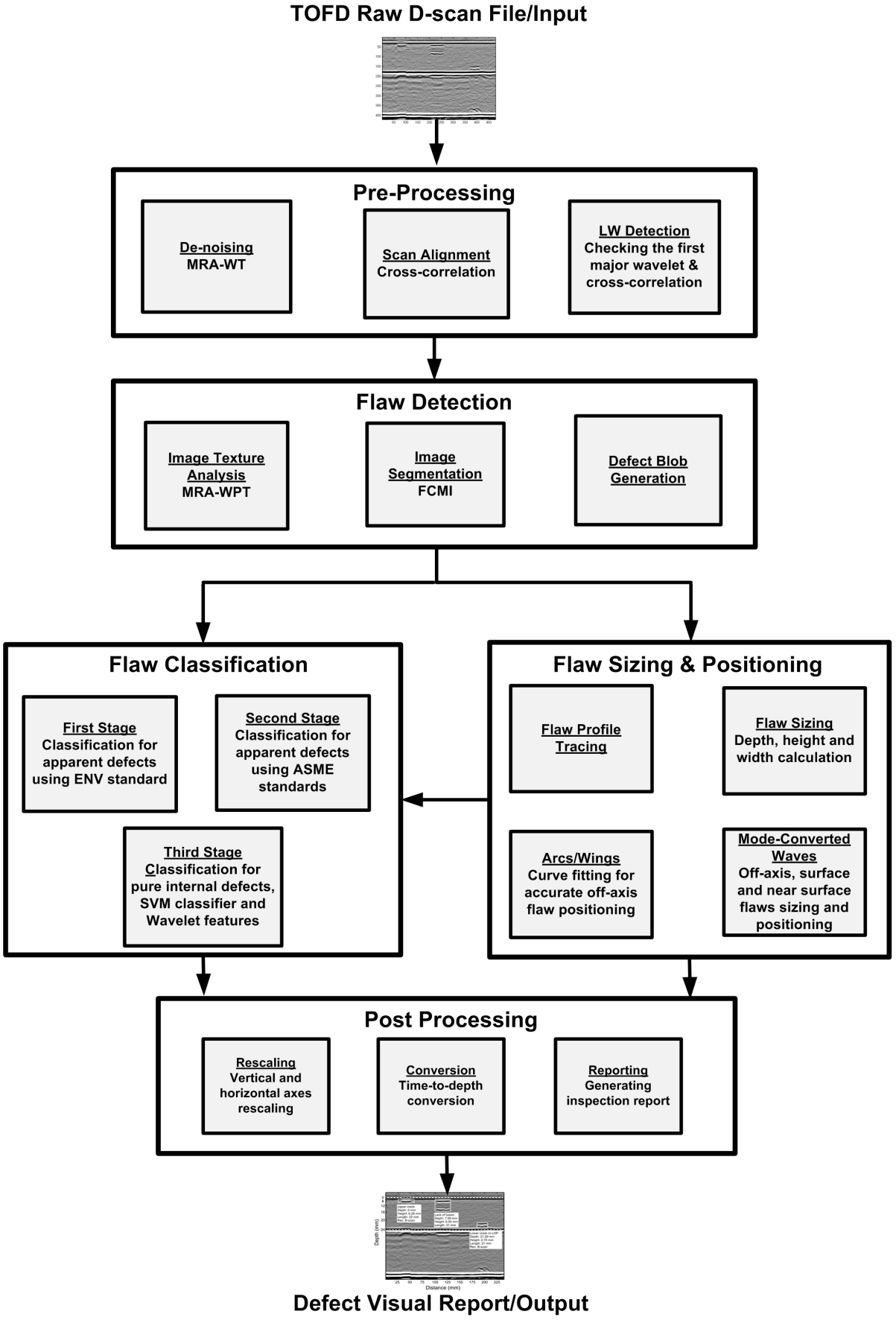

FIGURE 2.10: The proposed automatic TOFD data interpretation system

2.10 Summary and conclusions

This chapter has illustrated the concept of ultrasonic TOFD, its system and data acquisition parameters, features, limitations, applications and standards. The chapter has introduced also the concept of automatic TOFD interpretation system with its stages and the anticipated output. Such system is needed to aid the inspectors in decision-making and to reduce the total interpretation time. A commercial automatic TOFD data interpretation system is not implemented yet.

Chapter 3

Pre-Processing and Automatic Flaw Detection in TOFD Data

3.1 Introduction

Pre-processing is an important step in order to prepare the collected TOFD data for subsequent processing. Its impact is very tangible when it comes to building a comprehensive automatic interpretation system using computer algorithms. The collected TOFD data from the data acquisition system is in need of significant processing and enhancement in order to make it useful for automatic defect evaluation specifically when noise and other factors are present. The TOFD data acquisition and display configurations themselves may introduce sometimes a host of errors that can not be accounted for by manual interpretation, leading to reduction in the quality of the acquired data. Automatic data processing is often made difficult by this reduction in data quality, as indications due to small but potentially dangerous defects may be masked sometimes. This chapter presents the

techniques developed to pre-process TOFD data. It also presents the techniques used to detect flaws automatically in D-scan TOFD images.

3.2 Pre-processing of TOFD data

The proposed pre-processing of TOFD data includes noise suppression (de-noising), scan alignment and accurate detection of the lateral wave. These operations can be performed in an automatic way to minimise both the inconsistency and error introduced by human factors without reducing the spatial resolution of the acquired data. Effective quality enhancement and pre-processing facilitate successful and accurate automatic defect detection and subsequent classification, positioning and sizing.

3.2.1 De-noising through Wavelet transform and the multi-resolution analysis

Noise formed from scattering of inhomogeneous micro-structures and electronic circuitry contributes as a main source of errors. The removal of noise from noisy data while preserving useful information to obtain a filtered signal is often referred to as de-noising. Due to its computational efficiency, multi-resolution analysis (MRA) is considered as a powerful tool to enhance the SNR of ultrasonic TOFD signals.

There are several powerful tools in signal processing, of which Fourier transform is considered one of the most important. Fourier transform consists of breaking

down a signal into constituent sinusoids of different frequencies, and this is enough for the characterisation of a number of signals. However, Fourier analysis has a serious drawback which is when transforming a signal to the frequency domain, time information is lost. If a signal does not change much over time (a stationary signal), then this drawback is not very important. Nevertheless, most interesting signals contain numerous non-stationary or transitory characteristics. These characteristics are often the most important part of the signal, and accordingly, Fourier analysis is not suited for detecting them [69]. The Wavelet transform (WT) was developed especially to overcome these deficiencies, offering an inherent MRA that can be used to obtain the time-frequency representation of the ultrasonic signal [70, 71, 72, 73]. It is a windowing technique with variable-sized regions, which allows the use of long time intervals where more precise low frequency information is required, and shorter regions where high frequency information is required. The Wavelet transform breaks down a signal into shifted and scaled versions of the original (mother) wavelet. The continuous Wavelet transform (CWT) is defined as the sum over all time of the signal, $f(t)$, multiplied by scaled and shifted versions of the Wavelet function ψ:

$$C(scale, pos) = \int_{-\infty}^{\infty} f(t)\psi(scale, pos, t)dt \tag{3.1}$$

The results of the CWT are many Wavelet coefficients C, which are function of scale and position. Multiplying each coefficient by the appropriately scaled and shifted wavelet yields the constituent wavelets of the original signal.

The coefficients produced at different scales by different sections of the signal constitute the results of a regression of the original signal performed on the wavelets. The higher scales correspond to the most stretched wavelets. Thus, for higher

scales, a longer portion of the signal is compared with a more stretched wavelet. This allows noticing the low frequency and thus slow changes and coarse features are measured by the Wavelet coefficients. Similarly, for low scale, compressed Wavelets are used which allows noticing the abrupt changes and details, that is, observing high frequency [57, 69, 74].

For image processing purposes, the Wavelet transform can be thought of as the cross-correlation of an image with a set of wavelets of various scales. The maximum response of the correlation is obtained when the characteristic size of the feature of interest equals to wavelet size. Hence, it is so important to select a suitable wavelet that expose the required features. Among its many applications in image processing, Wavelet transform can be used for noise suppression or de-noising, image coding and compression.

In mathematics, Wavelet analysis refers to the representation of a signal in terms of a finite length or fast decaying oscillating waveform (known as the mother wavelet) [74]. This waveform is scaled and translated to match the input signal. In this way, it is possible to split local and global dynamics for a signal, i.e. low- and high-frequency contribute in a frequency domain, by the MRA in the Wavelet domain, less sensitive to noise than other transforms (e.g. Fourier transform) [70, 72]. MRA can be applied to the analysis of both one- and two- dimensional signals, in order to retrieve features useful to characterise relative trend into the time-, spatial- or frequency-domain.

Indeed, a wavelet has the characteristics of a band-pass filter and the Wavelet transform has the properties of a continuous filter bank with a constant voltage. Wavelet noise filters can be built using the continuous or the discrete Wavelet transform (DWT). In the continuous case, CWT of a signal $f(t)$ (A-scan signal

in this case) is calculated, generating the Wavelet coefficients, then applying an algorithm which chooses the coefficient vectors that should be set to zero [70, 71, 72, 73]. Because the energies of the ultrasonic signals are concentrated in a frequency band, all other frequencies are represented by very low amplitudes in the transform domain, and can be omitted without any loss of information. After the omission of the low amplitudes coefficients, inverse transform is applied to get a de-noised time domain signal.

The de-noising procedure used in this project is based on the decomposition of a signal by DWT in N levels using band-pass filtering and decimation to obtain the coefficients (see Figure 3.1). The global dynamics of an NDT-related signal $f(t)$ are condensed in the Wavelet approximation coefficients (WACs) at the higher multi-resolution level J; if the inspected signal is measured in the time- or spatial-domain, then it is possible to affirm that WACs are related to the low frequencies. On the other hand, local oscillations of $f(t)$ are depicted in a set of so called Wavelet details coefficients (WDCs) at different scales $j = 1, 2, ..., J$; they are related to the high frequencies of a time- or spatial-domain signal. After using the DWT to get the WACs and the WDCs, the next step is thresholding of some WDCs and reconstruction of the signal from the other WDCs and WACs using the inverse transform (IDWT).

This method is a generalisation of wavelet decomposition that offers a larger range of possibilities for signal analysis. In Wavelet normal analysis, a signal is split into WACs and WDCs. The approximation is then itself split into a second-level approximation and detail, and the process is repeated. In this analysis, the detail coefficients as well as the approximation coefficients can be split. This analysis is called the Wavelet packet transform (WPT) [70, 74, 75]. Hard thresholding is

used for thresholding WDCs. Hard thresholding can be described as the process of setting to zero the elements whose absolute values are lower than the threshold. Usually, global threshold is used in WPT filtering. In this project, a local thresholding was used instead of global thresholding (the obtained SNR for local thresholding was higher). The threshold is computed from WDCs at each level of decomposition and used for thresholding at the same level. The used local threshold value is based on the standard deviation and is calculated as follows [75]:

$$\Theta = k\sqrt{\frac{1}{N-1}\sum_{i=1}^{N}(D_i - \bar{D})^2} \tag{3.2}$$

where k is a factor related to the ratio of peak value to the RMS value, D_i is the WDC at each level, $\bar{D}$ is the mean value of WDCs and N is the length of each set of details coefficients.

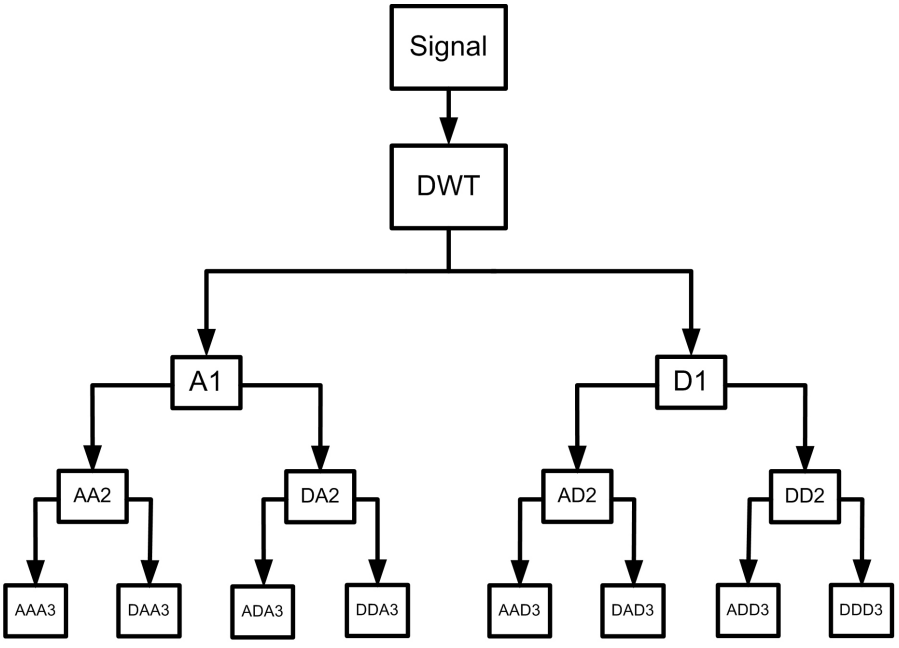

FIGURE 3.1: Discrete multi-resolution scheme-WPT; A is the approximation (low-pass) component and D is the detail (high-pass) component

In order to assess the quality of the suggested de-noising process, the SNR is

computed for different defect samples. The obtained SNR values were calculated using the following equation:

$$SNR_{dB} = 20log\left(\frac{S_{RMSF}}{N_{RMSN}}\right) \tag{3.3}$$

where S_{RMSF} is the RMS value of the filtered signal, and N_{RMSN} is the RMS value of the noise-only part of the raw signal.

In this research, three decomposition levels (L3) are used with Daubechies (db6) as the Wavelet filter. Figure 3.2 shows two D-scan image samples before and after applying Wavelet de-noising method, with a clear enhancement in the corresponding SNR values and visually as well. Although SNR improvement for human interpretation before and after applying de-noising may not appear significant, this improvement is more than adequate in terms of automation and computer interpretation. Performance of the subsequent processing stages in terms of accuracy shows remarkable enhancement after the de-noising process.

It is worth mentioning that other de-noising techniques were also tested and evaluated, like the use of Wiener filter and averaging. When compared with other methods, de-noising through Wavelet transform returned higher SNR values without reducing the spatial resolution of the data, especially when the noise is correlated with the data and not just a simple random noise. De-noising through adaptive Wiener filter technique applies a Wiener filter (a type of linear filter) to an image adaptively, tailoring itself to the local image variance. Where the variance is large, the filter performs little smoothing, and when the variance is small, the filter performs more smoothing. This approach often produces better results than normal

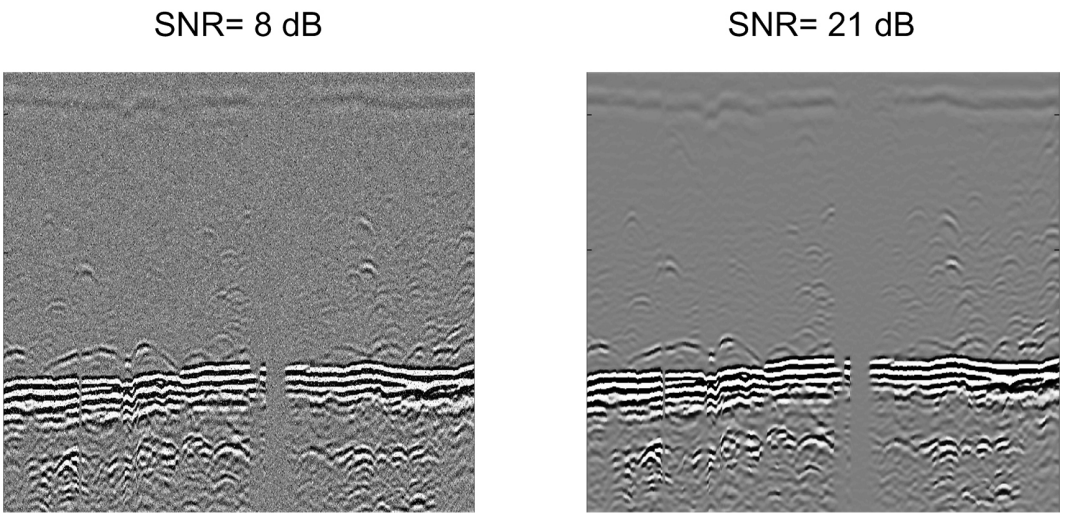

(a) De-noising example 1

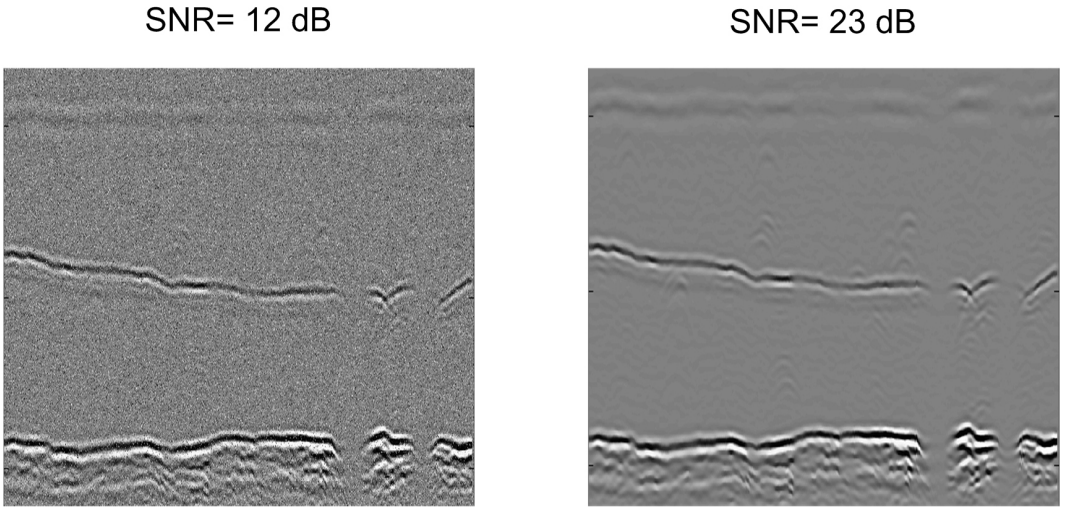

(b) De-noising example 2

FIGURE 3.2: Sample of de-noising results

linear filtering. The adaptive filter is more selective than a comparable linear filter, preserving edges and other high-frequency parts of an image. The filter works best when the noise is constant-power (white) additive noise, such as Gaussian noise. One draw back of the adaptive Wiener filter, however, is that it reduces slightly the spatial resolution of the scan images, which may lead to removing a flaw indication. The filter is tested on scan files and shows comparable results to

de-noising through Wavelet transform, with some favor to the Wavelet de-noising in most of the situations. The weakest de-noising method in terms of both SNR and spatial resolution is the averaging. The three de-noising methods were tested on noisy D-scan images and a summary of findings are shown in Table 3.1.

TABLE 3.1: Comparison in de-noising performance between MRA-WT, Wiener filter and averaging

De-noising method	**Average SNR enhancement**	**Spatial resolution reduction**
MRA-WT	62%	No
Wiener filter	55%	Yes
Averaging	39%	Yes

3.2.2 Other pre-processing steps

In addition to de-noising, pre-processing includes other important operations to improve the quality and consistency of the data to enable accurate subsequent defect detection, characterisation and sizing and positioning. These operations include scan alignment and identifying the accurate position of lateral wave.

Scan alignment is used to align adjacent A-scans and is essential to improve defect sizing and characterisation accuracy. A number of factors may contribute to the misalignment of adjacent A-scans, including couplant thickness variations, surface irregularities, inadvertent changes in probe separation and accidental probe lift-off [5]. Furthermore, far surface irregularities such as counter-bores and lack of root penetration flaws may cause the backwall echo to be misaligned in these places. In order for any defect to be accurately positioned and sized later, the tips of the defects must be accurately located within the material, and the lateral wave and the backwall echo are used as reference points as they are the only known

positions. In this project, scan alignment is carried out by cross-correlating each scan with the first A-scan in the image. The positions of the peaks in these cross-correlation plots are used to automatically shift each A-scan forward or backward in time in such a way as to align the envelope of the lateral wavelets. The effect of this alignment has had not only on the profile of the lateral wave and backwall echo, but also on the shapes of the defect signatures [2]. Figure 3.3 illustrates the effect of scan alignment on the lateral wave. It is worth mentioning that this operation must be performed with careful attention in order not to change or mask the indications of the near-surface and surface-breaking cracks.

Identifying the accurate position of the lateral wave is another important pre-processing operation. In certain industrial applications, the collected scan samples suffer from weak, disturbed or sometimes missing lateral wave. Lateral wave is an important reference point specifically when sizing and positioning is considered. It is also needed for scale linearisation and calibration.

As mentioned earlier in Section 2.4.6, when a longitudinal wave is reflected at the interface between two media from higher to lower acoustic impedance, it undergoes a 180° phase shift. Therefore, when the backwall signal is reflected at the interface between steel and air for example, there is a phase difference of 180° between the lateral wave and this backwall echo. Because of these phase changes, care must be taken when choosing the position for measuring the time of arrival of signals in order to obtain the most accurate results.

To detect the lateral wave, the first major wavelet peak (or trough, depending on the phase) of the A-scan is detected in order to accurately locate the lateral wave. The backwall echo detection can proceed in a similar manner to the scan alignment process. Successive cross-correlations are used to estimate the shift

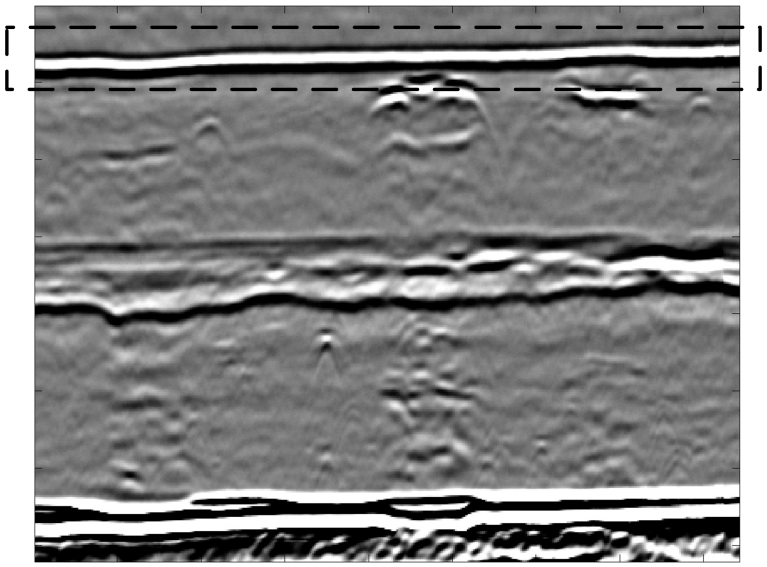

(a) Misaligned D-scan

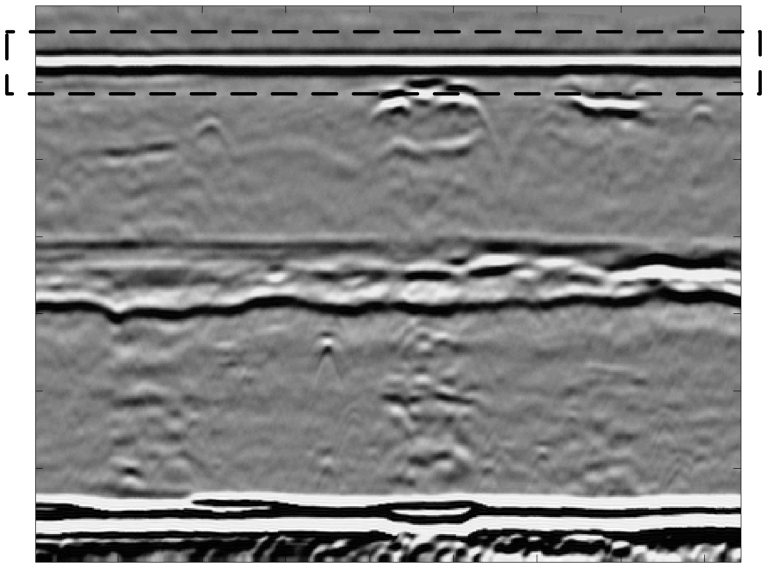

(b) The D-scan after alignment

FIGURE 3.3: Example of scan alignment pre-processing

between adjacent scans, but instead of using this shift to align the A-scan signals, it is used to trace the profile of the backwall across the image.

Once the time profile of the two waveforms is determined, successive detection and tracking of the peaks (for the lateral wave) and troughs (for the backwall echoes) determine their exact positions in time for each scan taking into consideration the relative phases of the two wavelets. Figure 3.4 shows D-scan images that are processed to detect the lateral wave and backwall echo positions. It can be seen clearly from this figure that the profile of the lateral wave (indicated by the black dashed line) and that of the backwall echo (indicated by the white dashed line) have be traced accurately without the need for them both to be level. Accurate positions of the two waveforms will become available for further utilisations (especially for flaw sizing and positioning).

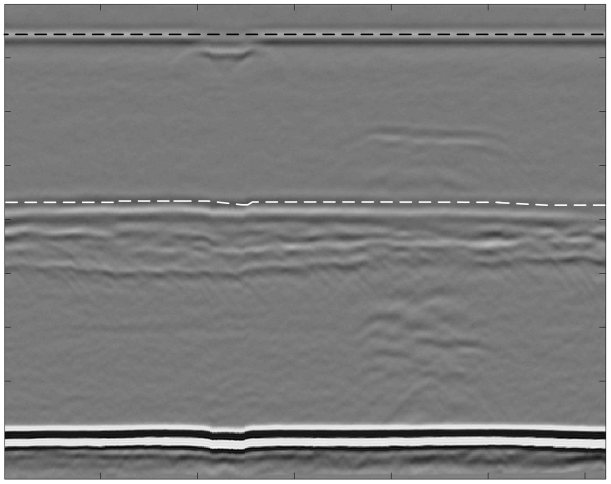

(a) Example 1, lateral wave and backwall detection

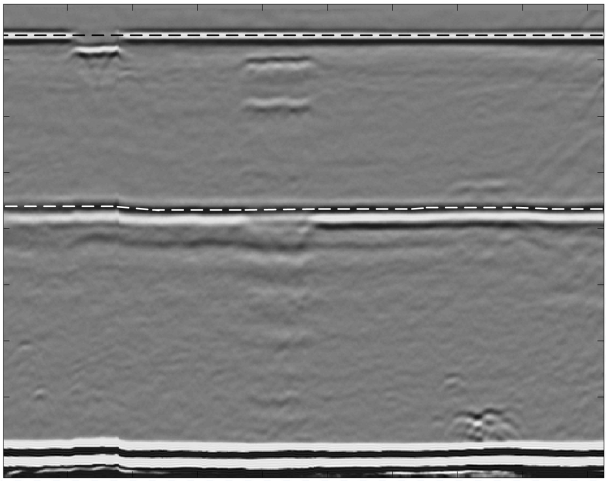

(b) Example 2, lateral wave and backwall detection

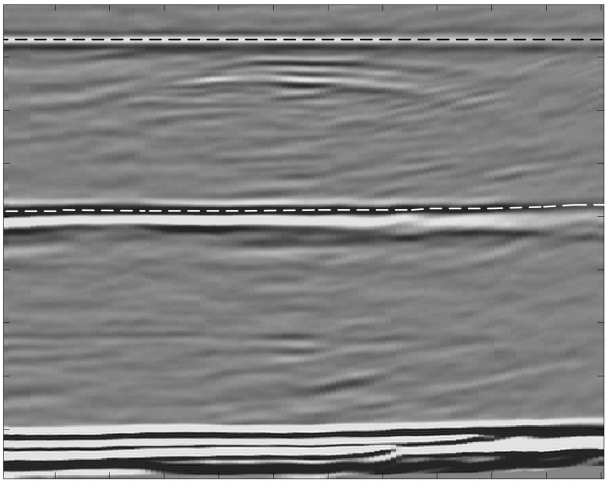

(c) Example 3, lateral wave and backwall detection

FIGURE 3.4: Detection of lateral wave and backwall illustration

3.3 Automatic flaw detection

Automatic defect detection is considered as an essential stage in the comprehensive automatic TOFD interpretation aid. After pre-processing the D-scan images, TOFD data is now convenient for defect detection. With manual interpretation, which relies heavily on a skilled operator, detection stage involves pointing out those image areas containing defects and suppressing others. Generally speaking, this process consumes considerable amounts of time and effort, besides the fact that the reliance on human judgment at this critical stage may invariably introduce inconsistency and error. This section illustrates some techniques to automatically highlight and outline detects in D-scan TOFD images.

The defects constitute only a small fraction of the collected TOFD data (called defect blobs). Highlighting those areas of interest and labelling them as likely defect zones are essentially a task of image segmentation process. Mainly, MRA based on WPT along with texture analysis are used to select the image that is used and processed in detection. Image segmentation can then be performed either by statistical methods or computational intelligence methods.

3.3.1 MRA-WPT for image analysis and selection

As mentioned previously, MRA using DWT is referred to as WPT. The WPT is a signal analysis tool that has the frequency resolution power of Fourier transform and the time resolution power of Wavelet transform [70, 74, 76, 77, 78]. It can be applied to time varying signals where Fourier transform does not produce useful results and Wavelet transform does not produce sufficient results. The WPT can

be considered as an extension to the DWT with better reconstruction process performance [70, 72, 79]. In the Wavelet packet framework, compression and de-noising ideas are exactly the same as those developed in the Wavelet framework. The only difference is that WPT offers more complex and flexible analysis, because in Wavelet packet analysis, the detail as well as the approximation parts are split, as illustrated in Figure 3.1. The tree decomposition in the Wavelet packet analysis can be applied continuously until the desired coarser resolution is reached.

A single Wavelet packet decomposition gives a lot of bases from which best representation with respect to a design objective can be selected. This can be done by finding the best tree based on an entropy criteria [70, 77, 78]. Selection can be done also based on texture analysis and statistical contents of the obtained images. De-noising (as explained previously) and compression are interesting applications of Wavelet packet analysis. This analysis is used in this project in two more important areas. The first area is to aid in flaw detection. The second area is to provide a ground for selecting defect blob features that are used as inputs to the classifier in the flaw classification stage (will be shown later in Section 5.5.2). Both areas rely heavily on the powerful compression ability of the Wavelet transform in general and WPT in particular to extract relevant and descriptive features only. Figure 3.5 shows how the Wavelet transform is powerful in highlighting the important indications and the regions of interest in a D-scan image. It is very obvious that this ability is so important as far as automatic interpretation is concerned.

The application of WPT to the D-scan image is performed to analyse the image into multiple decomposition levels by different analysing mother Wavelets like Gauss, Symlet, Coiffet and Debauchies. In this project, the Debauchies of order 8 (referred to as db8) is used as an analysing function in the WPT process.

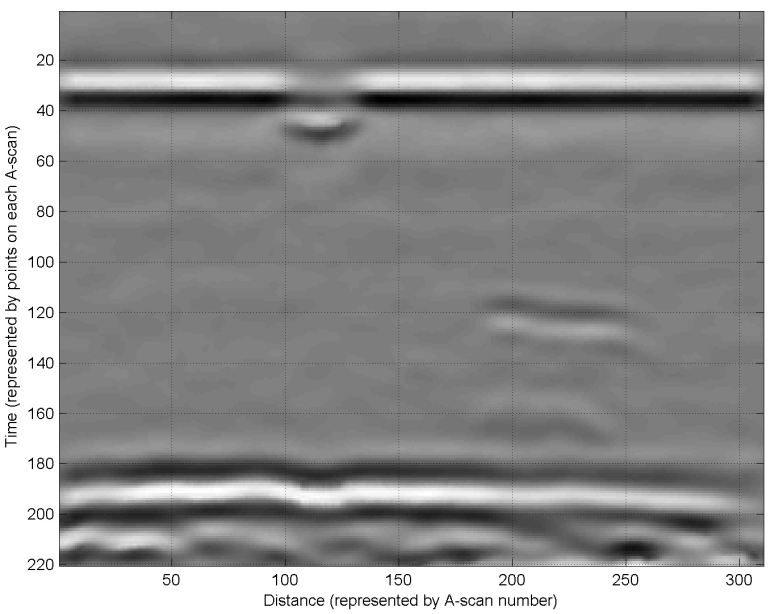

(a) Compression waves region of a D-scan sample

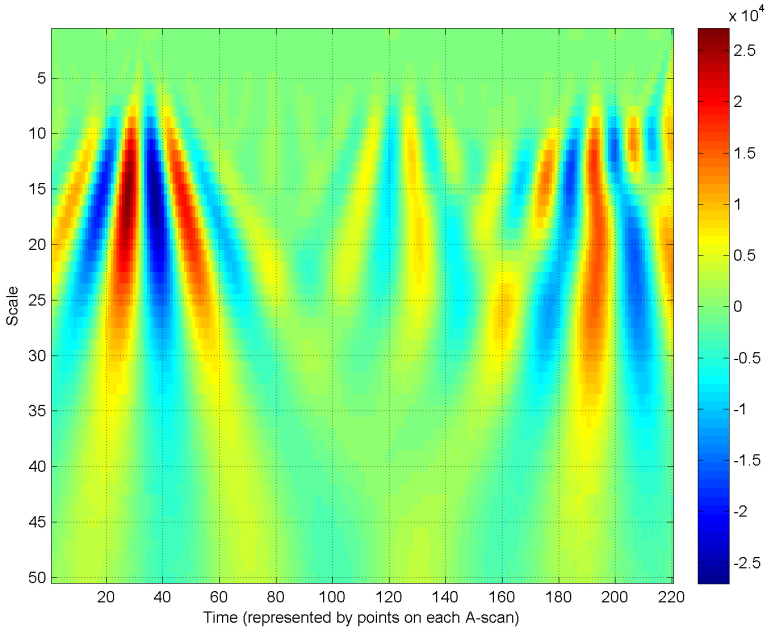

(b) Time-scale representation of the compression waves area

FIGURE 3.5: Wavelet transform view of a D-scan sample containing two defects (near surface and internal cracks)

The chosen level of decomposition is 3 since it achieved the required coarse resolution and higher decomposition levels do not add any significance to the analysis. The decomposition steps are as follows:

a) First, the D-scan image is decomposed by the WPT (db8, L=3) in the first level. The grey-level co-occurrence matrix (GLCM) $P(i,j)$ is calculated for the decomposed images.

b) Second, the descriptors or features that characterise the content of GLCM are calculated. The following are the three descriptors that are used in the selection of the images for reconstruction [80]:

- Contrast:

$$\sum_{i,j} |i-j|^2 p(i,j) \tag{3.4}$$

- Energy:

$$\sum_{i,j} [p(i,j)]^2 \tag{3.5}$$

- Entropy:

$$-\sum_{i,j} p(i,j) log(p(i,j)) \tag{3.6}$$

where $p(i,j)$ is the normalised GLCM $P(i,j)$.

c) Based on these descriptors, the image with the weakest textual information is discarded, and the one with the highest statistical contents is selected and kept.

d) Next, another decomposition level runs to generate the new set of images. The process of calculating the descriptor commences again, and so on. The process of decomposition proceeds until level 3.

e) The final image is reconstructed from three images carrying the highest statistical textural information in the last level. This image is a crucial input for the next stages.

It should be mentioned that the above exercise is applied to the compression waves area only and not the mode-converted waves area (the utilisation of the mode-converted waves will be discussed later in Chapter 6). Figure 3.6 shows the result after the application of 6 levels of Wavelet packet analysis on the compression part of a D-scan sample (Figure 3.6 (a)) that has 3 flaws. It can be seen from this figure that the required coarse resolution has been achieved in the third level, where the background is just a smooth area while defect indications have different texture (especially in vertical detail V3 image of Figure 3.6 (b)). Further levels (4, 5 and 6) do not add any significance to the analysis and just increase computational cost.

After the MRA-WPT analysis for the D-scan image, the next stage is image segmentation to identify the potential defects automatically. For that purpose, two methods are used: statistical and computational intelligence methods.

3.3.2 Segmentation through statistical analysis

Statistical analysis is based on exploiting pixel statistics in a probabilistic sense. It computes local features of each pixel in the image, and derives a set of statistics from the distributions of these local features. The local feature is defined by

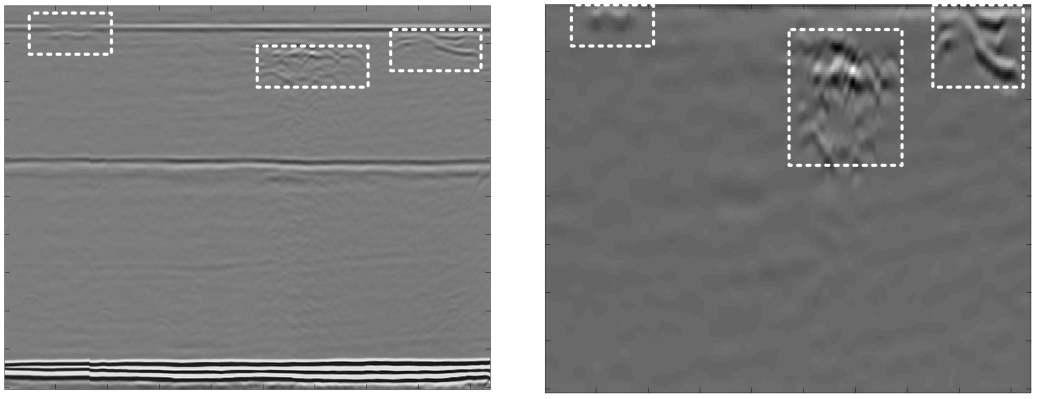

(a) The complete D-scan of a sample and the corresponding compression region only

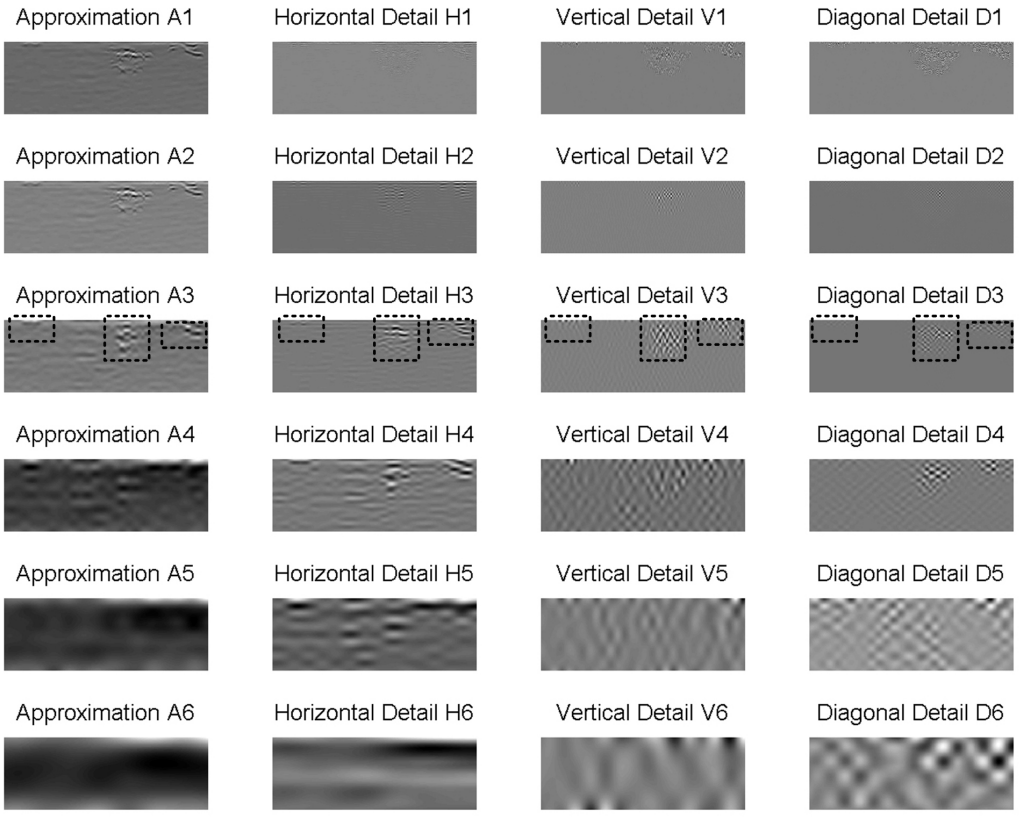

(b) WPT analysis of the compression region

FIGURE 3.6: WPT analysis with L=6 of a D-scan sample

combinations of intensities at specified positions relative to each point in an image. According to the number of points which define the local feature, statistics are either first-order (e.g. histogram mean and variance), second-order (e.g. GLCM) or higher-order statistics.

First-order statistics measure the likelihood of observing a grey value at a randomly chosen location in an image. It can be computed from the histogram of pixel intensities which depends only on individual pixel values. Consider a two-dimensional image I discretised into g grey levels. Let $\theta(i)$ $(i = 1, 2, \ldots, g)$ be the number of points whose intensity is i in the image and A be the area of the image defined as the total number of pixels in that image. The occurrence probability of intensity i in the image takes the form of a histogram and is given by:

$$h(i) = \frac{\theta(i)}{A} \tag{3.7}$$

As different portions of an image may exhibit different visual appearance, this histogram function is computed for small overlapping regions over the entire image, and the resulting distribution associated with the centre pixel of the region. Accordingly, for an $M \times N$ region of an image, the histogram is given by:

$$h(i) = \frac{1}{M \times N} \sum_{x=1}^{M} \sum_{y=1}^{N} \delta\big(I(x, y) - i\big) \tag{3.8}$$

where $\delta(i)$ is the Dirac-delta impulse function.

Two simple statistics are often used to characterise the histogram, namely, the mean and the variance (second moment), which are functions of the pixel intensity distribution $h(i)$ within any $M \times N$ region centred at an arbitrary point. They

are given by:

$$Mean: \ \mu_h = \sum_{i=1}^{g} i\, h(i) \tag{3.9}$$

$$Variance: \ \sigma_h^2 = \sum_{i=1}^{g} (i - \mu_h)^2\, h(i) \tag{3.10}$$

The resultant are feature matrices (or images), each point of which bears some relationship to the probability distribution function of pixel intensities within its neighbourhood.

Automatic segmentation of defects can be performed in this case by analysing the local first order statistical properties of the TOFD images based on the variation in intensity levels between pixels in the defect areas. Local variance has proved to be a successful indicator capable of discriminating the defect areas from the background.

Local statistics are computed for small rectangular windows surrounding each pixel in the image by scanning the compression waves region in a D-scan image using a moving window. The window size (say $m \times n$) must be chosen such that it would be enough to span a spatial-temporal area that contains amplitude variations due to defects, while keeping it small enough to provide an acceptable resolution level. To improve the spatial-temporal resolution more, this window must move with adjacent overlap in the x- and y-axis directions.

The optimum values for m and n are linked to scanning and data acquisition parameters [2]. For example, m is related to the A-scan collection step (the number

of collected A-scans per millimetre) by a factor between 0.6 to 1, while the optimum value for n is found to be equivalent to 3/4 of the ultrasonic wavelength in the medium. This can be computed using the averaging factor, the probe centre frequency, the sampling frequency and the collection step. With a probe centre frequency of 5 MHz, a sampling frequency of 100 MHz, a collection step of 10 scans/mm and an averaging factor of 5, a window of size (6×15) samples can be used with overlapping 3 and 5 samples respectively.

The value of histogram variance for each pixel is calculated and accumulated as the window moves with overlap between adjacent windows to improve the spatial-temporal resolution. The result is an image of cumulative local variance. The areas of defects can be identified based on this image by applying a threshold. A smooth segmentation is resulted from this thresholding. Fully automating this segmentation process requires determining the threshold value automatically, as the statistical properties of the local variance image may vary significantly with a variation in data acquisition settings and material type.

The occurrence histogram of the variance image has two or more distinct peaks with one being larger than the others as shown in Figure 3.7. This larger peak corresponds to the background, while the others correspond to different defects. The grey level corresponding to the first trough between the initial two peaks is considered as the optimal threshold value to differentiate between defects and background. Thus, more than one threshold value is computed for a range of histogram bins, and the lowest value is taken as the optimal threshold. This process ensures that no defect is overlooked. An example of the output is shown in Figure 3.8. After applying this technique, followed by further processing, the result is a segmented image with outlined defects.

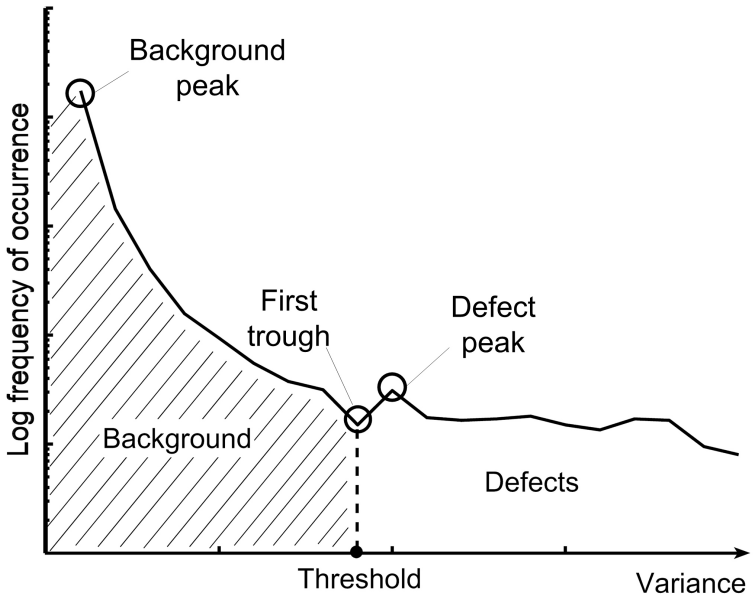

FIGURE 3.7: Logarithmic histogram of intensity in local cumulative histogram variance image [2]

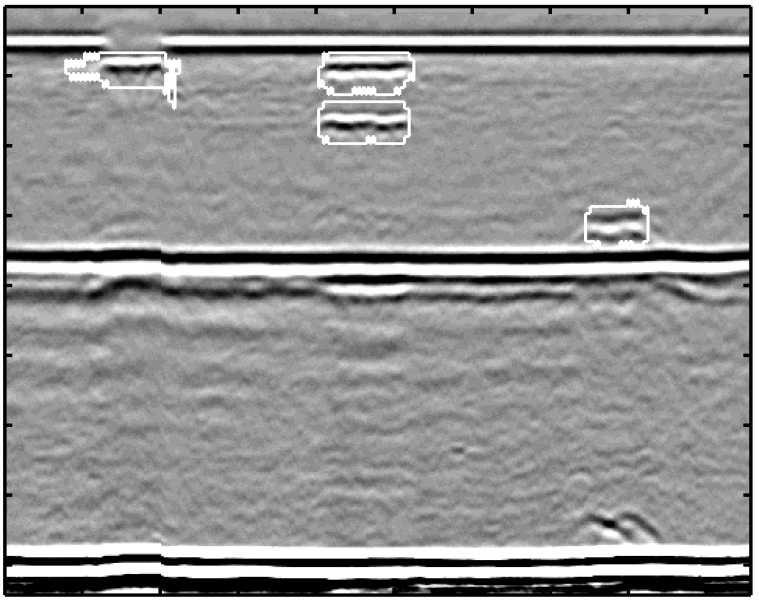

FIGURE 3.8: Segmented image using statistical analysis [2]

3.3.3 Fuzzy logic segmentation

It was found practically after several tests that statistical segmentation technique results in good performance when defects are well-separated and not superimposed. In such situations, segmentation using statistical methods may not be

the best method, and other alternatives are needed. The segmentation technique used in this project to detect defects automatically is based on the use of fuzzy logic, namely segmentation using the fuzzy c-mean iterative (FCMI) algorithm [81, 82, 83, 84]. This method showed better performance in terms of accuracy and automation when compared to statistical thresholding, especially in case of superimposed defects when normal means (visually via trained operator or automatically via statistical methods) can not perform as anticipated. The input to this algorithm is the final image after MRA-WPT (explained in Section 3.3.1). The algorithm acts as a binarisation operation (flaw or background), with black or logic '0' (pixel values set to zeros) represents background and white or logic '1' (pixel values set to ones) represents flaws. The obtained black and white image (or mask) is used to segment the scan image after some further processing.

In order to understand this segmentation operation, the FCMI algorithm needs to be explained. FCMI algorithm uses the concept of fuzzy logic and it is defined as follows [82, 83]:

Consider a pattern space $X = x_1, x_2, ..., x_m$ with the existence of c fuzzy clusters whose centres are unknown and are given the initial values $y_{10}, y_{20}, ..., y_{c0}$. FCMI algorithm iterates and at each iteration, certain patterns' membership values in the various clusters are obtained. The cluster centres are then updated by minimising a performance equation. The process terminates when the difference between two consecutive iterations does not exceed a given tolerance.

a) Input:

- n, the patterns' dimension.
- m, the number of patterns.

- c, the number of clusters.
- X=$\{x_i\}$, $1 \leq i \leq m$ - the given patterns
- Y_0=$\{y_{i0}\}$, $1 \leq i \leq c$ - the initial c cluster centres.
- N, maximum number of iteration allowed.
- ε, a given tolerance (alternatively, a minimum amount of improvement parameter).
- β, a tuning parameter which controls the degree of fuzziness in the process.

b) Output:

- Y=$\{y_i\}$, $1 \leq i \leq c$ - the final cluster centers.
- (χ_{ij}), $1 \leq i \leq c$, $1 \leq j \leq m$ - the final matrix of membership values.
- it, the number of iterations performed.

The steps of the FCMI algorithm are as follows:

- Step 1. Initialisation: set $k = 0$ and $y_i^{(0)}$=y_{i0}, $1 \leq i \leq c$.
- Step 2. For $1 \leq i \leq c$ and $1 \leq j \leq m$ calculate

$$d_{ij}^{(k)} = \left\| x_j - y_i^{(k)} \right\|$$

- Step 3. Fuzzification: For $1 \leq i \leq c$ and $1 \leq j \leq m$ calculate the membership function

$$\chi_{ij}^{(k)} = \left[\sum_{l=1}^{c} \left(\frac{d_{ij}^{(k)}}{d_{lj}^{(k)}} \right)^{2/(\beta-1)} \right]^{-1}$$

- Step 4. Defuzzification: If $d_{lj}^{(k)} = 0$ for some $l = l_0$, set $\chi_{l_0 j}^{(k)} = 1$ and $\chi_{ij}^{(k)} = 0$ for all $i \neq l_0$. For $1 \leq i \leq c$, update the cluster centres, using the following equation (the centre of gravity equation):

$$y_i^{(k+1)} = \frac{\sum_{j=1}^{m} \chi_{ij}^{(k)} x_j}{\sum_{j=1}^{m} \chi_{ij}^{(k)}}$$

  and x_j belongs to the class l_0.

- Step 5. If

$$\left[\sum_{i=1}^{c} \left\| y_i^{(k+1)} - y_i^{(k)} \right\|^2 \right]^{1/2} < \varepsilon$$

  set $y_i = y_i^{(k+1)}$ $1 \leq i \leq c$; $\chi_{ij} = \chi_{ij}^{(k)}$ $1 \leq i \leq c$, $1 \leq j \leq m$; $it = k + 1$; output y_i, χ_{ij} for $1 \leq i \leq c$, $1 \leq j \leq m$, it and stop. Otherwise, continue.

- Step 6. If $k = N$, output (no convergence) and stop. Otherwise, set $k \leftarrow k+1$ and go to Step 2.

As an example of FCMI algorithm, consider the samples shown in Figure 3.9. Assume $c = 2$. The initial approximations for the two cluster centres are $y_{10}=x_1=(2, 3)$ and $y_{20}=x_2=(1, 2)$. The samples in the first cluster are x_1, x_4, x_5, x_6, x_7 while x_2 and x_3 belong to the second one. The first iteration provides the new cluster centres $y_1=(3.4, 1.8)$, $y_2=(1.0, 1.5)$. Since convergence is not obtained, the samples are again classified with respect to the new cluster centres. Now, x_5, x_6, x_7 are in the first cluster and x_1, x_2, x_3, x_4 are in the second. The cluster centres are adjusted to $y_1=(4.3, 1.3)$, $y_2=(1.5, 2.0)$. The next classification yields the same partition of the samples, i.e. the same y_1 and y_2 and the process terminates after three iterations.

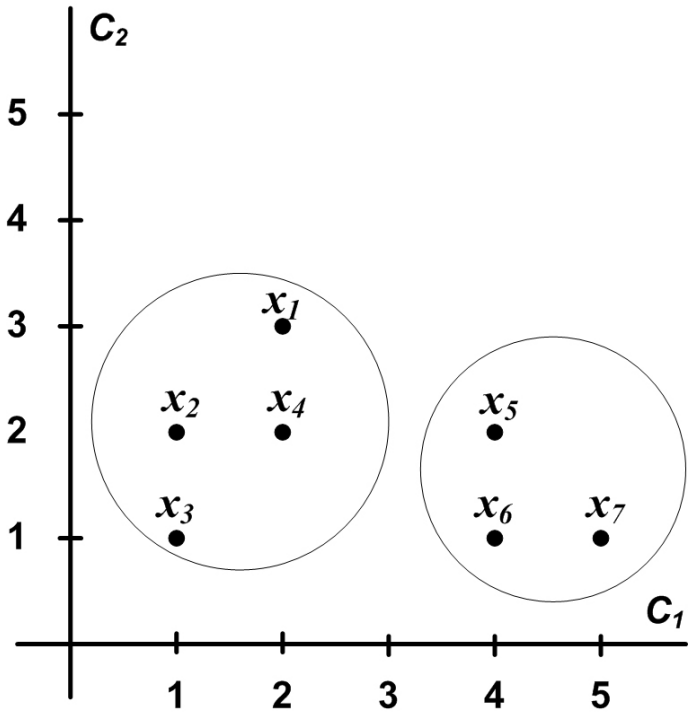

FIGURE 3.9: Applying FCMI algorithm with $c = 2$

For the current purpose, there are two classes: defect (flaw) and non-defect (background), hence $c = 2$. Based on preliminary experiments and research, the value of N was chosen to be 100 and the tuning parameter β for the given exercise was found to be in the range of 1 to 1.05. The minimum amount of improvement parameter ε was chosen to be 10^{-5}. Other parameters required to run this algorithm were chosen automatically depending on the input dimensions.

Segmentation through FCMI algorithm is a method that can be implemented as supervised or unsupervised. In this project, unsupervised implementation is used. After some processing, the output of this step is a segmented image data with highlighted defects areas. An example of the output of this algorithm represented as a mask is shown in Figure 3.10 for an input D-scan file shown in Figure 3.11 (compression waves region only).

For a better representation, each detected defect is outlined by a rectangle to

form a defect blob. This is achieved by applying a global thresholding in order to remove the lowest 10% of the pixel intensity values within the defect blob and then recording the minimum and the maximum spatial and temporal dimensions for each blob [2]. The recorded dimensions are used to generate a new mask with each defect blob represented by a rectangular outline. The defect may consist of more than one rectangular in general. As every defect is to be represented in one rectangular blob, the rectangular blobs related to the same defect must be merged based on the dimensions between the blobs. An output example after applying the above processing is shown in Figure 3.10 (b)

Figure 3.11 shows outputs of segmentation using statistical analysis method (variance thresholding) and FCMI algorithm for a TOFD D-scan file that has superimposed and overlapped defects. It can be seen that the latter method performs better in separating close defects (outlined by different boxes and not just one like the case of variance thresholding). Detection results after using FCMI algorithm were also compared with manual interpretation performed by a trained operator, and its performance was the highest in terms of detection accuracy and verified against scans with documented flaws (ground truth). Table 3.2 shows performance comparison between the three detection methods for close defects.

Table 3.2: Performance comparison between flaw detection methods

Method	**Detection accuracy (close defects)**
FCMI algorithm	85%
Variance thresholding	60%
Manual interpretation	40%

Further examples of outputs of the automatic detection stage are shown in Figures 3.12, 3.13, 3.14, and 3.15, which show high detection accuracy.

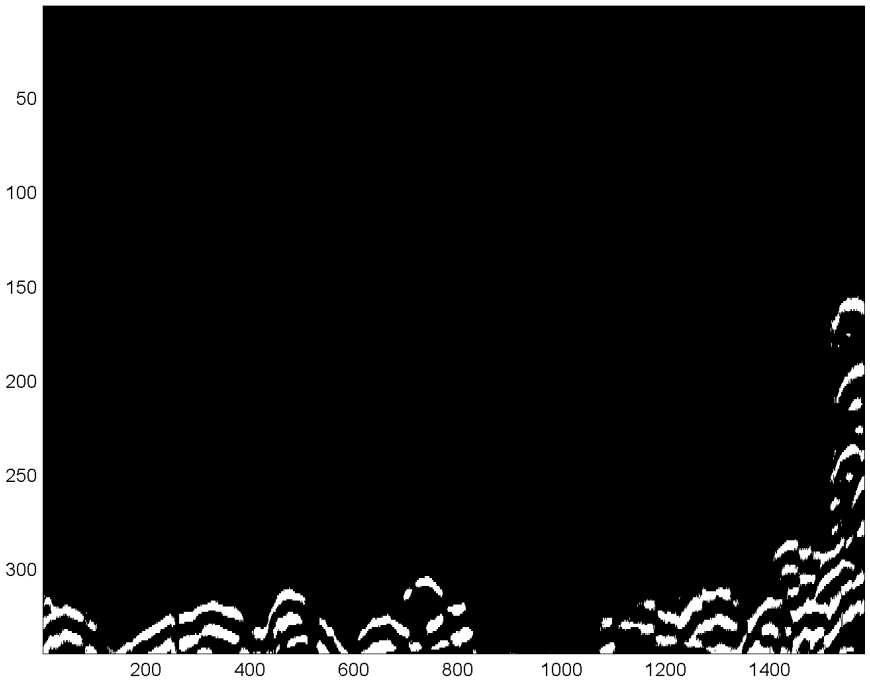

(a) The mask

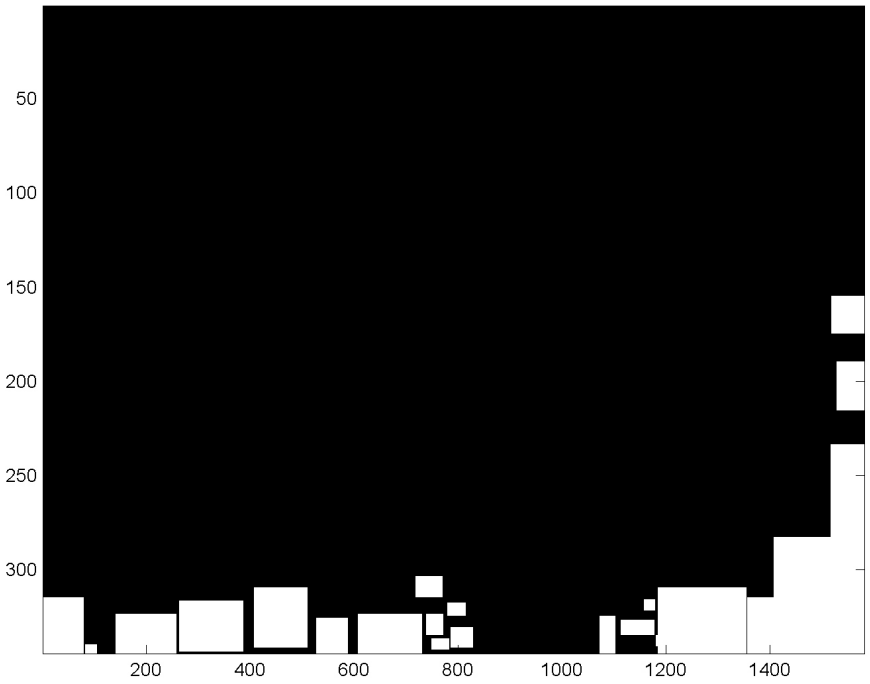

(b) Rectangular merged mask

FIGURE 3.10: The result of the FCMI algorithm in the form of a mask

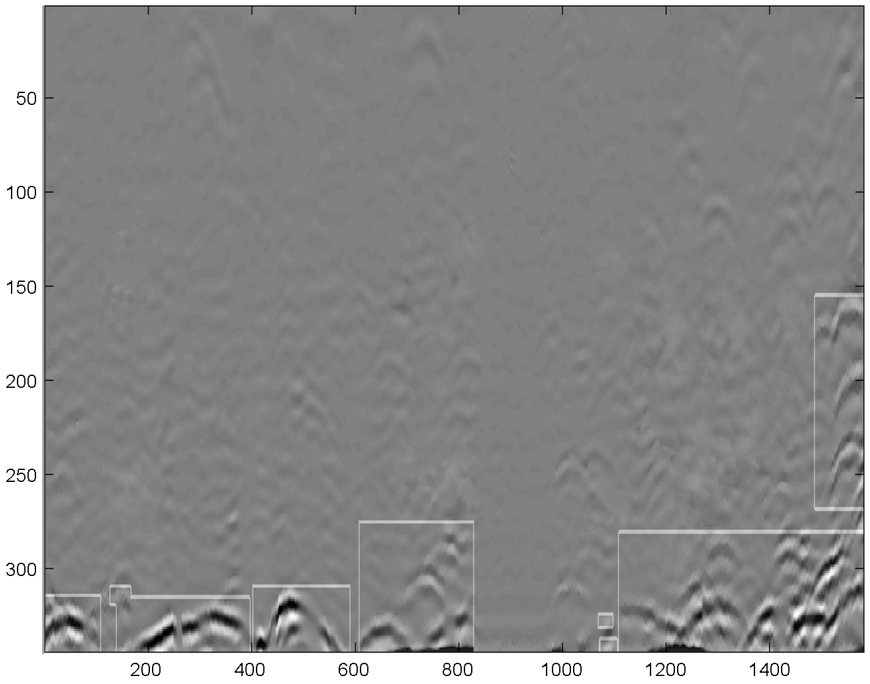

(a) Segmentation using statistical analysis (variance thresholding)

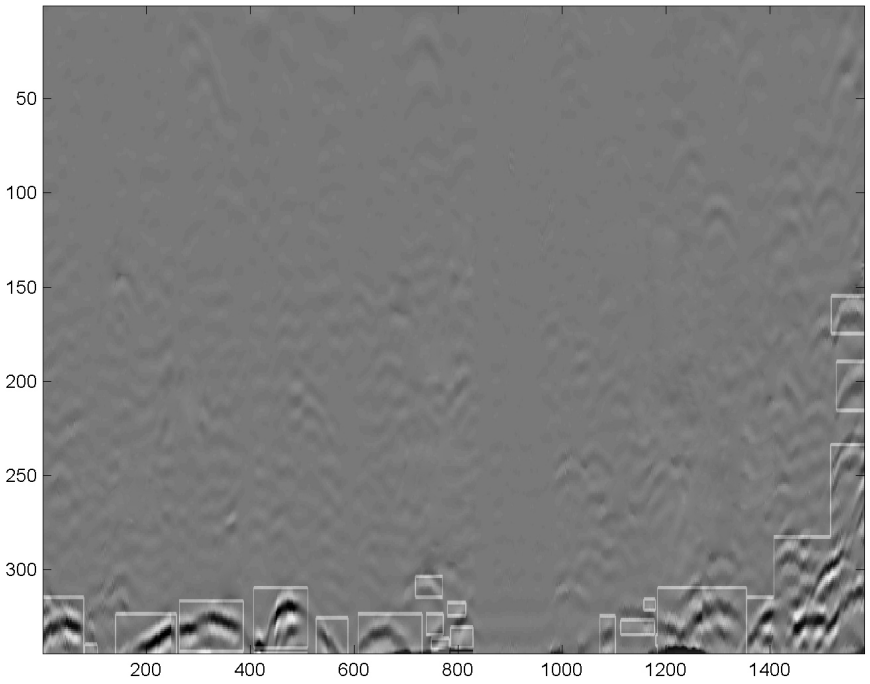

(b) Segmentation using FCMI algorithm

FIGURE 3.11: Segmentation results obtained from variance thresholding and FCMI algorithm

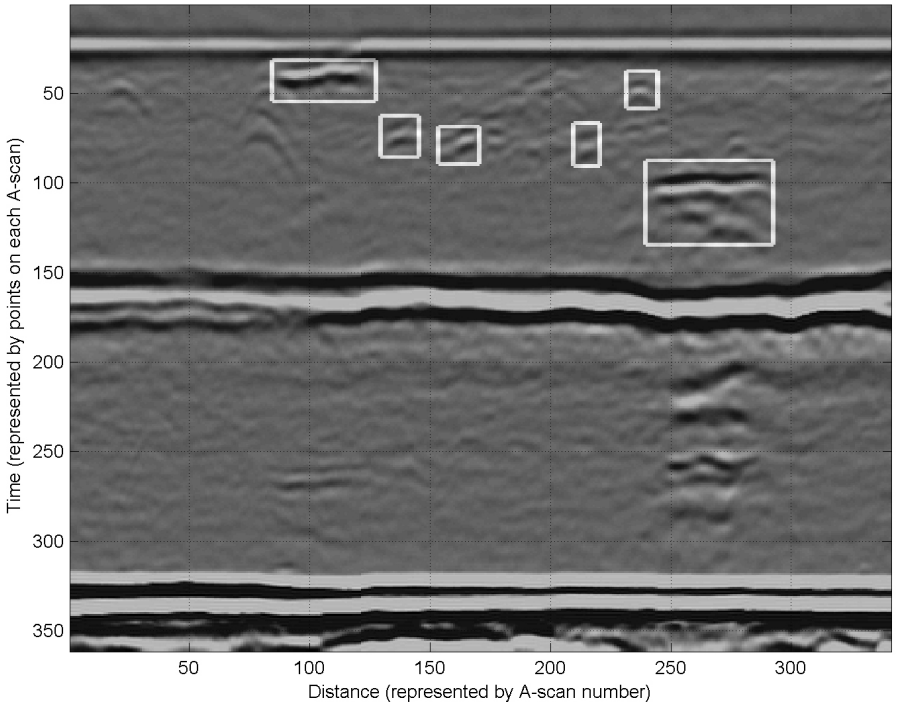

FIGURE 3.12: Automatically detected flaws in a D-scan image

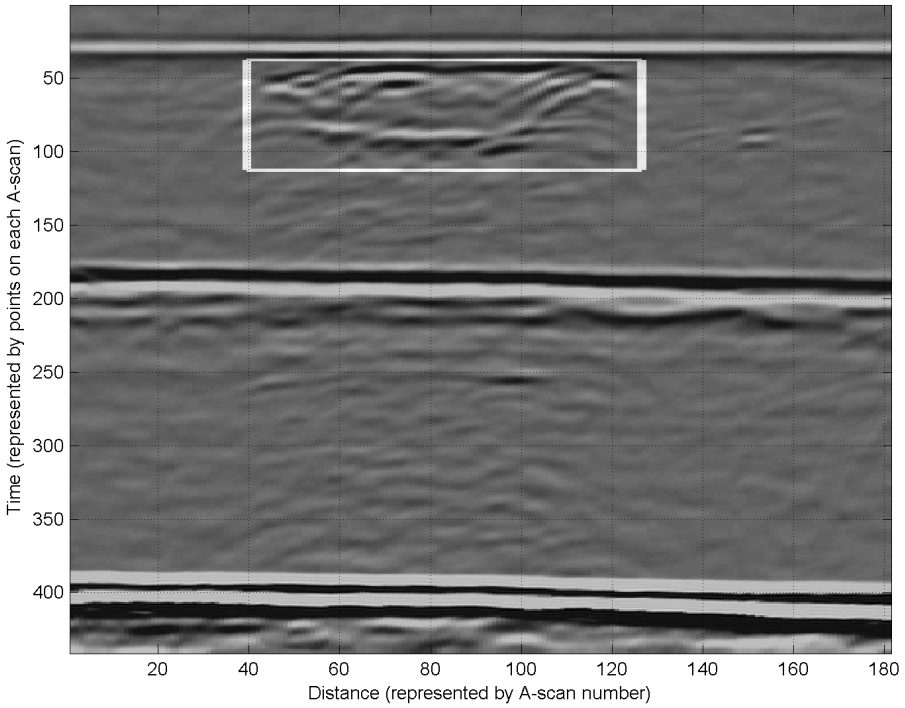

FIGURE 3.13: Automatically detected flaws in a D-scan image

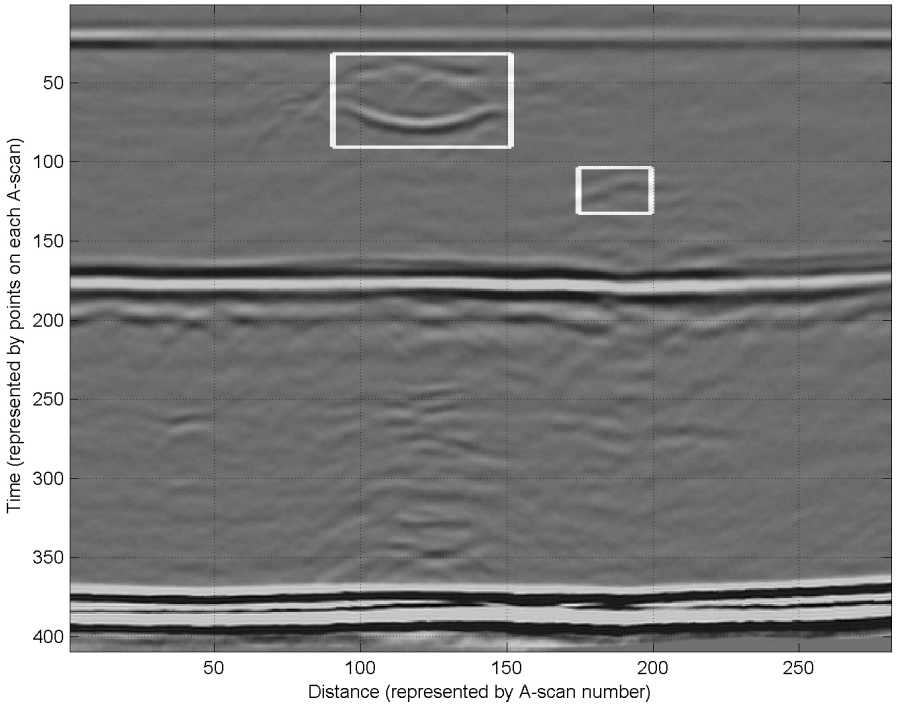

FIGURE 3.14: Automatically detected flaws in a D-scan image

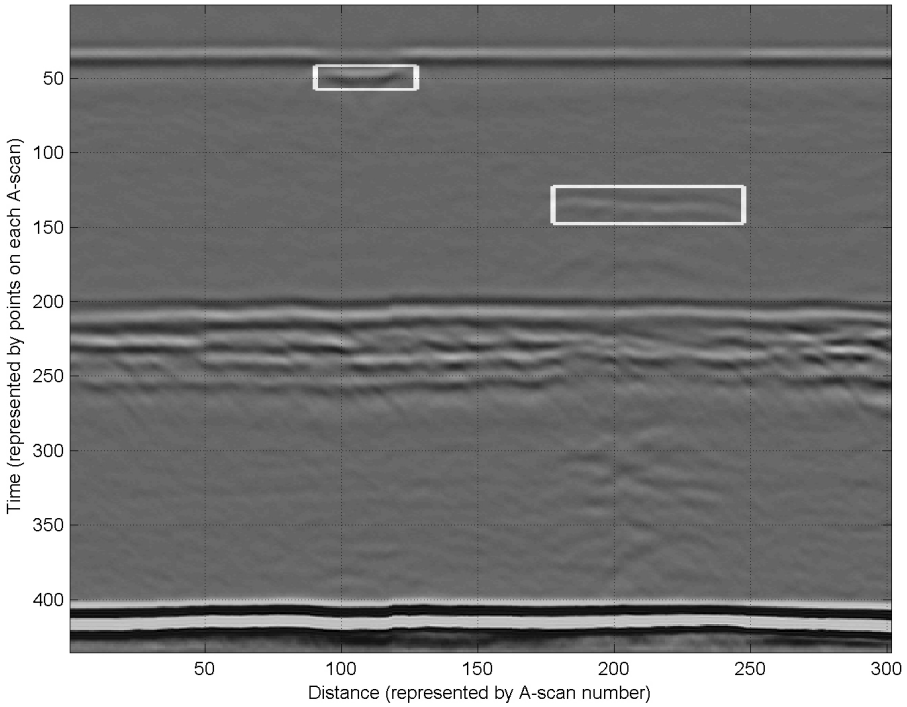

FIGURE 3.15: Automatically detected flaws in a D-scan image

3.4 Summary and conclusions

This chapter has proposed powerful methods for automatic pre-processing and flaw detection in TOFD D-scan data. Some of the used pre-processing methods have shown visual enhancement to the data, which is in favour of not only automatic interpretation but also manual interpretation by a human operator. On the other hand, some pre-processing methods aid only in automatic interpretation and there is no clear visual enhancement to the data. Data pre-processing helps in increasing the performance of the subsequent automatic interpretation stages and in reducing the rejection of TOFD scans due to poor quality, and hence, saving inspection time and cost.

Automatic flaw detection relies on image segmentation, and for that purpose two segmentation methods were discussed. Segmentation based on FCMI algorithm performs better in separating close defects when compared to variance thresholding method. It should be mentioned that the results of the automatic flaw detection are subject to operator verification and evaluation. Hence, it can be considered as a way to help the operator focusing on specific areas of interest in scan image to aid in making a final decisions regarding potential flaws.

Automatic flaw detection provides an important input to the subsequent stages, namely, flaw sizing and characterisation. The complete D-scan image data may not be needed, but rather, defect blobs will be processed further in subsequent stages.

Chapter 4

Automatic Flaw Sizing and Positioning

4.1 Introduction

Time-of-flight diffraction is one of the most common ultrasonic NDT techniques to size weld flaws in steel structures. It is based on measurement of the time-of-flight of the ultrasonic waves diffracted from tips of discontinuities originating from flaws. The resulting sizing accuracy is highly dependent on the skills and experience of human operators, which leads to inconsistencies and errors especially when the flaw is off-axis. The assumptions built into the acquisition software are inherently incorrect and lead by necessity to sizing errors. This chapter aims at proposing methods and algorithms to obtain automatic flaw sizing and positioning information based on the compression waves region to help in obtaining accurate interpretation of data. Eventually, these algorithms help in reducing the overall interpretation time and minimising sizing and positioning error.

4.2 Importance of flaw sizing and positioning

Most industrial welds are subjected to periodic ultrasonic inspection for the presence and size of weld defects. Flaws can be enlarged dramatically by fatigue and cause a reduction of strength. Monitoring the size of flaws is, hence, essential because if these flaws exceed a certain critical size, rapid brittle fracture will result, depending on the through-wall extent and orientation of the crack, and a catastrophic failure of structures may occur. Accordingly, accurate measurement of the through-wall extent of the flaws has great importance in ensuring the structural integrity of structures that helps in decommissioning decision-making process.

Conventional ultrasonic NDT techniques, such as PE, are used to detect and size these flaws pre-service and in-service. They rely on the reflected echo amplitude to get flaw sizing information and the signal travel time to locate flaw position and orientation [1]. These methods are based on the assumption that echoes from planar features suitably angled travel back to the transducer. They are simple and inexpensive, but they suffer from poor resolution for crack sizing when the echo is severely attenuated. The amplitude of the reflected echo may be influenced by factors such as surface roughness, particles in the specimen, transparency and orientation of the flaw. By the use of these techniques, flaws could be detected but there was often little precision in flaw sizing, leading to some critical flaws being overlooked or diagnosed incorrectly. This may lead to a failure or unnecessary repair or replacement of welded components. To overcome these limitations, ultrasonic TOFD is used [5].

4.3 Flaw sizing: height, width and depth determination

Current sizing and positioning techniques utilise the information in the compression waves region to identify the height, width and depth of the potential defects in the TOFD scan image. The emphasis on accurate sizing of these defects has encouraged the development of many standards such as BS 7706 [3] and ASME XI [20]. They are commonly used to aid the inspectors in TOFD data sizing interpretation.

Flaw sizing and positioning in TOFD data are still performed off-line and manually by skilled operators. It is actually a time-consuming and painstaking process requiring high operator skill, alertness, consistency and experience, a situation that is prone to measurement errors.

To automatically size and locate flaws, positions of the lateral wave and backwall signals need to be automatically detected, and all defects between the two are similarly identified and outlined using their longitudinal wave signatures. Sizing of defects then proceeds using these regions of interest only [2].

The arrival times of the diffracted wavefronts carry information about the spatial relationship of crack tips and, hence, the height and depth of the flaw can be estimated through measuring the arrival time of these echoes accurately with reference to those of the lateral wave and the backwall echo without the need of any amplitude measurement. Positioning of the tip signals can then be used to derive information about the actual flaw depth and height.

Size of the flaw is determined by its width and height, and its position is determined by its depth and distance from the scanning start point. After the automatic flaw detection stage described in previous chapter, the image regions containing flaws have already been accurately outlined, and flaw dimensions and depth can therefore be determined from these regions.

4.3.1 Flaw height determination

The height is defined as the maximum difference between flaw extremities in the z-direction (through-wall). It is determined by the difference between the location of the top and bottom echoes of the flaw, or in other words, the vertical distance between top and bottom echoes taking into account the phase relationship between both echoes (explained previously).

For internal cracks, both upper- and lower-tip diffraction echoes appear in the returns and the height of the flaw is determined by the difference in depth between them. When the detected signature consists solely of an apparent upper-tip diffraction without any associated indications in neither the lateral wave or the backwall echo, the embedded flaw is deemed to have no height. For top surface-breaking flaws, the flaw signature consists only of the lower-tip diffraction echo. Therefore, the height is determined by the distance between the lateral wave and this lower-tip diffraction signal. Similarly, in the case of bottom surface-breaking flaws, the height is determined by the difference in depth between the upper-tip diffraction and the backwall echo [3].

The signatures of the top and bottom echoes of flaws are usually inflated and suffer from profile variations. Accurate sizing of any flaw needs accurate tracing of the

profile of flaw top and bottom envelopes. This can be achieved by successive sub-sampling and cross-correlation to estimate the shift between adjacent A-scans [2, 5]. This shift is used to trace the profiles of the top and bottom envelopes within the flaw region taking into consideration the relative phases of the two wavelets as shown in Figures 4.1.

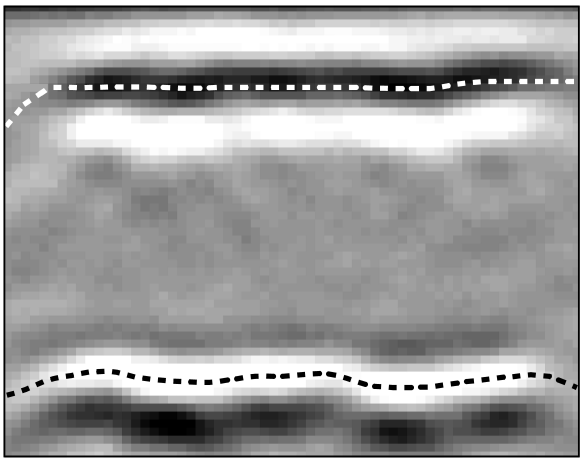

FIGURE 4.1: Flaw A-scan wavelets and profile detection

The time-of-flight of the flaw top and bottom echoes are measured in order to obtain the most accurate sizing results. In order to achieve this, the major wavelet peak (or trough) is detected, depending on the phase as shown in Figure 2.4. From the obtained flaw top and bottom tips profiles, the minimum and maximum distance (height) between these tip echoes can be extracted automatically. Hence, the maximum range of the flaw can be estimated by finding the difference between the maximum and minimum of tips heights.

4.3.2 Flaw width determination

The width is defined as the difference between flaw extremities in the x-direction (lateral). When TOFD probes scan across a defect, there is a direct relationship

between the width of the flaw record (returns) and its actual width. Therefore, the width of the flaw can be estimated directly from the width of its record in the D-scan data file. However, this record is usually elongated due to the finite width of the ultrasonic beam [5]. For flaws with a profile approximately parallel to the metal surface, there will be hyperbolic arcs (or wings) at the ends of the flaw record generated when the probes approach and leave the flaw. This elongation reduces the accuracy of the width estimation to about ± 5 mm, which is approximately the same as that given by pulse-echo techniques [85].

This elongation must be treated to improve the overall sizing accuracy of TOFD [2]. An improved method is proposed to treat the elongation by automatically detecting and fitting a curve to the arcs of the defect record in order to estimate their start points and then eliminate their effect on width estimation. As a result, the defect width can be accurately estimated without the error introduced by the added width of the wings. This would greatly reduce the effect of the elongation on the width estimation. This method is explained in Section 4.6.2.

4.3.3 Flaw depth determination

Flaw depth is defined as the distance between the scanning surface and the flaw top extremity in the z-direction. It is, in practice, directly related to the time-of-flight between the lateral wave and the echo from the flaw's top tip, taking into account the phase relationship between the two signals.

After the process of scan alignment (explained in Chapter 3), the lateral wave becomes level, while the top tip echo of the flaw may still suffer from profile variations. It can be estimated accurately in a similar way as shown in Figure 4.1.

By using the estimated lateral wave position (time) and the profile of the top tip echo of the flaw, the depth of the flaw can be estimated. A minimum and a maximum depth can be estimated based on the profile variation of the top tip echo.

As mentioned earlier in Chapter 2, there is a phase difference of approximately $3\pi/4$ between the echoes diffracted from the flaw top and the lateral wave. Correct exploitation of this phase information adds accuracy to the subsequent depth rescaling and allows accurate determination of the exact positions in time for the upper extremity as well as the relative times between this extremity and the lateral wave.

4.4 TOFD sizing limitations and errors

Despite all its good features, TOFD suffers from some limitations and errors. As far as sizing is concerned, the following are the major TOFD limitations and error sources:

a) TOFD suffers from a noticeable sizing error of off-axis flaws with D-scans due to the assumed lateral position of an indication by the acquisition software.

b) Sizing of surface-breaking and near-surface cracks is always a weakness in any TOFD inspection system, resulting in a very low accuracy of sizing measurement. This applies to both top and bottom surfaces.

c) Errors due to inaccurate PCS reading.

d) Timing errors.

e) Scanning errors.

The first two limitations are the most influential and difficult to handle in TOFD sizing and positioning interpretation, while the rest can be addressed easily and made minimum by different means.

This section shows how to quantify errors and determine their extent of these errors for different cases and configurations. All the discussions shown here are in terms of the compression waves region and, hence, all velocities and times refer to longitudinal waves.

4.4.1 Off-axis depth error

In D-scan configuration, the flaw is likely to be offset from the centre line of the axis between the transmitter and receiver probes in TOFD equipment. However accurate the time-of-flight may be, the lateral position of the source of the echo is still unknown. This gives rise to depth errors as the flaw is incorrectly assumed to lie equidistant from both probes [2, 5, 61]. Consider the situation for D-scan with a defect tip at depth d_x offset from the axis between the two probes by a distance X mm, and a transit time (neglecting probe time delay) of t μs (Figure 4.2). The range for a signal from the defect tip is given by:

$$v_L t = \sqrt{(s+X)^2 + d_x^2} + \sqrt{(s-X)^2 + d_x^2} \tag{4.1}$$

where v_L is the longitudinal wave velocity in the material.

The shape of the path with constant range (i.e. time) is an ellipse with the index points of the two probes at its foci, which can be written as such [2, 4, 5]:

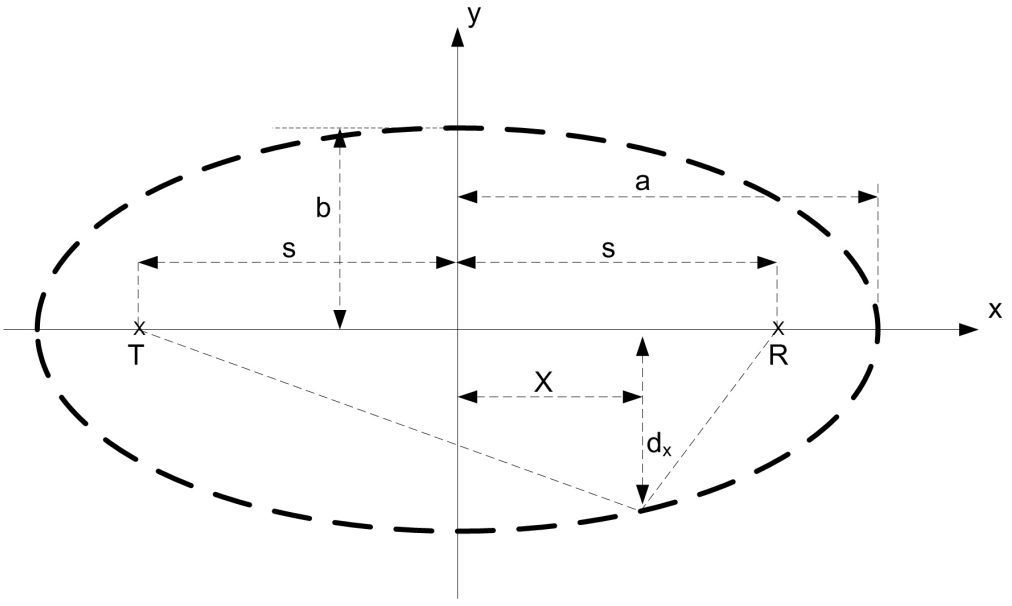

FIGURE 4.2: Ellipse with constant time-of-flight

$$\frac{x^2}{(v_L t/2)^2} + \frac{d^2}{(v_L t/2)^2 - s^2} = 1 \tag{4.2}$$

Rearranging this equation:

$$d^2 = \left(1 - \frac{x^2}{(v_L t/2)^2}\right)\left(\left(\frac{v_L t}{2}\right)^2 - s^2\right) \tag{4.3}$$

and if the depth is d_x for an offset X then:

$$d_x^2 = \left(\frac{1}{4} - \frac{X^2}{(v_L t)^2}\right)\left((v_L t)^2 - 4s^2\right) \tag{4.4}$$

The above expression represents an ellipse with the beam entry points as foci and path length $v_L t$.

In order to estimate the depth error for an off-axis crack tip, the maximum and minimum depth at which it could occur (i.e. d_{max} and d_{min}) need to be considered for a measured transit time (Figure 4.3).

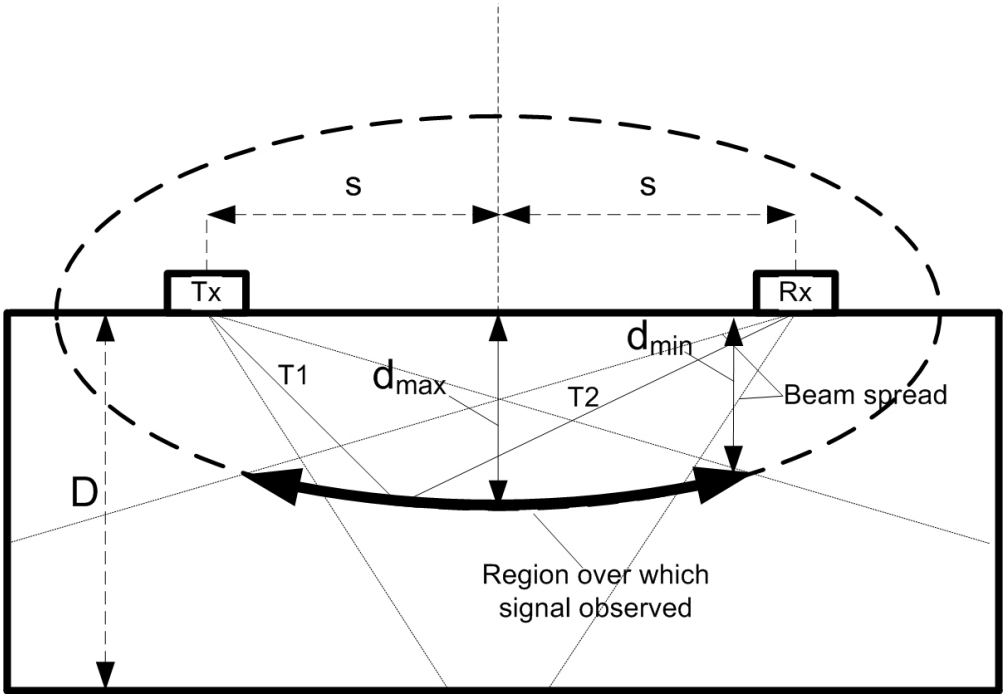

FIGURE 4.3: Uncertainty in lateral position in a D-scan

The maximum depth, d_{max}, is at the deepest point of the ellipse, i.e. when X=0, giving [5]:

$$d_{max} = \sqrt{\left(\frac{v_L t}{2}\right)^2 - s^2} \tag{4.5}$$

According to the equation of the ellipse representing the path for transit distance $v_L t$, the minimum value for the depth, d_{min} is when the flaw is at the edge of the inspection coverage area, X is less than $v_L t/2$, i.e. a fraction f (where $f < \frac{1}{2}$). Thus, the ellipse position for d_{min} is when $X = f v_L t$, hence [4]:

$$d_{min} = \sqrt{(v_L^2 t^2 - 4s^2)(\frac{1}{4} - f^2)} \tag{4.6}$$

Depth error can be expressed as a percentage of the minimum depth and is given by:

$$d_{error} = \frac{d_{max} - d_{min}}{d_{min}} \tag{4.7}$$

This is because the percentage error involves dividing by the true value, which is in this case would be d_{min} because d_{max} is clearly the wrong value caused by incorrect assumption.

Using Equations (4.6) and (4.5) in Equation (4.9), then:

$$d_{error} = \frac{\sqrt{(\frac{v_L t}{2})^2 - s^2} - \sqrt{(v_L^2 t^2 - 4s^2)(\frac{1}{4} - f^2)}}{\sqrt{(v_L^2 t^2 - 4s^2)(\frac{1}{4} - f^2)}} \tag{4.8}$$

which simplifies to:

$$d_{error} = \frac{1}{\sqrt{1 - 4f^2}} - 1 \tag{4.9}$$

4.4.2 Variation of the depth error with off-axis distance

In practice, the lower edge of the acoustic beam determines the maximum detectable lateral position of a defect tip. The variation of the factor f with the offset distance X is quite complicated and the maximum value (at the edge of the beam) depends on the probe separation and the probe parameters [2, 4].

Take the typical situation of aiming the beam centres at $2D/3$, where D is the material thickness. Then, for an ellipse with depth d=$D/2$ (when the offset X

is zero), the variation of the factor f with offset (expressed as a fraction of X to s) is shown in Figure 4.4, and the corresponding percentage depth error in Figure 4.5. At the extreme position $X = s$ (i.e. defect is directly beneath one of the probes), $f = 0.46$ and the depth error is 155%. Thus, the depth error for an off-axis reflector can be very large.

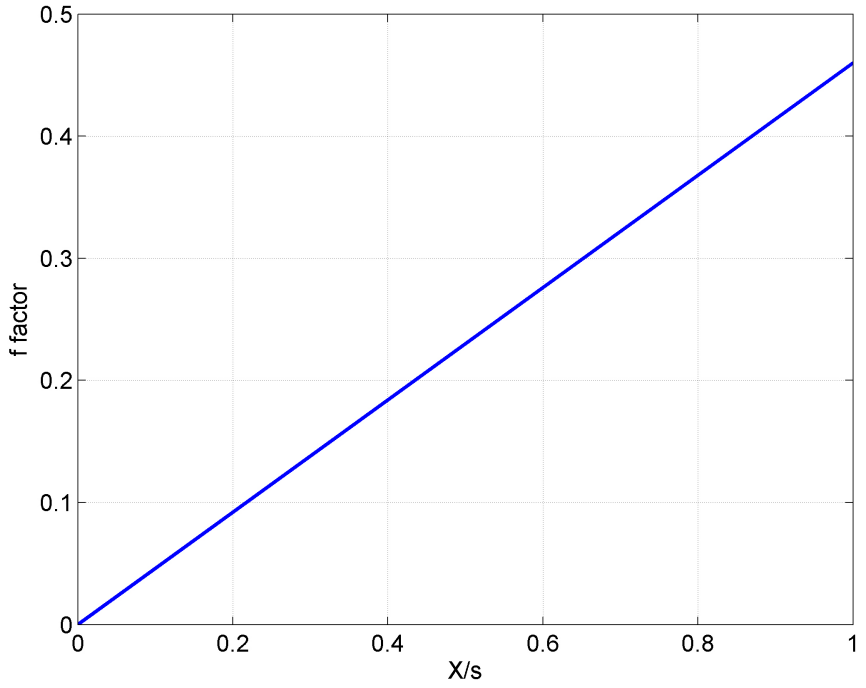

FIGURE 4.4: Variation of the factor f with off-axis distance X at $d = D/2$ and $s = 2D/3 \tan\theta$

Consider two situations, the first considers the depth error at the edge of the ultrasonic beam and the second the error at the edge of a typical weld.

Depth error at edge of ultrasonic beam Consider the general case where the flaw tip is at the edge of the beam. Let s be related to the thickness of the sample, i.e. $s = uD$, and the path length when $X = 0$ at a depth d is thus given

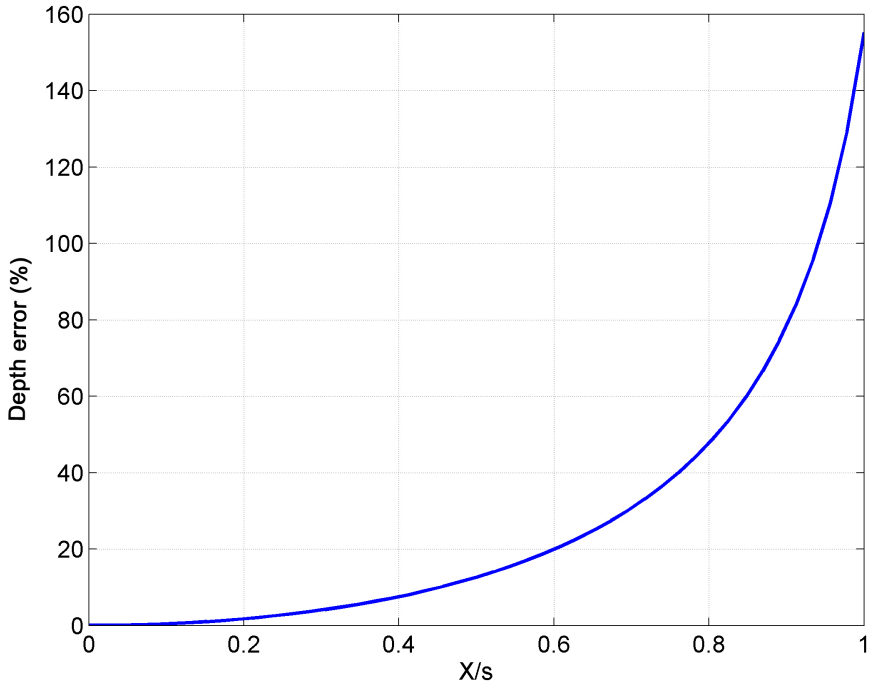

FIGURE 4.5: Variation of depth error with off-axis distance X at $d = D/2$ and $s = 2D/3 \tan\theta$

by:

$$v_L t = 2\sqrt{d^2 + s^2} = 2D^2\sqrt{v^2 + u^2} \tag{4.10}$$

where d is related to the thickness of sample by $d = vD$.

The edge of the beam at depth d is given by:

$$X = s - d \ \tan\varphi = D(u - v \ \tan\varphi) \tag{4.11}$$

where φ is the angle of the lower edge of the beam from the upper surface. It is assumed that any indications are in the far-field of the probes and that the ultrasonic beam can be described by a divergent beam emerging from the probe

index points. Hence:

$$f = \frac{X}{v_L t} = \frac{D(u - v\ \tan\varphi)}{2D\sqrt{v^2 + u^2}} = \frac{(u - v\ \tan\varphi)}{2\sqrt{v^2 + u^2}} \tag{4.12}$$

Let us consider two situations, the first with beam centres aimed at $2D/3$ and secondly with the beam centres aimed at the backwall. This can be done by adjusting the PCS. The general equation of the PCS was shown previously in Chapter 2 to be:

$$PCS = 2\ D_f\ \tan\theta \tag{4.13}$$

where D_f is the focus depth and θ is the beam centre angle. Based on the above equation and the fact that PCS=$2s$, it is always acceptable to take s=D_f tanθ. For the most typical cases of a 60° probe, with 5 MHz and 6 mm crystal diameter, the lower beam angle, φ, is about 45° for a beam edge cut-off of 10 dB. Taking the first case when beam centres aimed at 2/3 of sample thickness, $s = 2D/3\ \tan(60°)$, and at a depth of half of the sample thickness, the quantities derived in this section are u=2 tan(60°)/3=1.15 and v=0.5.

Similarly, at $d = D$, v=1. The corresponding values for the factor f and the depth error are shown in Table 4.1.

TABLE 4.1: Depth errors at edge of beam aimed at $2D/3$

Depth	f	**Depth error (%) at beam edge**
$D/2$	0.26	17.1
$2D/3$	0.18	7.5
D	0.05	0.5

The variation of the depth error as a function of the depth is shown in Figures 4.6.

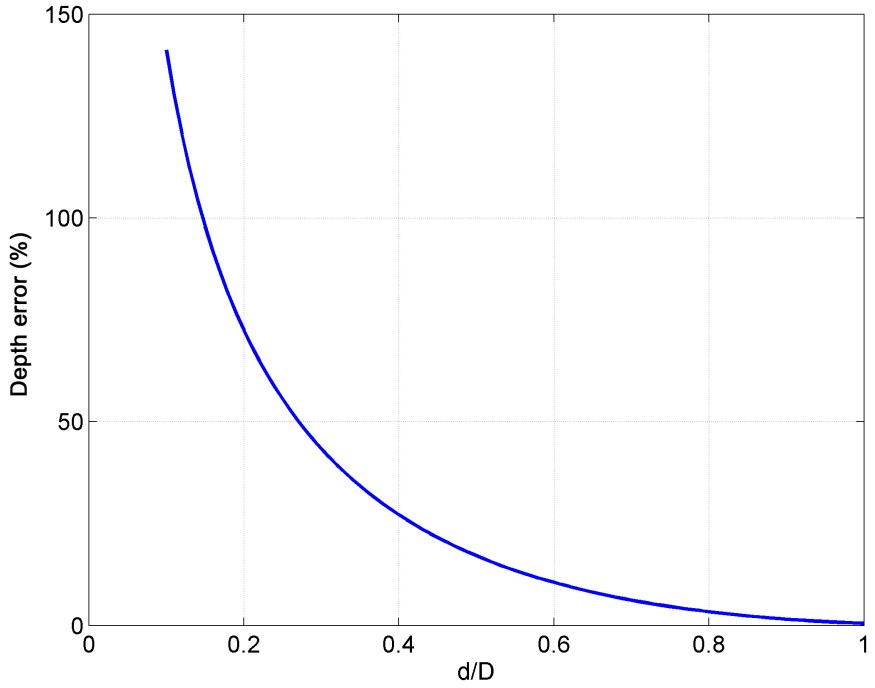

FIGURE 4.6: Depth error at edge of the beam for $s = 2D/3 \tan\theta$

It can be seen from the figures that the depth error (and f) decreases with increasing depth. Near the upper surface, however, the maximum depth error at the beam edge is very large, but at the 2/3 depth it is typically 7.5%.

For the second case, with the beam centres aimed at the backwall, $s{=}D \tan(60°)$ and hence, $u{=}\tan(60°){=}1.73$ and at the backwall $v{=}1$. The corresponding values for the factor f and the depth error are shown in Table 4.2.

TABLE 4.2: Depth errors at edge of beam aimed at backwall

Depth	f	**Depth error (%) at beam edge**
$D/2$	0.34	37.0
$2D/3$	0.29	22.1
D	0.18	7.5

The variation of the depth error as a function of depth is shown in Figure 4.7.

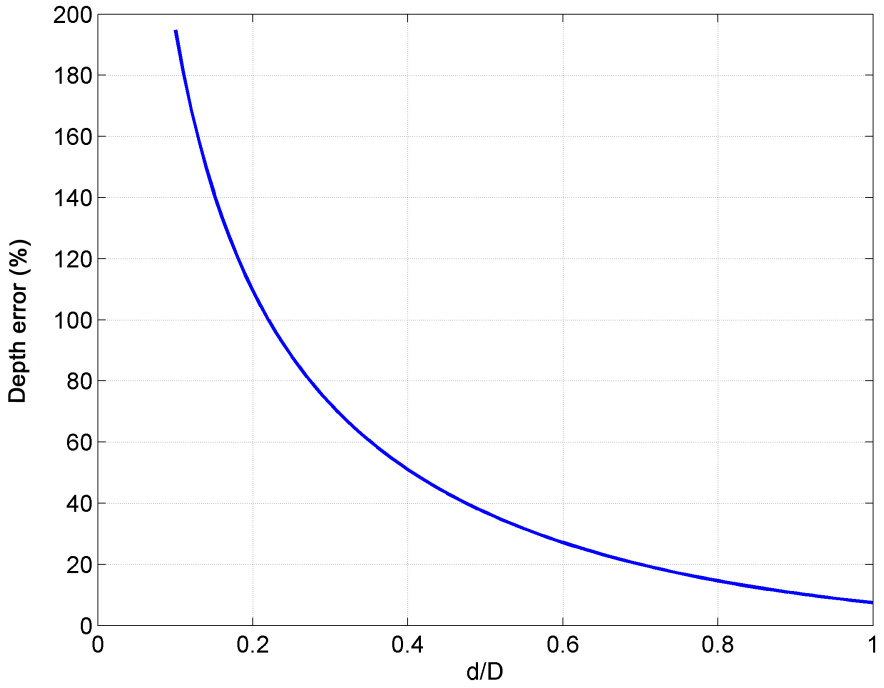

FIGURE 4.7: Depth error at edge of beam for $s = D \tan\theta$

As before, the depth error decreases with increasing depth, and the maximum error is large near the upper surface. At the backwall, the maximum depth error is 7.5%.

Depth error at edge of weld The more realistic maximum depth error occurs when the defect is at the edge of the weld, since most flaws are found in this part. Consider a typical situation for the case of a single V weld (Figure 4.8) inspected from the top surface. The x-axis offset at the edge of the weld at depth d below the surface is given by $X = (D - d)\tan(30°)$ for a total included weld angle of 60° and $s = 2D/3\tan(60°)$.

Figures 4.9 and 4.10 plot the factor f and the corresponding depth error as a function of depth into such a sample.

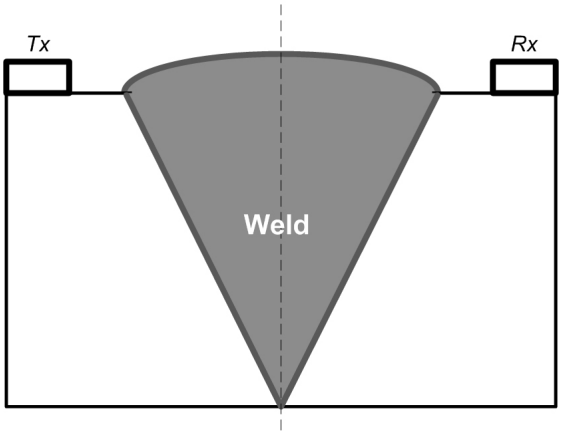

FIGURE 4.8: A single V Weld

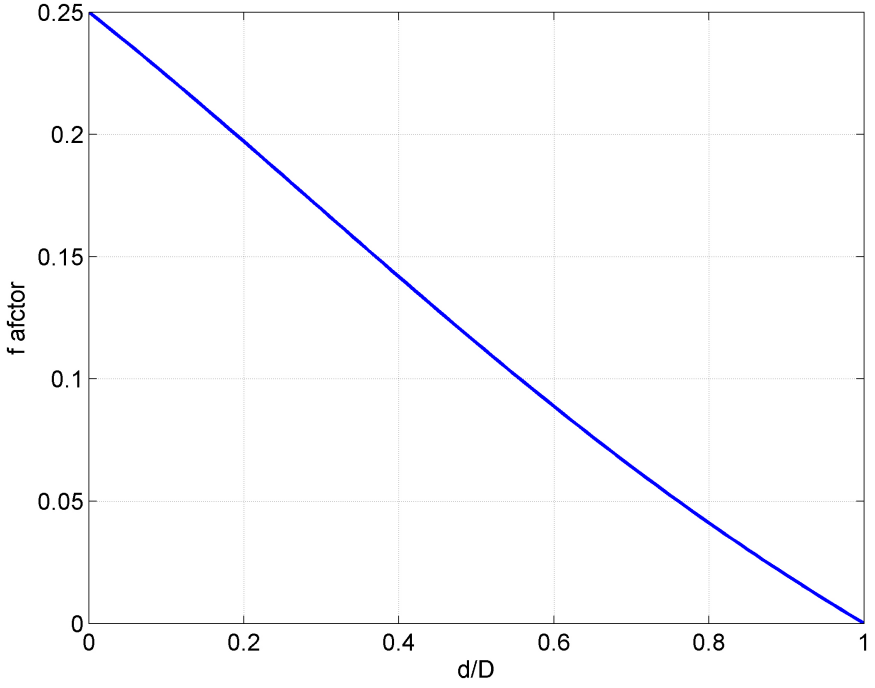

FIGURE 4.9: Variation of factor f at edge of a single V weld (included angle 60°) for $s = 2D/3 \tan(60°)$

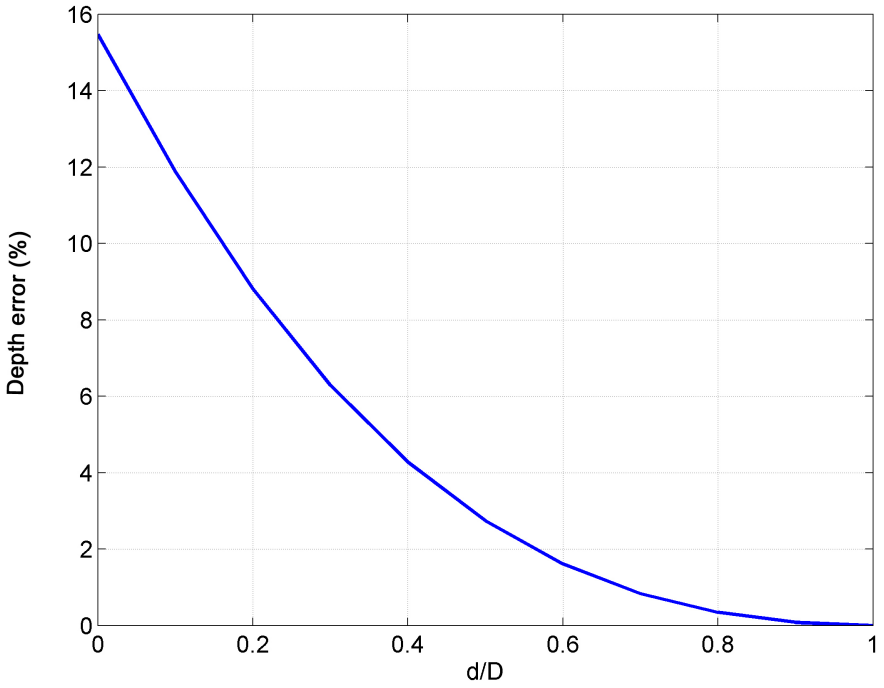

FIGURE 4.10: Depth error at edge of a single V weld (included angle 60°) for $s = 2D/3 \tan(60°)$

Thus, the maximum error is on the edge of the weld near to the top surface and is 15.5%. The error at the edge of the weld rapidly decreases and in the bottom half of the weld the error is less that 3%, becoming zero at the root. For the case of double V weld (Figure 4.11), the depth error as a function of depth will be as shown in Figure 4.12.

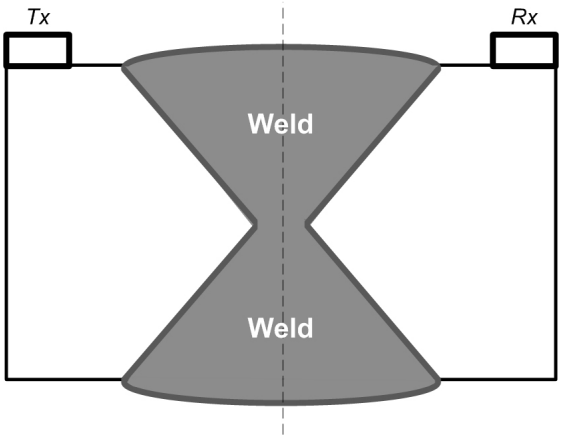

FIGURE 4.11: A double V Weld

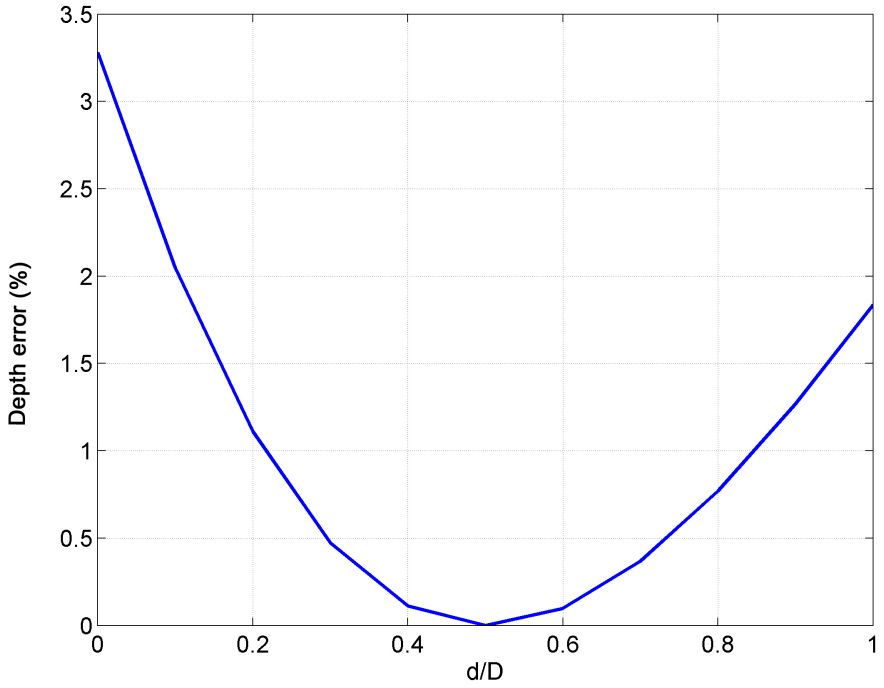

FIGURE 4.12: Depth error at edge of a double V weld (included angle 60°) for $s = 2D/3 \tan(60°)$

4.4.3 Summary of off-axis depth error

There is considerable variation in the maximum depth error with a D-scan TOFD. The depth error increases non-linearly from a minimum for indications on the centre line between the two probes to 155% or greater at s (half the PCS). Thus, in theory, large errors are possible for the measurement of depth for off-axis indications. The calculation of the error is complex and depends on the off-axis distance, the depth of the indication and the PCS. To put this into context, the situations where the indication may be at the edge of the ultrasonic beam or restricted to the edge of the weld are considered.

For the situation where the indication could be anywhere in the beam coverage of the TOFD probes, the maximum depth error occurs along the lower edge of the ultrasonic beam. For the general case where the beam centres are aimed at 2/3 the

sample thickness and 60° probe shoes, 6 mm diameter, and a frequency of 5 MHz are used, the maximum error at the beam edge (10 dB cut-off) will vary from greater than 155% at the near surface to 0.5% at the far surface. At the 2/3 the thickness, the factor f=0.18 and the error is 7.5%. When looking for weld root erosion in the heat effected zone, is a more specific situation. The probes are aimed at the backwall and it has been seen that at the edge of the beam on the backwall f=0.18 and the depth error is 7.5%. For a 20 dB cut-off of the beam edge, the value of f rises to 0.21 and the depth error to 10.2%. Thus, a typical value for f in this situation is 0.2, i.e. X=0.2$v_L t$ which gives a maximum depth error of 9%. Thus, for an off-axis flaw for a sample of thickness 25 mm, the maximum depth error on the backwall is 2.25 mm.

If it can be assumed that any likely flaws are restricted to the volume of the weld being inspected, then the maximum depth error is when the flaw is on the weld edge. Consider the situations for a single V weld (included angle 60°). Again it is assumed the 60° with 5 MHz and 6 mm diameter probes are aimed at 2/3 the thickness of the sample. The maximum depth error along the edge of the weld varies from 15.5% at the top surface to 0% at the lower surface. For the bottom half of the weld, the maximum error is less than 3%.

In summary, for D-scan, the measurement of the depth of a flaw is not as accurate as with B-scan technique. This leads, when depending only on the raw D-scans, to wrong interpretation decisions and unnecessary repairs, and hence, extra costs. In this project, novel methods will be proposed to increase the reliance on D-scans by increasing sizing accuracy to a level comparable with B-scans.

4.4.4 Surface-breaking and near-surface cracks problem

There are two main problems with defects that breaking or near to the inspection surface: the poor depth resolution due to timing uncertainty and the presence of the lateral wave that may mask the indication of crack tips. The lateral wave may ring for several cycles, typically up to two periods. The presence of the lateral wave is a serious problem and for probe arrays aimed at $2D/3$ for near-surface cracks. It extends to an equivalent depth of many millimeters depending mainly on the chosen value of the PCS. An indication of a possible signal can sometimes be seen in the lateral wave because of interference between the two signals and a change in the regular pattern. Also, signals from near-surface region can often be seen better after the backwall (as a shear wave signal in the mode-converted region) because of the lower velocity and the time scales are effectively increased.

Surface-breaking defects should be easily seen because they may interrupt the lateral wave and appear as a dip in this signal. Sometimes, however, the lateral wave may round the sides and the defect will not be detected (because of its size).

Similarly, the backwall signal may obscure a signal from a flaw. It can be shown that the dead zones due to the lateral wave DZ_{lw} and that due to the backwall DZ_{bw} can be expressed as:

$$DZ_{lw}\ (mm) = \sqrt{(v_L/2)^2(t_{lw} + t_{pl})^2 - s^2} \tag{4.14}$$

$$DZ_{bw}\ (mm) = \sqrt{(v_L/2)^2(t_{bw} + t_{pb})^2 - s^2} - D \tag{4.15}$$

where t_{lw} and t_{bw} are the times-of-flight of the lateral wave and the backwall signal,

respectively, and t_{pl} and t_{pb} are the durations of the lateral wave and backwall acoustic pulses in microseconds up to 10% of the maximum amplitude, respectively. For example, consider the inspection of 40 mm thick sample with 5 MHz probes and a PCS of 100 mm. Taking the pulse duration as two cycles for the lateral wave (i.e. $t_{pl} = 0.4$ μs) and four cycles for the backwall signal (i.e. $t_{pb} = 0.8$ μs), then the dead zones can be found to be $DZ_{lw} = 11$ mm and $DZ_{bw} = 3.7$ mm. The dead zones can be decreased by reducing the PCS or by using probes with shorter pulse lengths or higher frequency (further discussion on this will be shown in Section 4.5). Solutions to these problems will be suggested later in Chapter 6.

4.4.5 PCS reading uncertainty

In the current TOFD acquisition systems, the probe centre separation is measured manually by the operator using a ruler and then it is fed into the software. As the probes have finite diameters, the exact probe-centres can not be determined accurately. Accordingly, this measurement suffers from inconsistency and inaccuracy. As the depth estimation is directly dependent on the PCS (or s), any error in this measurement results in noticeable depth error. This error can be expressed as [3]:

$$\Delta d_s = \frac{\Delta s(\sqrt{d^2 + s^2} - s)}{d} \tag{4.16}$$

where Δd_s is the error resulting from an error Δs in the PCS.

To rectify this error, an estimate of the effective value of s can be used to correct the measured PCS value by calibrating the measurements on a signal with a known depth and making use of the specimen thickness and the lateral wave and backwall times, which are determined accurately in the pre-processing stage. Based on

the fact that the measured time between the lateral wave and backwall echo is equivalent to the thickness of the test plate D (which is known), the effective value of the PCS (or s) can be calculated by calibrating the maximum depth with the thickness of the test plate. The effective value of s in this case is found to be as follows:

$$s = \frac{D^2}{v_L t_{bw}} - \frac{v_L t_{bw}}{4} \tag{4.17}$$

where v_L is the longitudinal ultrasound propagation velocity in the test plate, and t_{bw} is the time of the backwall echo relative to that of the lateral wave. By estimating the effective value of s, the influence of PCS error can be overcome which reduces the depth error.

4.4.6 Timing uncertainty

Timing errors are mainly caused by either probe delay error, phase measurement error or a combination of both. They are often dominant contributors to the total error in depth estimation.

Probe delay is a very short time (5 to 7 μs) required for the ultrasonic signal to travel through the probe shoe and coupling layer. The effect of this is to increase the transit time of all signals. This increase needs a depth correction which is small enough to be ignored, unless very thick shoes or coupling layers are used. The delay is assumed to be the same for all paths, which is an acceptable approximation, and is treated as a constant. It should be subtracted before the estimation of the depth is made, and it can be determined from the time of the lateral wave signal

which can be calculated if the PCS is known:

$$t_{lw} = \frac{2s}{v_L} \tag{4.18}$$

To rectify this error, the reference for time measurements is taken as the peak of the main lobe of the lateral wave and is hence computed by subtracting t_{lw} from any time measurements:

$$t_r = t - t_{lw} = t - \frac{2s}{v_L} \tag{4.19}$$

Phase measurement error originates because of two reasons. The first reason is that the operator usually assumes that the signal from the bottom of the flaw is in-phase with the lateral wave and that from the top is in-phase with the backwall echo. While, as described earlier, the phase of the signal from the bottom of a flaw lags that of the lateral wave by $\pi/4$, and that from the top of the flaw leads by $3\pi/4$. Accordingly, an error of about $\pi/4$ will result. The second reason is that the operator determines the phase manually using a software cursor. This process involves human errors and leads to significant measurement error.

To rectify this error, a process of successive detection and tracking is used to determine the exact positions of peaks and troughs in time for each scan taking into consideration the relative phase relationship between the two wavelets as described earlier. Accordingly, the $\pi/4$ phase error can be rectified automatically in depth calculation by subtracting the time equivalent to it from the time of the top tip echo of a flaw.

4.4.7 Scanning errors

Ultrasonic signals generated from TOFD probes need a thin layer of coupling material, usually gel or fluid, in order to be transmitted to the component under test, because of the fact that ultrasonic energy can not be transmitted in air. The thickness of the coupling layer is so thin that its influence on the time-of-flight of signals can be ignored when compared to other sources of error. However, the effect of this layer may be taken in to considerations when the scanned surface has irregularities (because a thicker coupling layer is necessary in this case). An additional signal delay results in this case, and a certain measurement error occurs.

To rectify this error, a similar solution to the probe delay problem can be followed by considering that any delay resulting from the couplant layer to be a part of probe delay and then its influence is eliminated by measuring the time of any flaw signal with reference to the time-of-flight of the lateral wave t_{lw}.

4.5 TOFD sizing resolution

Resolution is defined as the minimum separation of two signals before they can be correctly identified, e.g. the top and bottom tip diffraction signals from a small crack. Resolution, therefore, sets a lower limit to the size of flaw for which top and bottom echoes can be detected. In general, because the signal wavetrain contains several cycles corresponding to typically 2 or 3 wavelengths, this is the resolution distance. For 5 MHz probes, this will correspond to 2 to 3 mm [4]. Hence, the top and bottom echoes from smaller flaws such as slag lines or pores are not usually

resolved. The following steps show how to get the theoretical formula for the resolution in terms of the relevant parameters of a TOFD system.

The maximum timing error (E_s) due to sampling is related inversely to the sampling frequency f_s, hence:

$$E_s = \frac{1}{2f_s} \tag{4.20}$$

Thus, for a probe frequency of 5 MHz and f_s taken as 25 MHz, E_s will be 0.02 μs.

Based on the time-of-flight relationship (and with reference to Figure 4.13), the resolution ρ can be defined as follows:

$$\rho = v_L \sqrt{(\frac{t_{lw} + E_s}{2})^2 - (\frac{t_{lw}}{2})^2} \tag{4.21}$$

where t_{lw} is the time taken by the lateral wave to travel directly from the transmitter to the receiver, and v_L is the longitudinal wave velocity in the material. Now, t_{lw} is expressed as:

$$t_{lw} = \frac{PCS}{v_L} = \frac{2s}{v_L} \tag{4.22}$$

Substituting Equations (4.20) and (4.22) in Equation (4.21) and simplifying, yields:

$$\rho = v_L \sqrt{\frac{1}{4f_s}(\frac{PCS}{v_L} + \frac{1}{4f_s})} \tag{4.23}$$

which can be approximated for large values of f_s to:

$$\rho \approx \frac{1}{2}\sqrt{v_L \frac{PCS}{f_s}} \approx \sqrt{\frac{v_L s}{2 f_s}} \tag{4.24}$$

For example, consider a case where the PCS=58 mm, v_L=5.69 mm/μs, f_p=5 MHz and f_s=25 MHz. This leads to a resolution of ρ≈1.8 mm. If the sampling frequency increases to 100 MHz, then this gives a resolution of ρ≈0.9 mm (enhancement by 50 % compared to the former case).

Equation (4.24) shows an important result regarding the relationship between resolution in TOFD and the probe separation and the sampling frequency. Reducing the PCS (or increasing the sampling frequency) by a factor of 4 results in a two-fold enhancement in the resolution.

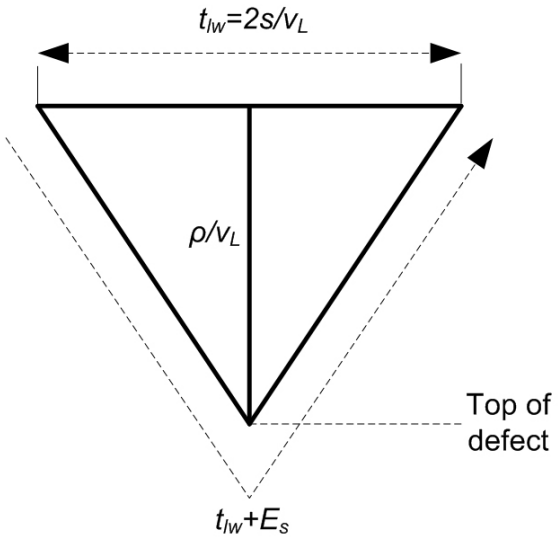

FIGURE 4.13: TOFD resolution illustration

4.6 Accurate determination of size and depth of off-axis flaws

This section presents a method for accurate determination of the size and depth of off-axis flaws in D-scans using diffraction arcs curve fitting technique. The proposed method can be explained as follows:

4.6.1 Through-wall size and depth of cracks

As mentioned earlier, in D-scan configuration, the flaw is likely to be offset from the centre of the axis between the transmitter and receiver by a distance X as shown in Figure 4.14. From the acquisition geometry, the path of the ultrasonic signal from the transmitter to the receiver can be expressed by (without taking into consideration the transducers' longitudinal movement) [2, 5, 61]:

$$v_L t = \sqrt{(s+X)^2 + d^2} + \sqrt{(s-X)^2 + d^2} \tag{4.25}$$

where all the parameters have their ordinary definition.

This path $v_L t$ has the same value for any point on an ellipse with foci at the transmitter and receiver centres. The travel time therefore can not yield a unique value for depth as the position of the defect tip on the ellipse is impossible to determine and there will always be some depth error, as can be seen by rearranging Equation (4.25):

$$d = \sqrt{(\frac{1}{4} - \frac{X^2}{v_L^2 t^2})(v_L^2 t^2 - 4s^2)} \tag{4.26}$$

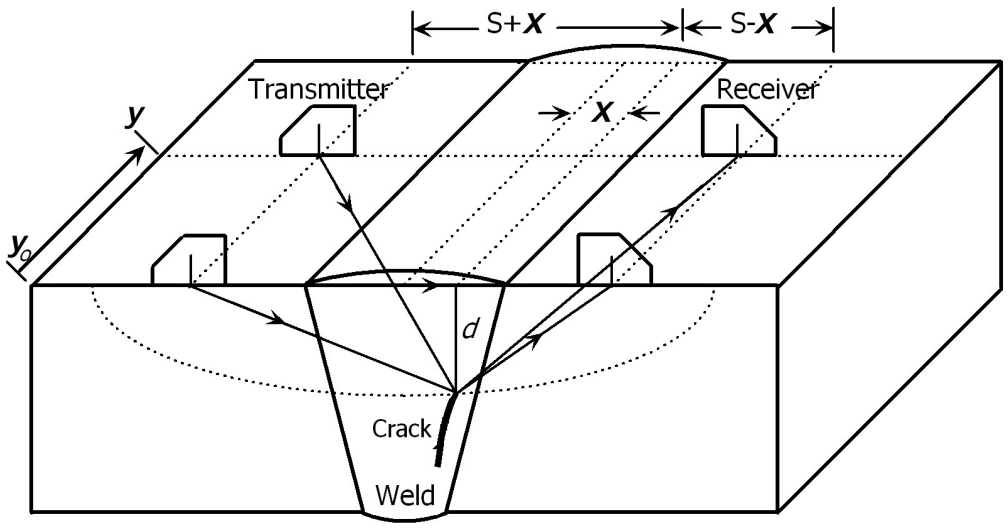

FIGURE 4.14: Effect of lateral flaw position on the arrival time in D-Scan

From the above equation, it is clear that if X is unknown then d can not be calculated. To overcome this problem, it is normal practice to perform a TOFD B-scan at the position of a detected defect to measure the depth accurately and find the offset X. Measurement errors are minimised because (as mentioned earlier) at some point within the B-scan the defect must lie equidistantly between the two probes. This operation requires that the operator first analyses the D-scan to find the locations of any potential flaws, and then carries out a number of supplementary B-scans to measure their depths. It is clear that this introduces a certain amount of subjectivity to the operation and adds to the total inspection time. By assuming, as current processing and reporting software invariably does, that the diffracted returns originate from a point mid-way between the transducers (i.e. $X = 0$) the interpreted depth suffers from an error. This error (Δd_X) due to the error in lateral position can be calculated by [2, 61]:

$$\Delta d_X = \frac{2X^2}{v_L t}\sqrt{\frac{v_L^2 t^2 - 4s^2}{v_L^2 t^2 - 4X^2}} \tag{4.27}$$

Even though flaw sizing using TOFD in D-scanning mode is more accurate than

other (conventional) ultrasonic techniques, this depth error can still be significant, as shown previously in Section 4.4.

When the flaw is located in the plane normal to the inspection surface and passing through both transmitter and receiver, the transit time of the pulse is at a minimum. As the transducers move away from this position, as illustrated in Figure 4.14, along a scan line perpendicular to the plane of the flaw, the transit time increases resulting in ***arcs*** or ***wings*** at the ends of the flaw record in D-scan presentation.

For a flaw located at a position y_o (in Figure 4.14) along the weld, the shortest path of a diffracted signal when the transmitter and receiver are moved to position y can be shown to be [2, 5, 61]:

$$v_L t = \sqrt{(s+X)^2 + d^2 + (y-y_o)^2} + \sqrt{(s-X)^2 + d^2 + (y-y_o)^2} \qquad (4.28)$$

This equation represents the dependence of end of defect signature shape on the off-axis distance (X) as shown in Figure 4.15. The depth error is directly related to X (follows from Equation (4.27)). Figure 4.16 shows a 3-D representation for the compound effect of this dependency.

4.6.2 Diffraction arcs and curve fitting

The way in which the time-of-flight of a flaw varies with probe position during a scan leads to characteristic arcs appearing in the data record. These arcs (or wings) can be used as a tool to give more accurate sizing capability [5, 61]. When a flaw tip lies in the vertical plane defined by the probe beam centre lines and

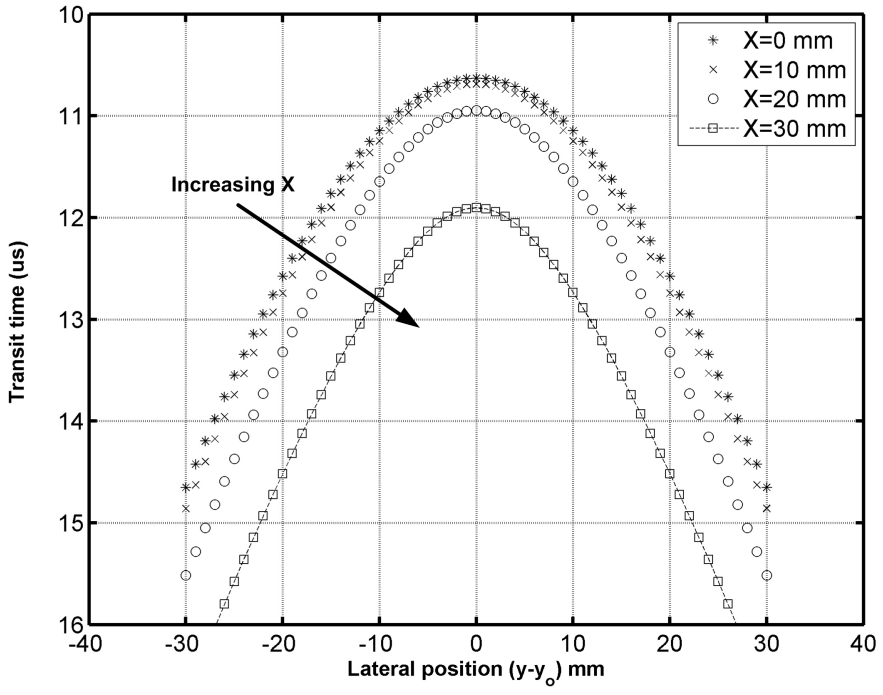

FIGURE 4.15: Dependence of defect signature shape on lateral position and off-axis distance (s=30 mm, d=10 mm)

is equidistant from the two probes, the transit time is a minimum. If the probes are moved in any direction, the signal will still be present because the tip still lies within the beams but the distance will have increased and the indication will therefore appear a little later on the data record. A continuous scan across the location of the flaw will produce an indication having characteristic downward-curving tails as was shown in Figures 4.15 and 4.16.

Equation (4.28) is recognised as an equation of a hyperbola for variables t and y. This has two implications; physically, t is at a minimum at the point where the scattering point lies in the plane defined by the two beam axes and it increases as the point moves away from that plane. On the other hand, it is clear that signal loci, although hyperbolic only in the special case referred to above, is of the same general shape for all scan paths in this simple geometry. In particular, the signal loci for a scan parallel to the plane defined by the beam axes will look very much

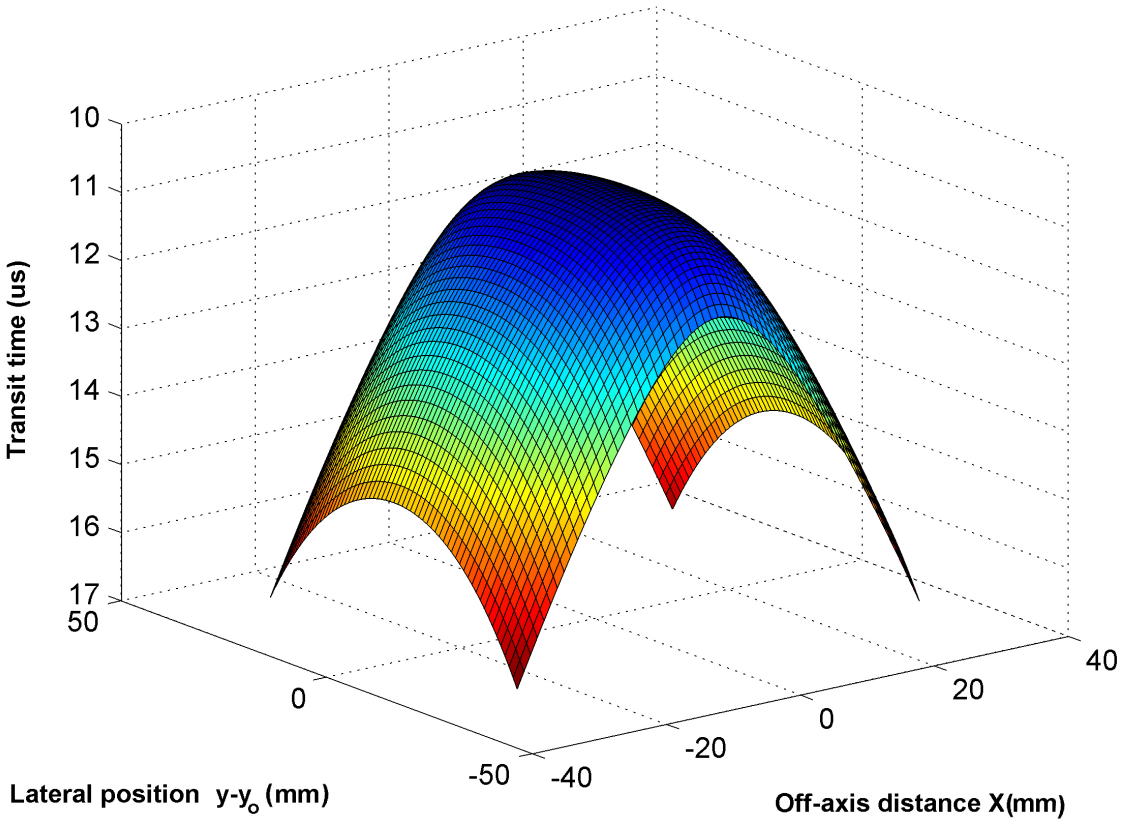

FIGURE 4.16: 3-D Representation of defect signature dependence on lateral position and off-axis distance (s=30 mm, d=10 mm)

like hyperbolas for deep defects but will appear increasingly flattened as the defect is approached.

Since the shape of the arcs depends only on the defect depth, the defect lateral displacement, probe separation and direction of probe motion, it is predetermined for any given depth [2, 5]. It is a simple matter to provide a means of displaying the correct shape as a cursor on a digital display and to allow it to be moved interactively to check its fit to any suspected defect indication. It is also highly desirable to automate the characterisation of these arcs in order to determine the offset X, and hence the depth d can be found more accurately.

For each detected defect, the edge points of the defect signature can be determined

by a combination of 2-dimensional alignment processing and 1-dimensional peak tracing for each echo. As a result, the sets of points representing the envelope of the defect echo wavefront can be detected. These points can be checked if they represent arcs by identifying those with a monotonic increase in time. The points can then be modeled to fit, in a minimum mean square error sense, a curve governed by Equation (4.29) (following from Equation (4.28)) with varying X from 0 to s and varying d from d_{min} to d_{max} possible values:

$$t = \frac{1}{v_L}(\sqrt{(s+X)^2 + d^2 + (y-y_o)^2} + \sqrt{(s-X)^2 + d^2 + (y-y_o)^2}) \qquad (4.29)$$

As a result of this curve fitting, not only can X be found, but the start point of the arc can be identified more accurately. This point is then used to correct the measured width of the defect (by finding the distance between the start points of the two wings defining the flaw) to eliminate the effect of elongation in the flaw record due to the finite width of the ultrasonic beam, while the estimated value of X is then used to correct the lateral position of the defect (Equation (4.26) or (4.27)) and, hence, minimise the depth error which increases the accuracy of the sizing measurements.

To test the effect of the offset X on the shape of the arcs, different flaws in D-scan data files with different values of offsets were examined. These scans were generated by placing the probes with unsymmetrical distances from the centre plane of the weld (off-axis scanning) with considering the position of the defect from the centre plane of the weld. The actual offset values used in data acquisition are then compared with the estimated values from curve fitting, and the result is that they are identical. In data acquisition, changing X is limited by the width of the weld cap of each plate and the position of the weld from the centre plane of the

weld. Some examples of the effect of changing the offset X on the arcs shape are shown in Figure 4.17. This method presents a very important result: it is possible to measure the transverse position of a defect when performing an ultrasonic D-scan by studying how the arcs of a defect indication vary with scan position. This information would normally be obtained only from a B-scan image. It should be mentioned that there is one limitation to this method: it does not indicate whether the defect is off-axis to the right or to the left of the weld (direction of the displacement). In other words, the value of X is determined accurately, but it is not obvious whether this off-axis shift is to the left or to the right of the centre line of the weld. A novel solution to this limitation will be discussed later in Chapter 6.

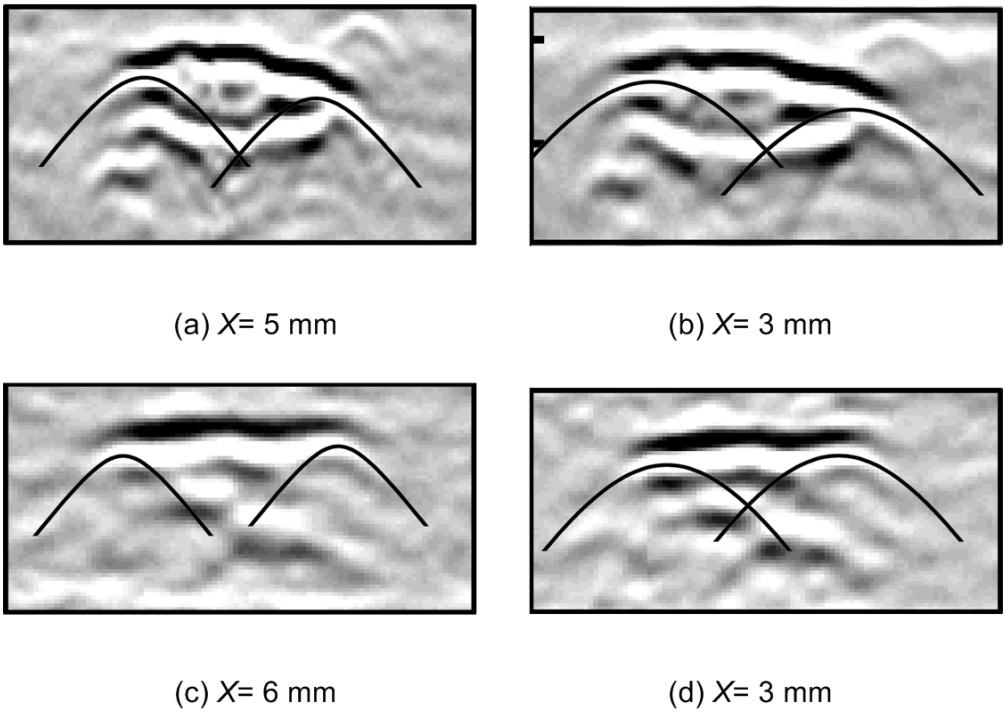

FIGURE 4.17: Application of curve fitting to estimate X (Actual and estimated values are identical)

4.7 Summary and conclusions

This chapter has introduced flaw sizing and positioning in TOFD D-scans and the extent of the incorporated limitations and errors. A number of techniques have been developed to process the information provided in the compression waves region to size and locate flaws automatically, and, hence, relieving the operator from error-prone, mundane and routine tasks. A curve fitting method was used to measure the transverse position of an off-axis flaw accurately when performing a D-scan by studying how the arcs of a defect indication vary with scan position, an information that would normally be obtained only from a B-scan image. However, some limitations still exist in sizing of off-axis and near-surface flaws (which are among the weaknesses of TOFD), and in Chapter 6, novel solutions will be proposed.

Next stage will be flaw characterisation. According to latest standards and experts vision, sizing and positioning information can be considered as a main input to the process of flaw characterisation. This can be seen as a further reason behind the importance of flaw sizing and positioning. Next chapter will be discussing the task of automatic characterisation of potential flaws.

Chapter 5

Automatic Flaw Characterisation

5.1 Introduction

Once a flaw has been detected and sized, it is often important to be able to determine its type. This is very essential since defect size, location and type will decide the action needed and whether a flaw can grow to a failure.

This chapter presents a group of algorithms and techniques to build an automatic flaw characterisation stage to be integrated under a comprehensive automatic TOFD interpretation system. For that purpose, the support vector machines (SVM), which has been recently proposed as a very effective method for classification and regression, is used to build a classifier to differentiate between defect classes. For that purpose, discriminative defect features generated using the Wavelet transform are fed to the classifier. Classification based on dimensionality will be discussed in this chapter as well. The proposed techniques apply to D-scan images and the region of interest for that context is the compression waves area.

5.2 Importance of flaw characterisation

Most modern forms of transport and industrial equipment rely heavily on the integrity of steel components with welded joints which are directly or indirectly subjected to large and rapidly varying stresses. To ensure their integrity after manufacture or to inspect them in service, ultrasonic NDT techniques are widely employed. Classification of flaws provides important input to the process of workpieces and structures decommissioning. While planar flaws (cracks) are considered highly critical as they can grow to fail, some other flaws are considered as negligible (e.g. point flaws), and other flaws are considered less critical because they may not grow (e.g. a slag). Accordingly, identifying the flaw category has great importance in ensuring the structural integrity of many structures by detecting the defects that could trigger a failure. Incorrect characterisation of weld flaws may lead to some critical flaws that have not been diagnosed correctly, leading to unnecessary repair or replacement of components, and hence extra cost.

Currently, flaw characterisation is achieved by human operators, a process that involves inaccuracies and inconsistencies and consumes time. Increased industrial pressure to complete the interpretation of inspection data in near real-time has motivated research to develop computational tools capable of aiding the operator by automating the interpretation to classify flaws promptly and accurately.

5.3 Flaw types and classes

Different TOFD standards and codes have come with different flaw class definitions. In general, flaw classification can be categorised based on flaw geometry

(size and location) or visual signatures. Each category has its own supporting standards and codes.

5.3.1 Geometrical classification

Two standards support this classification type: the European Standard ENV 583−6 [63] and the American Standard ASME XI codes [20].

The European Standard ENV 583−6 [63] classifies each defect based on its position from the surfaces into the following categories:

a) Top-surface breaking flaws

b) Bottom-surface breaking flaws

c) Embedded flaws

The ASME XI codes [20] classify crack-like flaws, based on the aspect ratio between the flaw depth and height into the following categories:

a) Breaking one of the surfaces

b) Clear embedded

c) Embedded but approaching one of the surfaces

d) Very small surface breaking

Mainly, sizing and positioning information would suffice as inputs to a classification algorithm that works according to the above classification. In theory, such an

algorithm is not sophisticated and would be implemented by a group of conditional- or if-statements.

5.3.2 Visual signature classification

On the other hand, the British Standard BS 7706 [3] classifies flaws based on their visual signatures. It is fairly detailed in its categorisation of the common flaws in welds, recognising five main categories of flaws, each with a number of sub-categories as follow:

a) Planar flaws (includes upper cracks, internal cracks, lower cracks and lack of fusion)

b) Volumetric flaws (includes lack of penetration and large slag lines)

c) Threadlike flaws

d) Point flaws (includes porosity and small pieces of slag or pores)

e) Uncategorised flaws

Appendix A explains in details these categories with illustrating examples of each.

Each of the above categories has special characteristics and patterns, yet there are some similarities between these categories which make the discrimination between them not an easy task. In general, the classification based on these categories is not a straight forward process and it needs rigorous involvement of computational intelligence classifiers and intensive computations.

More concern is given to the categories and subcategories recognised by the British Standard BS 7706, and its characterisations and patterns have been studied carefully to decide the discriminating features between the various classes.

Table 5.1 shows a summary of the common flaw types according to British Standard BS 7706.

TABLE 5.1: Summary of flaw types according to BS 7706 Standard

Defect type	**Abbreviation**	**Description**	**Illustration**
Upper crack	UC	Opened to the upper surface or very close to it. Returns only one echo from the bottom tip of the crack. Appears as a short straight line and may be accompanied by a loss or a weakening of the lateral wave signal.	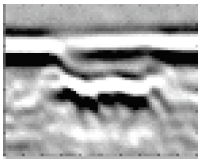

Continued on next page

Defect type	**Abbreviation**	**Description**	**Illustration**
Internal crack	IC	Has two echoes with a distinct phase difference and small irregularities. Appears as two lines above each other.	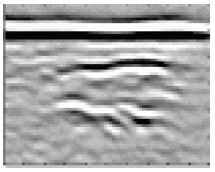
Lower crack	LC	Opened to the lower surface or very close to it. Returns only one echo from the top tip, the bottom echo is masked by the backwall signal. Very difficult to be classified.	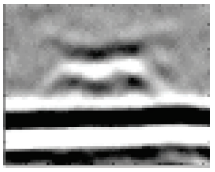
Lack of fusion	LOF	Looks similar to an IC, two lines above each other but without irregularities between the two echoes. Both echoes have similar amplitude.	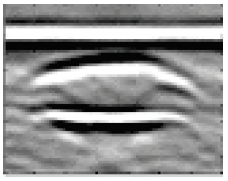

Continued on next page

Defect type	**Abbreviation**	**Description**	**Illustration**
Lack of penetration	LOP	Shows two echoes with an unclear 180° phase difference between them. The echo from the upper tip is larger in size and much brighter than the echo from the bottom tip. There is more than one defect signature for LOP.	

Continued on next page

Defect type	**Abbreviation**	**Description**	**Illustration**
Slag line	SL	Returns two echoes with an unclear 180° phase difference between them. The echo from the upper tip is larger in size and brighter than the echo from the bottom tip. Produces a signal of larger amplitude than a crack. There is more than one defect signature for a SL.	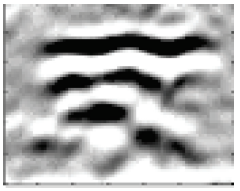
Threadlike	TL	Includes flaws with significant length but little through-wall extent (height). Shows an upper tip echo and no lower tip. Appears to be a cluster of point flaws.	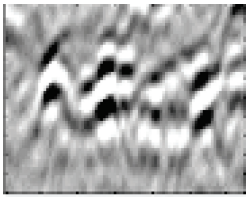

Continued on next page

Defect type	**Abbreviation**	**Description**	**Illustration**
Porosity	PO	Is a cluster of closely pores that have a group of similar echoes with no resolvable length. Each echo shows only the upper tip. Has a pattern similar to acoustic noise and appears as a group of small arcs.	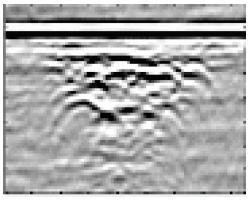

5.4 Phase estimation

An important clue to the characterisation of a flaw indication is the phase of the tip diffraction signals with respect to the lateral wave or the backwall echo. Careful estimation of the phase relations for each defect category is essential for any automatic TOFD interpretation system.

In order to check the degree of matching between two signals, cross-correlation operation can be used. Depending on the value of the resulting cross-correlation coefficient, a decision is made whether the two signals are in-phase or out-of-phase. Accordingly, signals in the outlined defect area (defect blob) is cross-correlated

with the lateral wave or the backwall signals if the phase difference is needed for characterisation purposes.

In this research, the phase relationship between a flaw indication and the lateral wave or the backwall echo is always used in flaw characterisation process to confirm the flaw class.

5.5 Intelligent flaw classification

Defect that are pure internal, i.e. they are clearly embedded and not open to or approaching either surfaces, require advanced visual processing to be classified. This is in contrast with apparent defects that can be classified using geometrical and phase information only. To automatically classify pure internal defects, computational intelligence techniques are the methods of choice. These defects are:

a) Internal crack,

b) Lack of fusion,

c) Lack of penetration,

d) Slag lines,

e) Threadlike, and

f) Porosity.

In the context of automatic classification, machine learning and pattern recognition require extraction of regularity or some sort of structure from a collection of data.

Neural networks (NN) and Bayesian classifiers are typical examples to learn such regularity or structure from the given data observations. Support vector machines (SVM) classifier is relatively new and is based on strong foundations from the broad area of statistical learning theory (SLT). Since its inception in early 1990s, it has found applications in a wide range of pattern recognition problems like handwritten character recognition, image classification, financial time series prediction, face detection, bioinformatics, biomedical signal analysis, medical diagnostics, and data mining, among others.

5.5.1 Support vector machines classification

The SVM classifier has become, in practice, a classifier of choice of numerous researchers and practitioners for several real-world classification problems. This is because it is capable of generalising well (predicting the unseen or unknown samples with a good degree of accuracy) as compared to many traditional classifiers. The SVM classifier offers several advantages which are typically not found in other classifiers [82, 86, 87]:

a) Maximisation of generalisation ability. In training classifiers like NN, the sum-of-squares error between outputs and desired training outputs is minimised. Thus, the class boundaries change as the initial weights change, so does the generalisation ability. Hence, especially when training data are scarce and linearly separable, the generalisation ability deteriorates considerably. Because the SVM classifier is trained to maximise a margin, the generalisation ability does not deteriorate very much.

b) No local minima. Since the SVM classifier is formulated as a quadratic programming (QP) problem, there is a global optimum solution.

c) Robustness to outliers. Classifiers like NN are vulnerable to outliers because they use the sum-of-squares error. Thus, to prevent the effect of outliers, they need to be eliminated before training, or some mechanism for suppressing them needs to be incorporated in training. In SVM, a margin parameter controls the misclassification error. If a large value is set to that parameter, misclassification is suppressed, while if a small value is set, training data that are away from the gathered data are allowed to be misclassified. Thus, by properly setting a value to that margin parameter, outliers can be suppressed.

d) Low computational overhead. The SVM classifier is computationally less intensive (especially in comparison to NN).

e) High dimensional data classification. The SVM classifiers performs well in higher dimensional spaces (a factor which limits many efficient classifiers).

f) Small training data scale. Lack of training data is often not a severe problem for SVM.

g) Error minimisation. The SVM classifier is based on minimising an estimate of test error (structural risk minimisation) rather than training error.

h) Noise reluctance. The SVM classifier is robust against noisy data (noise can severely degrade the performance of NN).

i) Robust to curse of dimensionality. The SVM classifier does not suffer as much from the curse of dimensionality and prevents overfitting.

Before proceeding, the concept of SVM needs to be explained. The SVM classifier tries to maximise the margin between classes which increases generalisation ability. It is fundamentally developed for binary classification case and is extendable for multi-class situation. The classification can be restricted to consideration of the two class problem without loss of generality. In this case, it is required to separate two classes by a function which is induced from an available problem. The goal is to produce a classifier that works well on unseen examples. The basic idea is to build a linear classifier that maximises the distance between a separating hyperplane and the nearest data point of each class [82, 86, 87].

Given some training data:

$$(\mathbf{X_1}, y_1), ..., (\mathbf{X_n}, y_n), y_i \in \{-1, +1\} \tag{5.1}$$

The SVM classifier like other linear classifiers attempts to evaluate a linear decision boundary (assuming that the data is linearly separable) or a linear hyperplane between the two classes:

$$\langle w, x \rangle + b = 0 \tag{5.2}$$

Then, a function $f(\mathbf{X}, W_0) \in f(\mathbf{X,W})$ which best approximates the unknown discriminant (separation) function needs to be found. Linearly separable data can be separated by infinite number of linear hyperplanes that can be written as:

$$f(\boldsymbol{X}, \boldsymbol{W}) = \boldsymbol{W}^T \mathbf{X} + b \tag{5.3}$$

It is required to find the optimal separating hyperplane (see Figure 5.1 (a) and (b)). The optimal separating hyperplane is the one with maximal margin M that is

defined as:

$$M = \frac{2}{\|\mathbf{W}\|} \tag{5.4}$$

This hyperplane is uniquely determined by the points (or vectors) on the margin (called the support vectors (SV)) that satisfy:

$$y_j \left[\mathbf{W^T X_j} + b\right] = 1, \quad j = 1, ..., n_{SV} \tag{5.5}$$

and at the same time, it must separate other data points correctly, i.e., it should satisfy the inequalities:

$$y_j \left[\mathbf{W^T X_j} + b\right] \geq 1, \quad j = 1, ..., n \tag{5.6}$$

where n denotes the number of training data and n_{SV} stands for the number of SV.

With reference to Equation (5.4), maximisation of M means a minimisation of $\|\mathbf{W}\|$. Alternatively, minimisation of a norm of a hyperplane normal weight vector [82, 86, 87]:

$$\|\mathbf{W}\| = \sqrt{\mathbf{W}^T\mathbf{W}} = \sqrt{w_1^2 + w_2^2 + ... + w_n^2} \tag{5.7}$$

leads to a maximisation of a margin M. Because the square root is a monotonic function, consequently, a minimisation of norm $\|\mathbf{W}\|$ is the same as a minimisation of:

$$\mathbf{W}^T\mathbf{W} = w_1^2 + w_2^2 + ... + w_n^2 \tag{5.8}$$

and this leads to a maximisation of a margin M. Hence, the problem is reduced to solving:

$$minimise : \mathbf{W^T W} = \|\mathbf{W}\|^2 \tag{5.9}$$

$$subject\ to\ constraints : y_j \left[\mathbf{W^T X_j} + b\right] \geq 1 \tag{5.10}$$

This is a classic quadratic programming (QP) problem with constraints that ends in forming and solving a Lagrangian [82, 86, 87]:

$$L = \frac{1}{2} \left\|\mathbf{W^2}\right\| - \sum_j \alpha_j y_j (\mathbf{W^T X_j}) + \sum_j \alpha_j \tag{5.11}$$

where L is the Lagrange function and α_js are the Lagrange multipliers.

Once the Lagrange multipliers for the optimal hyperplane have been determined, a separating rule can be used in terms of SV and the Lagrange multipliers.

As mentioned before, SVM foundations are strongly rooted in the SLT, an area of study which addresses the issue of how to control the generalisation ability of a classifier. Vapnik and Chervonenkis [86, 87] developed this theory for creating classifiers or discriminant functions that can generalise well. Normally, classifiers like NN try to minimise the training error (called empirical error) but, statistically, there is no guarantee that such a classifier (with zero empirical error) performs well on the test data. SLT, in contrast, provides an estimate of the test error (called risk) [86, 87, 88]:

$$E_r \leq E_e + c\sqrt{\frac{V(F)}{N}} \tag{5.12}$$

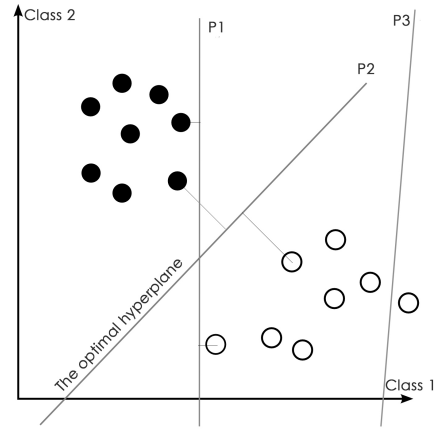

(a) Evaluation of an optimal hyperplane

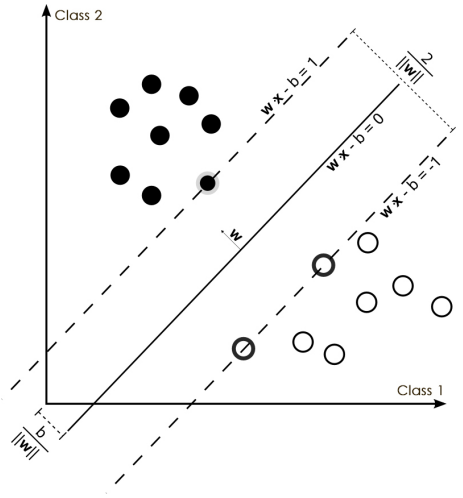

(b) Maximum margin hyperplane

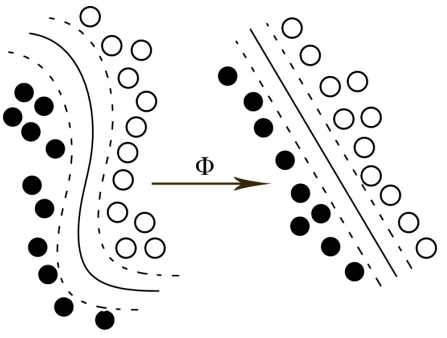

(c) Feature mapping function concept

FIGURE 5.1: SVM classification concept

where E_r is the risk, E_e is the empirical error, c is a constant, $V(F)$ is the VC-dimension (the Vapnik-Chervonenkis dimension), denoting the maximum number of samples that can be shattered by a set of functions [86, 87] and N is the number of training samples. This equation describes the basis of the structural risk minimisation principle. SVM concept, in practice, is based on the minimisation of this risk estimate which often leads to efficient classifiers.

The concepts above are presented for a linear classification case. These are generalisable to a non-linear case where a mapping function $\Phi(x_i)$ is used to map the input space into a higher dimensional feature space such that the non-linear hyperplane becomes linear, Figure 5.1 (c). To avoid the increased computational complexity and curse of dimensionality, a kernel-trick or kernel function $K(x_i, x_j)$ is employed, which, in essence, computes an equivalent kernel value in the input space such that no explicit mapping is required [86, 87, 89].

The kernel functions return the inner product between two points in a suitable feature space, thus defining a notion of similarity, with little computational cost even in very high-dimensional spaces. Kernels commonly used with kernel methods and SVM in particular include the following [82, 89]:

a) The linear kernel implementing the simplest of all kernel functions:

$$K(x_i, x_j) = \langle x_i, x_j \rangle \tag{5.13}$$

b) The polynomial kernel:

$$K(x_i, x_j) = (scale \langle x_i, x_j \rangle + offset)^{degree} \tag{5.14}$$

c) The Gaussian radial basis function (RBF) kernel:

$$K(x_i, x_j) = exp(-\sigma \left\| x_i - x_j \right\|^2) \tag{5.15}$$

d) The hyperbolic tangent kernel:

$$K(x_i, x_j) = tanh(scale \left\langle x_i, x_j \right\rangle + offset) \tag{5.16}$$

The SVM classifier to be used in this research should be able to work on multi-class case. Multi-class SVM classifier aims at assigning labels to instances by using support vector machines, where the labels (class identifiers) are drawn from a finite set of several elements. The dominating approach for doing so is to reduce the single multi-class problem into multiple binary problems. Each of the problems yields a binary classifier, which is assumed to produce an output function that gives relatively large values for examples from the positive class and relatively small values for examples belonging to the negative class. Two common methods to build such binary classifiers are where each classifier distinguishes between

(i) one of the labels to the rest (one-against-all, OAA) or

(ii) between every pair of classes (one-against-one, OAO).

Classification of new instances for OAA case is achieved by a winner-takes-all strategy, in which the classifier with the highest output function assigns the class. On the other hand, classification of OAO case is achieved by a maximum-wins voting strategy, in which every classifier assigns the instance to one of the two classes, then the vote for the assigned class is increased by one, and finally the class with the most votes determines the instance classification [82, 86, 87, 88].

In this research, the multi-class SVM classifier is implemented using OAA method with a 5^{th} order polynomial kernel (Equation (5.14) with degree = 5). For the SVM classifier to function as anticipated, it must be fed with features that are as discriminative in nature as possible. Next section discusses the choice of input features.

5.5.2 Wavelet features

A large variety of feature extraction methods exist which are based upon signal processing (or filtering) techniques. Wavelet filtering is one such method that can be successfully used for feature extraction. The idea of using the Wavelets for feature extraction in classification context is not entirely new and has been applied before to texture analysis, and researchers have been using it for over a decade or so in one form or the other. The inherent capability to do so was highlighted on the MRA using the Wavelet transform [88, 90, 91, 92]. As explained before, Wavelet transform decomposition and its extension, WPT, have gained popular applications in the field of signal and image processing. Wavelet transform enables the decomposition of the image into different frequency subbands, similar to the way the human visual system operates. This property makes it especially suitable for segmentation and classification of images [91, 92]. As far as classification is concerned, appropriate features need to be extracted to obtain a representation that is as discriminative as possible in the transform domain. It is known that proper feature selection is likely to improve the classification accuracy with fewer number of features. A widely used Wavelet feature is the energy of each Wavelet subband obtained after WPT [90, 91, 92].

Two-dimensional WPT decomposition allows analysing an image simultaneously at different resolution levels. Different energy functions can be used to extract features from each subband for classification. Commonly used energy functions include magnitude, magnitude squared and the rectified sigmoid [92]. In this research, the definition of energy based on squaring is used. The energy in different subbands is computed from the subband Wavelet coefficient [91, 92]:

$$\sigma_p^2(k) = \sum_i \sum_j \left[C_k^p(i,j)\right]^2 \tag{5.17}$$

where $\sigma_p^2(k)$ is the energy of the obtained (decomposed) image projected onto the subspace at node (p,k). The energy of each subband provides a measure of the image characteristics in that subband. The energy distribution has shown to have important discriminatory properties for images and as such can be used as a feature for classification.

5.5.3 The feature vector

To train the SVM classifier, a group of data that contains features of each targeted defect type must be applied. Accordingly, each defect area or blob is analysed by MRA-WPT with Daubechies six-tap filter (db6) and three-level decomposition ($L = 3$) to generate decomposition subbands. After each decomposition level, the energies are calculated. A feature vector (FV) of length 12, which contains the energies (four energy values per level), is generated.

The generated FV was tested to check its performance. It was found practically that some regional features need to be considered in forming a final FV that will be used in training of the built SVM classifier. This is because to generate these

regional features, each defect blob is considered as an image containing different shaped regions, and some image processing procedures are applied afterwards.

Mainly, thresholding converts the defect image to a binary image. White regions correspond to background while the black ones correspond to foreground (or vice versa). These regions are referred to as "islands". The threshold value is set so that the lowest 15% of the pixel intensity values within the defect blob are considered redundant, and each pixel in the blob is set to one (white) if its intensity is higher than the threshold and zero (black) otherwise. Figure 5.2 shows this concept.

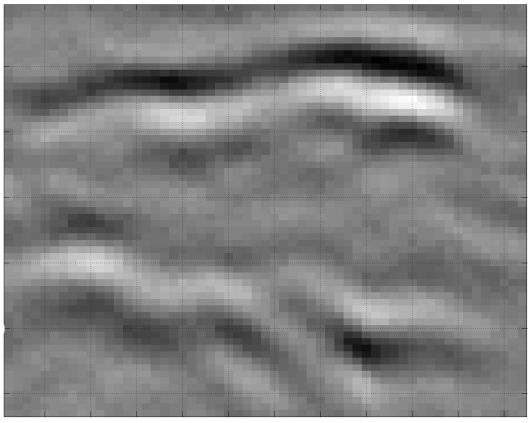

(a) Original defect blob

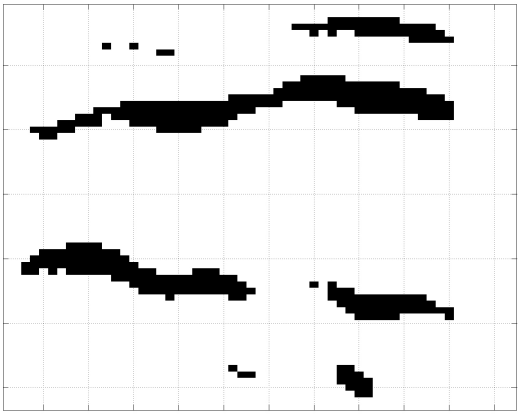

(b) Defect blob after thresholding

FIGURE 5.2: Islands concept of a flaw

Each of the generated islands is assigned a unique label according to the following equation:

$$R_k = k,\ k = 1,\ 2,\ 3, \cdots,\ N \tag{5.18}$$

where R_k is the k^{th} region in the blob from the N regions.

Many regional features can be found and employed in defect classification. The commonly used ones are as follows:

a) Area: represents the total number of pixels in all regions and is given by:

$$A_R = \sum_{i}^{n} \sum_{j}^{m} R(i,j) \tag{5.19}$$

b) Relative area (RA): represents the ratio of the number of pixels in all regions to the area (total number of pixels) of the blob outlining all islands and is given by:

$$A_{relative} = \frac{A_R}{A_{blob}} \tag{5.20}$$

c) Number of positive islands (NPI): represents the number of the islands in the defect blob after thresholding.

d) Total number of islands (TNI): represents the number of the islands in the absolute of the defect blob after thresholding.

e) Solidity: is the area of each island divided by the area of the smallest convex polygon containing that island.

f) Extent: represents the area of each island divided by the area of the smallest rectangle containing that island and is given by:

$$\text{Extent} = \frac{A_R}{A_{rect}} \tag{5.21}$$

where A_{rect} is given by:

$$A_{rect} = (i_{max} - i_{min})(j_{max} - j_{min}) \tag{5.22}$$

Many practical tests were attempted, and as a result it was found that after adding three regional features to the Wavelet energies FV, the performance of the SVM classifier was enhanced against the unseen defects. The three regional features are TNI, NPI and RA.

In a nutshell, the final FV contains 15 values and is expressed as:

$$FV = [WPT\ energy\ values\ (1-12),\ TNI,\ NPI,\ RA] \tag{5.23}$$

5.5.4 Classification performance criteria

The built SVM classifier is used to automatically classify the six pure internal defect that were explained previously. D-scan samples containing these types of defects were used to train and test the classifier after applying the operations mentioned earlier on each defect blob.

The defect blobs have been used to obtain different training and testing patterns. The output of the SVM classifier is a number which codifies each kind of defect as

follows: 1 for IC, 2 for LOF, 3 for LOP, 4 for SL, 5 for TL and 6 for PO. As mentioned previously, the SVM classifier has been trained using 5-degree polynomial kernel implementing the OAA. At the end of the training phase, test patterns are applied and SVM classifier returns a particular matrix, so called confusion matrix (CM) [70, 90], which evaluates the goodness of a trained classifier. Generally speaking, the element CM_{ij} of a CM represents the probability that a single pattern belonging to the $i-th$ class could be classified as belonging to the $j-th$ class (sum of elements of each rows is therefore equals to unity). Thus, the more the CM is similar to the identity matrix, the better classification performance is. The other performance factors that are selected to assess SVM classifier are the classification accuracy (CA) and classification precision (CP). In terms of CM elements, classification accuracy and precision are defined as follows:

$$CA = \frac{\sum_{i=1}^{n_c} CM_{ii}}{n_c} \times 100\% \tag{5.24}$$

$$CP = \frac{1}{n_c} \sum_{i=1}^{n_c} \frac{CM_{ii}}{\sum_{j=1}^{n_c} CM_{ji}} \times 100\% \tag{5.25}$$

where n_c is the number of classes to be discriminated ($n_c = 6$ in the present case). The automatic classification results using SVM classifier will be shown in Chapter 7.

5.6 Automatic flaw classification based on dimensionality

Apparent defects (that are not pure internal) can be classified using the recorded sizing and positioning information from previous stages in addition to the relative phase relationship between the defect echoes and the lateral wave [3]. These defects are:

a) Upper crack,

b) Near surface slag,

c) Lower surface breaking defect,

d) Small pieces of slag or pores,

e) Small surface slag line.

These defects are tackled by an algorithm that is different from the one which deals with the pure internal defects mentioned earlier. First, the algorithm checks the defect blob dimensions and shape to see whether the defect shows one or two tip echoes. In the latter case, the flaw is referred to the SVM classification algorithm because it is considered as pure internal defect. However, if the defect shows one echo only, then this means it may be breaking one of the surfaces, a small surface slag line, or a point flaw. Furthermore, the distance of defect from the lateral wave or the backwall echo is used to decide whether the defect breaks one of the surfaces or it is an embedded defect, while the width of the flaw can be used to discriminate between the small surface slag line and the point flaw. In the case of

a small surface slag line, the phase information is used to differentiate it from an upper crack.

The above procedure is based on the European Standard $583-6$ [63] in classification of flaws according to dimensionality. As mentioned earlier in this chapter, classification algorithm that is based on dimensionality can be realised in theory by a group of conditional- or if-statements. Figure 5.3 shows a flowchart of such algorithm.

In order to achieve a comprehensive flaw characterisation algorithm based on dimensionality, another algorithm was implemented based on the American Standard ASME XI codes [20] that is is used to classify crack-like flaws according to the aspect ratio of the flaw depth to height. A flowchart of this algorithm is shown in Figure 5.4.

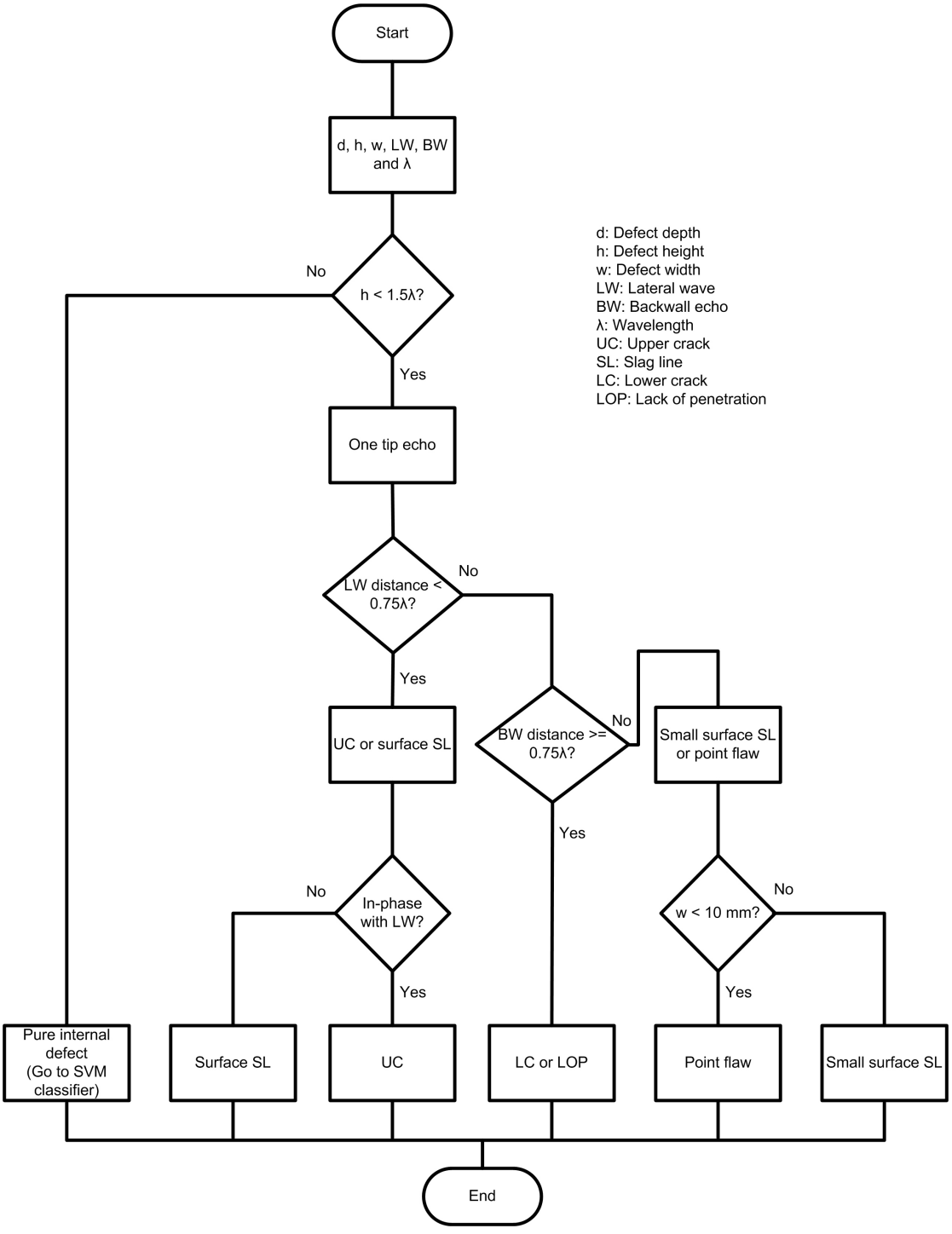

FIGURE 5.3: A flowchart illustrating the dimensional flaw categorisation algorithm based on the European Standard ENV 583-6

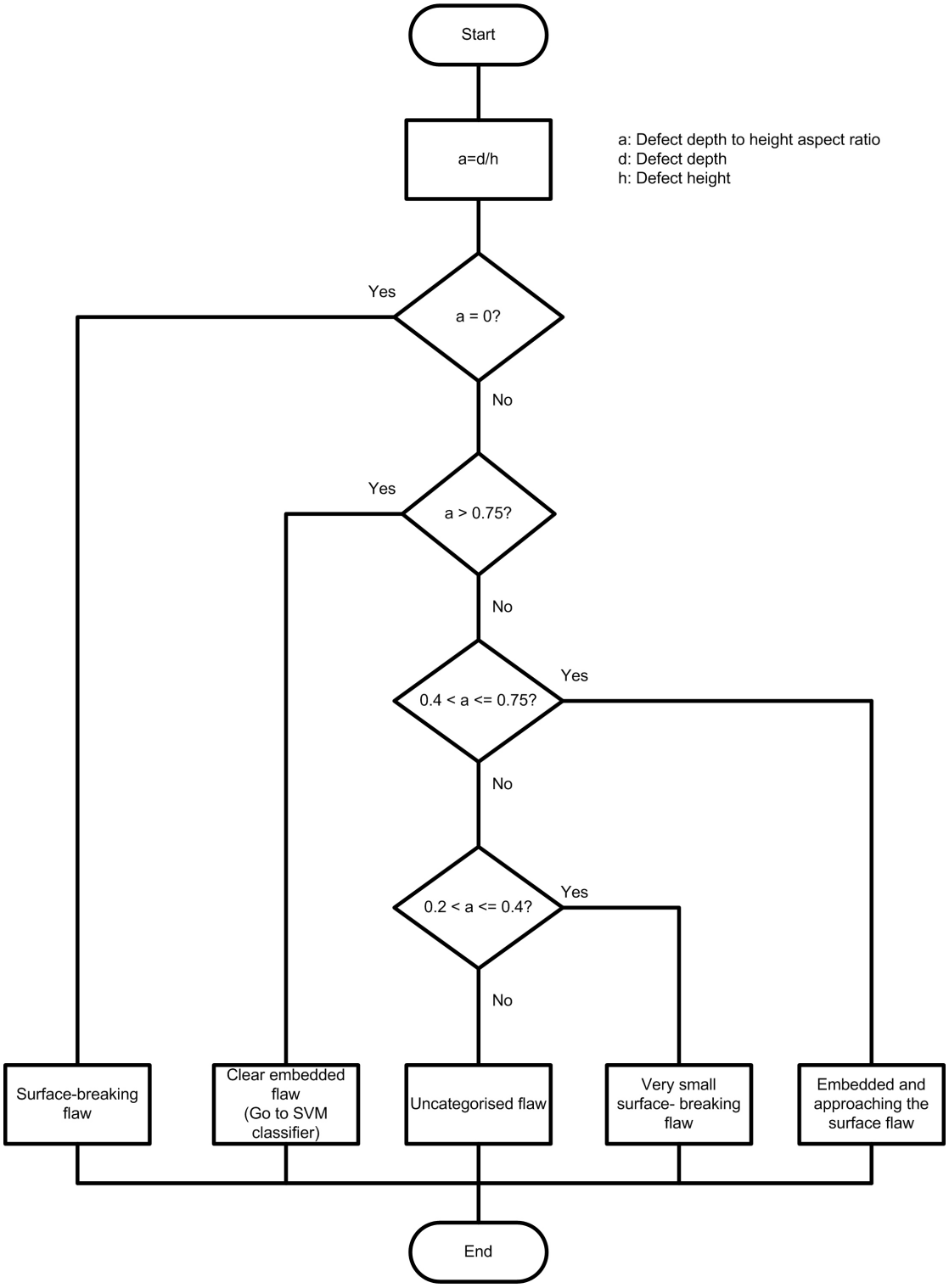

FIGURE 5.4: A flowchart illustrating the dimensional flaw categorisation algorithm based on ASME XI codes (crack-like flaws)

5.7 Summary and conclusions

This chapter has presented several promising methods to aid in automation of TOFD flaw classification. The SVM classifier is used to classify pure internal flaws category and is robust and promising compared to other classifiers (e.g. NN). For that purpose, features taken from the Wavelet transform (more specifically, the MRA-WPT energies) have been used and they seem to be very powerful as inputs to the SVM classifier. Wavelet features have reduced the complexity of the process of feature extraction, and accordingly, no feature reduction methods were needed. For apparent defects, classification based on dimensionality is used. Moreover, two algorithms are implemented based on the European and American standards. These two algorithms are integrated with the SVM classifier to create a comprehensive automatic classification tool that aid human operators in decision-making.

As a personal impression and after discussions with experts in the TOFD field, flaw classification procedures in the future will be more dependent on flaw dimensionality (i.e. sizing and positioning information) as a main input rather than visual signatures.

The task of flaw classification in noisy data can be difficult. The same can be said if the data is collected in poor surface conditions. For that purpose, data pre-processing is crucial along with the use of advanced processing techniques, and interpretation may be extended in this case beyond compression waves region.

Next chapter proposes novel utilisations of the mode-converted waves region in accurate sizing and characterisation of flaws.

Chapter 6

Mode-Converted Waves Utilisation in Flaw Sizing and Characterisation

6.1 Introduction

Manual TOFD data interpretation utilises the compression waves portion of the collected data only and overlooks the mode-converted waves region in general. Even the available automatic or semi-automatic TOFD interpretation methods still consider the mode-converted data as irrelevant and redundant. This chapter shows novel utilisations of the data included in the mode-converted returns for accurate sizing and characterisation of weld flaws. The mode-converted shear waves utilisation is considered as an added value to the D-scan scheme to make it more useful and accurate and comparable with a B-scan. The results achieved so far have been promising in terms of accuracy, consistency and reliability.

6.2 Compression waves region

Compression (longitudinal) waves are used highly in TOFD since they arrive at the receiver first before any possible shear waves and make the specification of a velocity for sizing easier. As mentioned in an earlier context, despite all the good features of TOFD, it suffers from some limitations and inaccuracies. TOFD suffers from a noticeable sizing error of off-axis flaws with D-scans due to the acquisition software misinterpretation. Moreover, detection and sizing of surface and near-surface cracks are always a weakness in any TOFD inspection system [61, 62]. Similarly, flaw classification is sometimes challenging in situations like the presence of high noise or poor scanning surface conditions.

Generally, manual TOFD interpretation depends only on the returns in the compression waves region. The mode-converted shear waves are usually overlooked and considered redundant in most cases, apart from a quick glance by the operator to see if it looks reasonable and appropriate.

6.3 Mode-converted region

Shear waves are produced and received by the probes at approximately half the angle of the compression waves. They may also be generated due to the change of the ultrasonic compression wave propagation upon reflection or refraction at acute angles at an interface or after hitting a reflector (e.g. a defect) inside the material under test. There is nothing to stop shear waves existence in TOFD data. Occasionally, they are useful because of the shorter wavelength for a given frequency and a lower velocity, which spreads the signals out further in time.

Accordingly, the shear wave velocity is smaller (approximately, half of longitudinal wave velocity and hence twice sensitive).

When the crack tip is located at a depth not greater than 67% of the thickness of the material, the backwall reflected longitudinal wave reaches the receiver before shear diffracted wave from the defect tip (will be proven later in Section 6.6). Figure 2.4 has shown a typical A-scan, with region 5 denotes the mode-converted waves portion.

Mode-converted waves can be utilised more with D-scan cases rather than B-scan, as they can give rise to a pattern in the parallel scans which can cause confusion [4]. This pattern does not normally occur for non-parallel scans. Accordingly, the mode-converted region is completely ignored with B-scan scenarios. Figure 2.5 has shown a D-scan and a B-scan with the mode-converted waves region indicated, respectively.

6.4 The utilisation of the mode-converted waves

Mode-converted shear waves appear in the portion of the TOFD image immediately after the backwall echo, and may provide an exceptional resolution of shallow flaws especially when the flaw is located closer (laterally) to one of the probes. In all cases, due to the lower speeds of these echoes, they may provide better resolution of the flaws than in the compressional wave. Although this mode-converted data is often discarded because the diffraction signal is stronger for longitudinal waves than for shear waves and to gain benefits in processing time, there are

instances where examining the patterns in this portion can lead to meaningful insight into the geometry and nature of the flaws.

After a thorough research, it is found that the mode-converted waves region data can be utilised in the following areas (applied to D-scans only):

a) Accurate positioning of off-axis flaws,

b) Accurate sizing of off-axis flaws,

c) Sizing of shallow surface and near-surface defects,

d) Flaw characterisation of complicated flaws or in noisy data and poor surface conditions.

Next sections provide details on each utilisation.

6.5 Mode-converted waves and flaw position estimation of off-axis flaws

Section 4.6.2 has presented the curve fitting method. This method has shown a very important result: it is possible to measure the transverse position of a defect when performing an ultrasonic D-scan by studying how the arcs of a defect indication vary with scan position. This information would normally be obtained only from a B-scan image. This method suffers from one limitation: it does not indicate whether the defect is off-axis to the right or to the left of the weld (direction of the displacement). In other words, the value of X is determined

accurately, but it is not obvious whether this off-axis shift is to the left or to the right of the centre line of the weld. Until now, it has only been possible to overcome this uncertainty by carrying out a B-scan.

To overcome this limitation, a novel solution is proposed here by exploiting the information in the mode-converted region of the D-scan. This region is generally overlooked or discarded when sizing defects, and does not feature in most TOFD standards [3, 63, 67]. Upon close inspection, however, mode-converted returns are highly indicative, as shear waves are twice as sensitive as longitudinal waves, having shorter wavelength and a lower velocity. Recall that the mode-converted waves are generated due to the change of the ultrasonic wave propagation upon reflection or refraction at acute angles at an interface.

It is therefore possible to exploit the fact that mode-converted returns are inherently asymmetric in that the inward (longitudinal) pulse travels faster than the outward (shear wave) pulse. This allows the direction of the lateral offset to be determined by reversing the direction of the beams and comparing the resulting echo times. Figure 6.1 shows two symmetrical flaws and their indications in the compression and the mode-converted waves regions. The two flaws have the same indication in the compression waves region in contrast with the mode-converted region where two distinct indications are present. By checking the time of the two mode-converted indications, the flaws can be concluded to be either closer to the transmitter or the receiver of the scan equipment.

Most commercial equipment used for TOFD scanning can provide the feature of operating multichannel probes concurrently (called software channels). Using this feature (and referring to Figure 6.2), two channels are defined as follows:

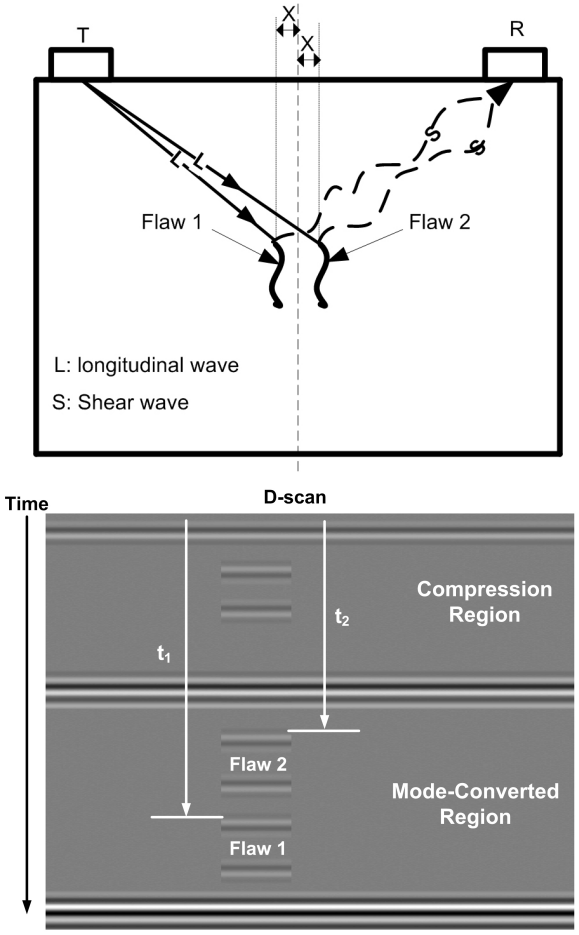

FIGURE 6.1: Time difference between defects in the mode-converted indication

a) Channel 1: Probe 1 is transmitting while probe 2 is receiving.

b) Channel 2: Probe 2 is transmitting while probe 1 is receiving.

As it can be seen from Figure 6.2, the indication in the compression (upper) region shows almost the same position for both transmitter-receiver setups. The difference is found in the mode-converted (lower) region, where there are two different times (t_1 and t_2). As the inward (compression wave) propagation is always faster than the outward (shear wave) propagation, the defect will consistently appear to the shallower (closer to the surface) when the probe closest to it is receiving.

Exploiting this observation allows automatic determination of the direction of offset, and in conjunction with the method explained in Section 4.6.2, the offset and depth error can be all but eliminated.

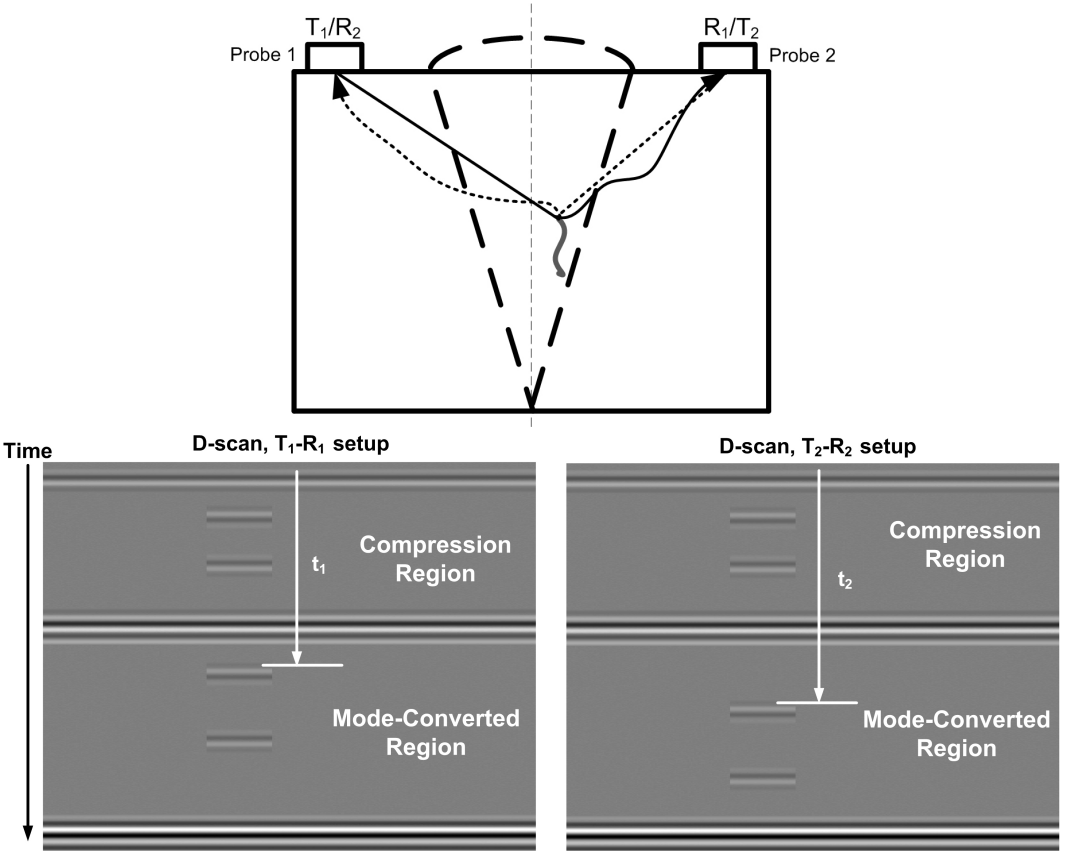

FIGURE 6.2: The flaw is actually closer to R_1 in $T_1 - R_1$ setup (shortest time)

6.6 Mode-converted waves and flaw sizing estimation of off-axis flaws

The previous section shows a possible use of the mode-converted waves to help in accurate positioning of flaws. This section proposes some further concepts, methods and techniques that utilise the shear times of the mode-converted waves

for the task of accurate sizing and positioning of flaws when the conventional methods fail due to data issues, complexity or the presence of shallow defects.

Consider a flaw of height (or length) L and oriented vertically at a depth d from the scanning surface in a component of thickness D (see Figure 6.3). It is required to express the diffracted echo of the top and bottom tips of the flaw in terms of shear times instead of the longitudinal ones. When the the flaw tip is located exactly in the centre line between the probes, then the time-of-flight is straight forward and will be shown in the following steps.

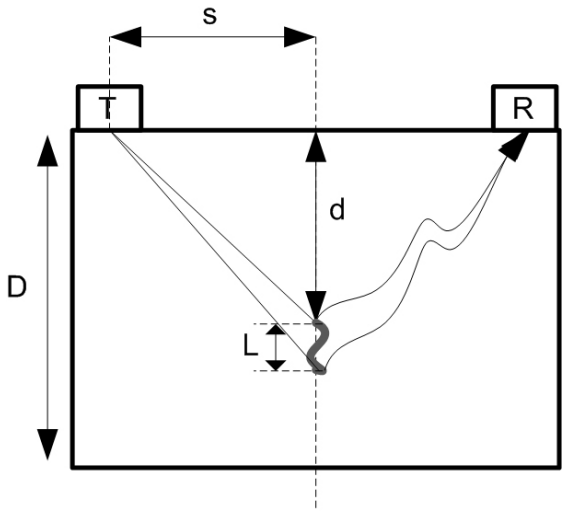

FIGURE 6.3: Typical TOFD representation of a defect lying on the centre line between the probes

The time-of-flight of the longitudinal backwall echo (t_{BW}) can be shown to be:

$$t_{BW} = \frac{2}{v_L}\sqrt{s^2 + D^2} \tag{6.1}$$

where all the parameters have their ordinary definition. The times of the longitudinal-diffracted echoes from the defect top and bottom tips t_{tl} and t_{bl} are given by:

$$t_{tl} = \frac{2}{v_L}\sqrt{s^2 + d^2} \tag{6.2}$$

and:

$$t_{bl} = \frac{2}{v_L}\sqrt{s^2 + (d+L)^2} \tag{6.3}$$

On the other hand, the times for the shear-diffracted (transverse) echoes from the defect top and bottom tips t_{ts} and t_{bs} can be expressed as:

$$t_{ts} = \left(\frac{1}{v_L} + \frac{1}{v_S}\right)\sqrt{s^2 + d^2} \tag{6.4}$$

and

$$t_{bs} = \left(\frac{1}{v_L} + \frac{1}{v_S}\right)\sqrt{s^2 + (d+L)^2} \tag{6.5}$$

where v_S is the shear velocity in the material. Now, relating the two sets of equations for longitudinal- and shear-diffracted echoes, it can be shown that

$$t_{ts} = \left[\frac{n+1}{2}\right] t_{tl} \tag{6.6}$$

and

$$t_{bs} = \left[\frac{n+1}{2}\right] t_{bl} \tag{6.7}$$

where $n = v_L/v_S$. In physical terms, this can be seen as in line with the concept of Poisson's effect in materials. Recall that the Poisson's ratio for a certain object is the ratio of transverse contraction strain to longitudinal extension strain in the direction of stretching force [93]. For the above case, Poisson's ratio is positive and is equal to $(n+1)/2$.

Logically, the shear-diffracted echo must appear after the longitudinal echo so that the longitudinal and transverse waves will not overlap (a situation that happens when the probes are too close together for example). As a result, the shear-diffracted echo from the defect top tip must appear after the longitudinal backwall echo. In mathematical terms:

$$t_{ts} > t_{BW} \tag{6.8}$$

and using the equations above for both terms, then:

$$s > \sqrt{\frac{D^2 - Rd^2}{R-1}} \tag{6.9}$$

where

$$R = \frac{1}{4}(1+n)^2 \tag{6.10}$$

For simplification, it can be assumed that $v_L \approx 2v_S$, then Equation (6.9) reduces to:

$$s > \sqrt{\frac{4D^2 - 9d^2}{5}} \tag{6.11}$$

Equation (6.11) leads to the definition of the minimum PCS required for shear-diffracted echo to appear after longitudinal echo. Based on this equation, it can be concluded easily that the following relation must be met:

$$d < \frac{2}{3}D \tag{6.12}$$

In words, when depth d of the defect tip that is diffracting is greater than 67%

of the thickness D, Equation (6.11) fails, i.e. the diffracting crack tip should lie within 67% of the thickness from the top surface to get the arrival time of shear tip-diffracted signal (t_{tS}) greater than the arrival time of the longitudinal bottom-reflected signal t_{BW}. For a given PCS, the general form of this relation is:

$$d < \sqrt{\frac{D^2 - s^2(R-1)}{R}} \tag{6.13}$$

As a numerical example, for a sample plate of 25 mm thickness, in order to be able to detect a flaw of 3 mm depth, the selected PCS should be taken to be less than 44 mm. This, of course, should be done in conjunction with other system parameters to assure the sensitivity and resolution required to detect that defect.

Returning back to Equations (6.4) and (6.5) and rearranging, the depth of the defect d and length (height) L can be shown to be:

$$d = \sqrt{\frac{v_L^2 t_{ts}^2}{(n+1)^2} - s^2} \tag{6.14}$$

$$L = \sqrt{\frac{v_L^2 t_{bs}^2}{(n+1)^2} - s^2} - d \tag{6.15}$$

As a quick verification, $n = 1$ for the longitudinal incidence and longitudinal diffraction, and Equations (6.14) and (6.15) reduce to the essential time-of-flight equations with longitudinal times:

$$d = \sqrt{\frac{v_L^2 t_{tl}^2}{4} - s^2} \tag{6.16}$$

and

$$L = \sqrt{\frac{v_L^2 t_{bl}^2}{4} - s^2} - d \tag{6.17}$$

Consider now the situation when the crack is off-axis. In this case, there are two possibilities (a flaw that is either off-axis to the right or to the left). Recall that the previous section has discussed and addressed the problem to distinguish between the two possibilities. For that reason, only one case (right off-axis) will be discussed. In this case, the time-of-flight of the diffracted signal from the top tip of the crack due to the shear wave can be expressed as:

$$t_{ts} = \frac{1}{v_L}\sqrt{d^2 + (s+X)^2} + \frac{1}{v_S}\sqrt{d^2 + (s-X)^2} \tag{6.18}$$

and that of the bottom tip is:

$$t_{bs} = \frac{1}{v_L}\sqrt{(d+L)^2 + (s+X)^2} + \frac{1}{v_S}\sqrt{(d+L)^2 + (s-X)^2} \tag{6.19}$$

Equation (6.18) can be solved (numerically) for d to get the depth of an off-axis crack derived from shear wave time-of-flight. Similarly, Equation (6.19) can be solved for L to get the crack length. Symbolic expressions for d and L in this case are much more complicated than the ones in Equations (6.14) and (6.15), and only numerical solution can be found after substituting the values of the other variables. It is worth mentioning that this requires accurate knowledge of the value of X (Section 4.6.2) in order to end up with accurate determination of d and L.

The application of the above technique was found to be significance when the

flaw indication in the compression area (longitudinal waves signature) is not clear, disturbed or noisy while the one in the mode-converted area is clear. The results of this method (will be shown in Chapter 7) were found to be more accurate in estimating the values of d and L.

6.7 Sizing of shallow and near-surface defects

Surface-breaking and near-surface cracks are always overlooked or incorrectly sized in TOFD systems due to the fact that the lateral wave masks most of flaw indication. In most of the cases, there is a clear sign of such flaws in the mode-converted waves region indicating that there is a flaw for consideration. Even though a defect can be detected and sized based on the compression regions indications (longitudinal times), there is no guaranty that the obtained sizing measurements are accurate. It has been found that shear times can be very useful in such cases. Hence, in order to measure accurately the size and position of such flaws, a similar procedure to that mentioned in the previous section can be followed.

6.8 The mode-converted waves utilisation in flaw characterisation

In addition to the compression waves region, flaws in general show indications in the mode-converted waves region that may contain more details and are more indicative. This (as mentioned previously) is due to the fact that shear waves are as twice sensitive as longitudinal waves (on the expense of being slower). This

feature can be utilised in flaw classification topic, especially when the compression waves region flaw indication is weak and not informative [94, 95].

A preliminary work has commenced to exploit this feature towards an automatic flaw classification tool that can classify different types of standard flaws like SL, PO, IC, LOF and LOP. Figure 6.4 shows samples of flaws with their indication in both the compression and the mode-converted regions. It can be seen clearly that mode-converted indication of each flaw contains more details and texture variations than the one in the compression region.

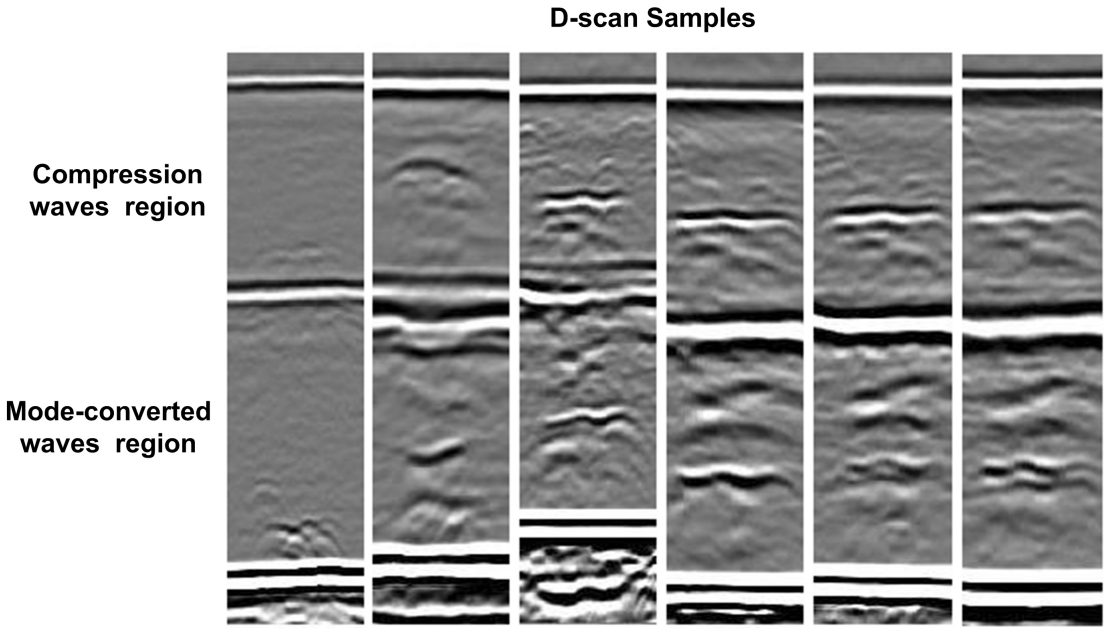

FIGURE 6.4: Sample of D-scans with flaw indications in the compression and mode-converted regions

The classification procedure was implemented using a SVM classifier, which is fed by inputs of a group of regional and statistical features. These features are extracted from each defect blob under consideration. The SVM classifier were trained using a representative set that comprises of 30% of the whole available data. The rest of data (70%) was used for testing purposes. With some tuning to the classifier and the features, a satisfactory classification accuracy was obtained.

More work and details will be shown and published in a future context in this regard.

6.9 Summary and conclusions

This chapter has proposed novel methods based on the use of the mode-converted waves region to enhance the accuracy of sizing and positioning of off-axis defects in ultrasonic TOFD D-scan data as part of a comprehensive computer-aided interpretation tool. The TOFD data acquisition model has been enhanced to take account of the possibility of a lateral offset, and this has been accurately modelled using D-scans alone. Furthermore, the ignored and discarded mode-converted waves portion of the data has been manipulated for the first time to determine the relative flaw displacement, exploiting the inherent asymmetry of the transverse wave propagation path. Sizing of shallow and near-surface defects can be done more accurately by following a similar procedure, and characterisation of complicated flaws or in a noisy environment or poor surface condition can be made more accurate as well.

Accordingly, more valuable results are obtained from D-scans, hence precluding the need for further B-scans, which is considered as a major achievement in terms of reducing the total inspection time and cost. This could potentially open a new paradigm and revolutionise TOFD data interpretation because the utilisation of the mode-converted waves in accurate sizing and classification looks very promising.

Chapter 7

Results and Discussion

7.1 Introduction

During the course of this work, many tests have been attempted and results were obtained. These tests covered all the developed methods and algorithms.

This chapter summarises the relevant results obtained from the work in this project. It also presents the developed GUI tool that is used to run the proposed algorithms.

7.2 Test data

The proposed methods in this research project have been implemented using MATLAB^{TM}, which is a well-known mathematical tool used by engineers and

scientists that saves development time when compared to using a high-level programming language. The developed methods have been applied to a data set of 76 D-scans from steel plates containing 163 weld defects representing different classes as summarised in Appendix B, with the majority being off-axis. The D-scans are collected using a 5 MHz TOFD system and 60° probes with 100 MHz sampling frequency. The plates have thicknesses between 20 and 30 mm, with different defect sizes and depths, all characterised and documented by the manufacturer of the steel plates. They are used for training and examination purposes at Lavender International Ltd, UK, and the scans are independently verified by a trained expert using one of the available commercial TOFD software.

Another data set that contains few D-scan samples was used in testing as well. It contains scans taken from real plates and pipe workpieces.

A GUI was developed to execute the written MATLAB functions that implement the developed algorithms. The GUI was developed using MATLAB graphical tool. Also, there is another prototype GUI that was developed using Visual C++ in Microsoft Visual Studio™ environment. Details of the developed GUIs will be shown later in this chapter.

7.3 Detection results

The developed detection method explained in Section 3.3 that is based on the use of MRA-WPT along with FCMI algorithm has proven to be rapid, accurate and robust. The data set used in the tests is the one shown in Appendix B. Using a PC with Intel Core 2 Duo @3.0 GHz processor running MATLAB R2011a, the

detection result has been achieved in a matter of seconds (between 1 and 5 s) depending on the size of the D-scan image. The output is readily understood by people not routinely involved with ultrasonics as each defect is outlined with a box. The defects in the scan files are successfully detected with a POD of 98.77% (161 out of 163 defects) and a FCR of 5.52% (9 false alarms of 163 defects) due to point flaws that are usually negligible and unreported in manufacturers data sheets. The obtained POD is considered very promising. Recall that the anticipated POD of TOFD is 95%.

7.4 Sizing and positioning results

A combination of the previously discussed methods and techniques in Chapter 4 and 6 have been implemented using MATLAB to size and locate flaws. The developed methods have been applied to the 76 test plates D-scan samples containing 163 weld defects (139 internal defects, 24 surface and near-surface defects) listed in Appendix B. The majority of the achieved results of flaw depth and height are more accurate than manual results (with reference to the manufacturer data sheets), and in a fully automatic and unsupervised manner. For depth measurement, 90% of the obtained results are closer to the actual values, compared to only 10% obtained by a trained operator, and for height measurement, the obtained percentages are 78% and 22%, respectively. This leads to a major error reduction in sizing and positioning process when compared to manual interpretation. For flaw depth and height measurements, the average error when compared to the actual sizing data is less than ± 1 mm for all defect classes except for the surface-breaking cracks where the average error is slightly above ± 1 mm because the flaw echo is merged with the lateral wave or backwall echo. Tables 7.1 and 7.2

quantify the obtained results with a comparison between the automatically computed and manually measured values. The advantage of the automatically computed values can be seen clearly from these two tables compared to the manual ones. Figures 7.1 to 7.4 show the results in graphical means for internal flaws and upper cracks.

The obtained results are also compared to sizing measurements obtained from manual interpretation of B-scan samples for the same investigated flaws, and the result is found to be similar in accuracy performance for 95% of the interpreted samples, with an advantage of 5% only of B-scan over the developed algorithms that deploy D-scans.

The main reasons behind the enhanced sizing and positioning accuracy are found to be the accurate estimation of the off-axis displacement and the use of the mode-converted waves that help in the subsequent flaw depth and height measurements.

TABLE 7.1: Sizing results for 139 internal flaws

	Depth		**Height**	
	Automatic	**Manual**	**Automatic**	**Manual**
Average error (mm)	0.47	1.13	0.43	0.60
Maximum error (mm)	1.40	3.00	1.25	2.00
Accuracy	90%	10%	78%	22%

TABLE 7.2: Sizing results for 24 surface and near-surface flaws

	Depth		**Height**	
	Automatic	**Manual**	**Automatic**	**Manual**
Average error (mm)	1.02	1.33	0.73	1.01
Maximum error (mm)	3.00	3.00	1.79	2.00
Accuracy	54%	46%	79%	21%

Sizing and positioning process has been achieved in a matter of seconds for each scan image (can take several minutes or even hours with manual interpretation,

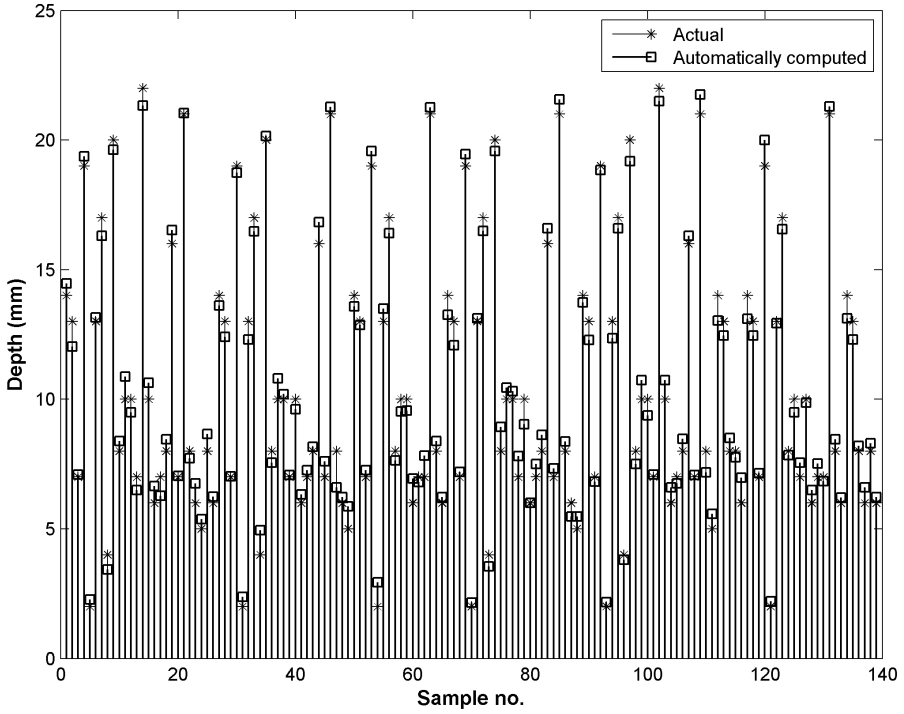

(a) Flaw depth

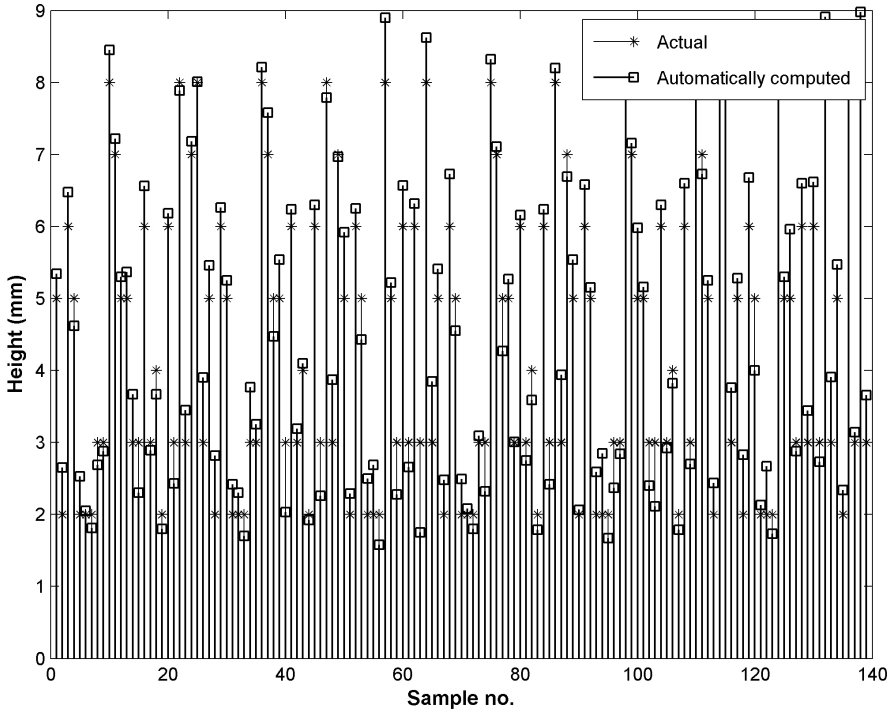

(b) Flaw height

FIGURE 7.1: Comparison between the actual and the automatically computed depth and height for internal flaws

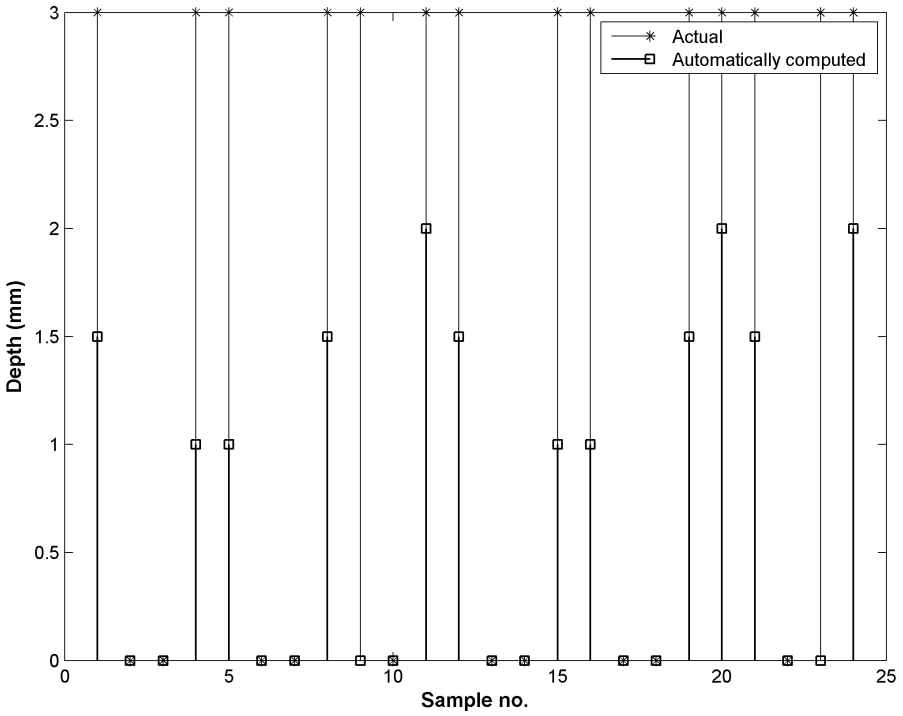

(a) Flaw depth

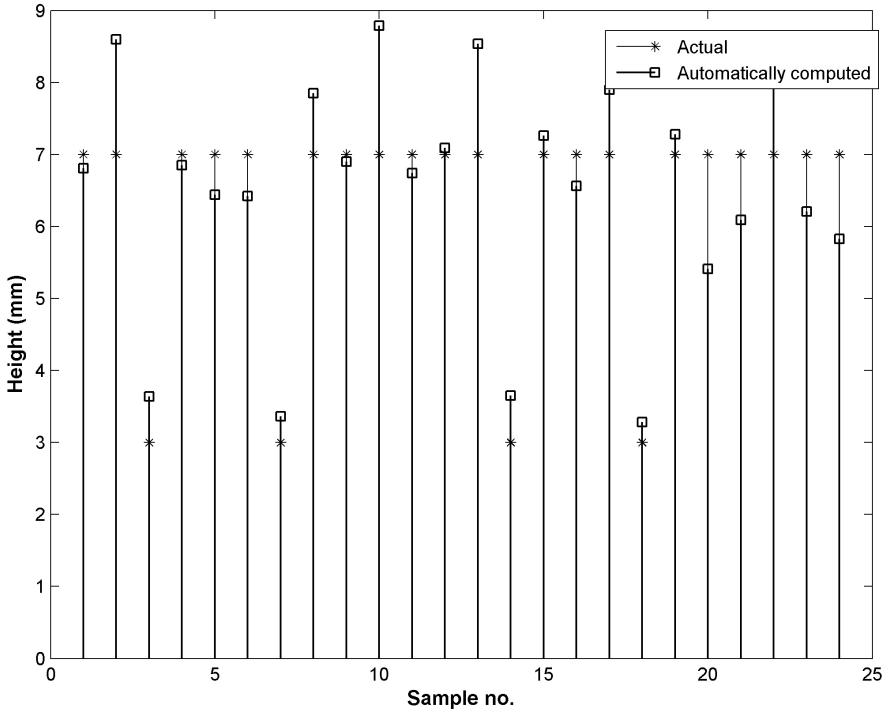

(b) Flaw height

FIGURE 7.2: Comparison between the actual and the automatically computed depth and height for upper cracks

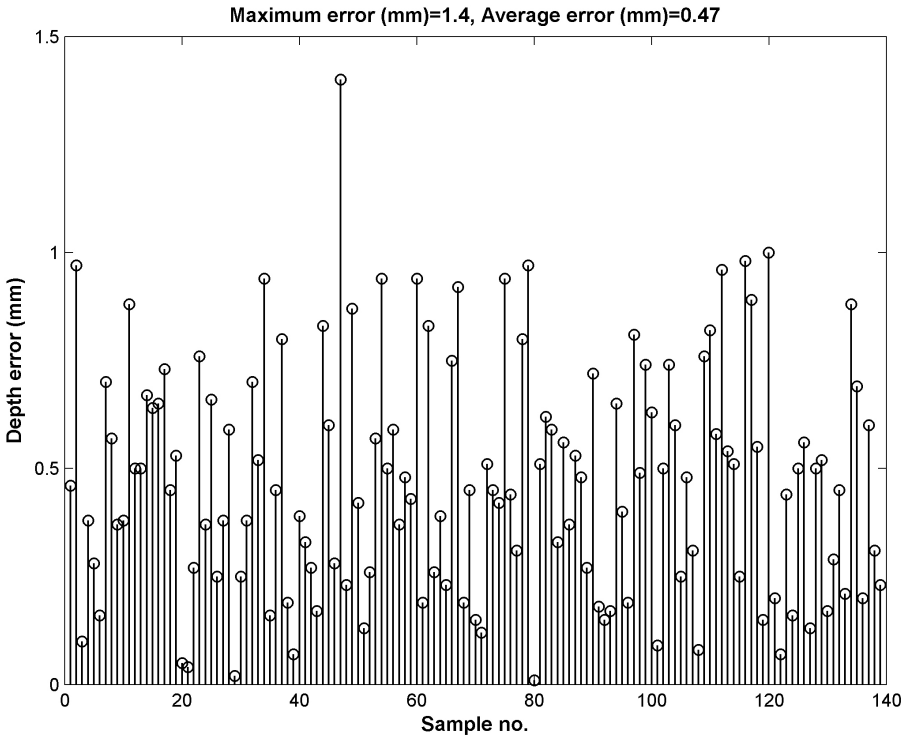

(a) Depth error

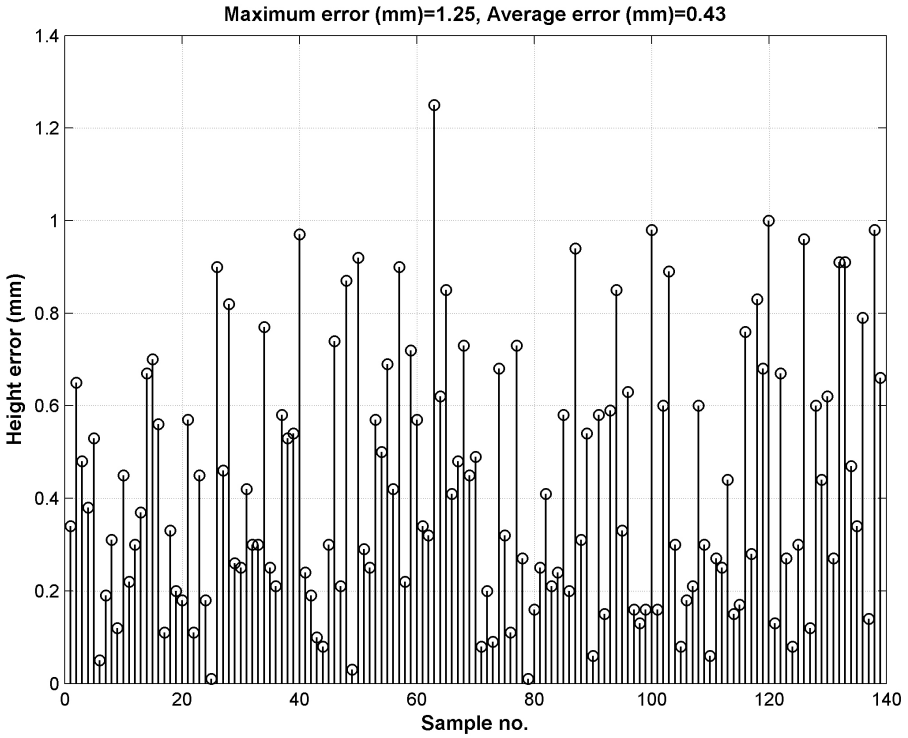

(b) Height error

FIGURE 7.3: Error in calculating depth and height for internal flaws

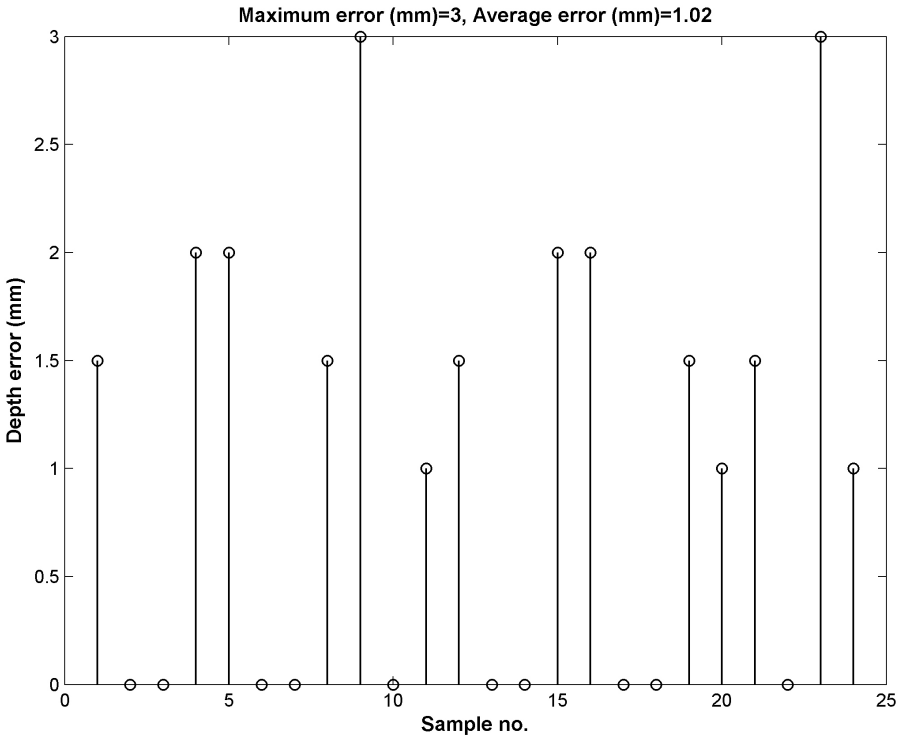

(a) Depth error

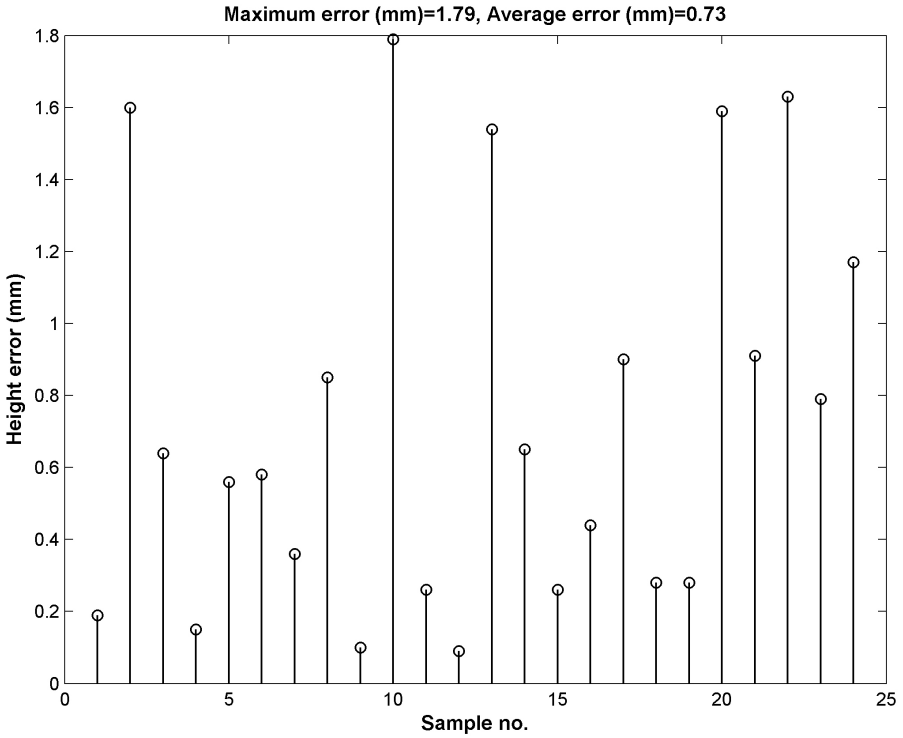

(b) Height error

FIGURE 7.4: Error in calculating depth and height for upper cracks

specifically when cross-check is required) and with very high accuracy, which can be considered as an important achievement from simple D-scans.

7.5 Characterisation results

As mentioned in Sections 5.5 and 5.6, two methods are used to classify flaws. The first method employees an intelligent classifier built using SVM. The developed algorithm for this method is used to classify pure internal defects according to the British Standard BS 7706 [3]. The second method is used to classify apparent flaws based on dimensionality (sizing and positioning) information. For that purpose, two algorithms based on the European Standard ENV $583-6$ [63] and the American Standard ASME XI codes [20] are used.

For pure internal flaws, this research focuses on automatic classification of six flaw types that require advanced visual processing for interpretation. D-scan test samples containing 103 (a subset of data shown in Appendix B) documented defects are used in the SVM classification algorithm. The targeted defects for classification are summarised in Table 7.3 below, along with the corresponding available number of samples per each defect type.

Table 7.3: The used flaw samples for SVM characterisation

Defect type	**Abbreviation**	**Code**	**Used samples**
Internal crack	IC	1	16
Lack of fusion	LOF	2	14
Lack of penetration	LOP	3	8
Slag lines	SL	4	44
Threadlike	TL	5	6
Porosity	PO	6	15

It should be noted that the used feature vector of length 15 is found suitable for classification based on the defect types and the available samples. Larger feature vectors would be needed to classify more defect types to avoid overfitting. The output of the SVM classifier is a number which codifies each kind of defects (from 1 to 6). As mentioned previously, the SVM classifier has been trained using a 5-degree polynomial kernel implementing the OAA method. At the end of the training phase, test patterns are applied and the SVM classifier returns the confusion matrix, which evaluates the goodness of a trained classifier. As mentioned previously, the element CM_{ij} of a CM is the probability that a single pattern belonging to the *i-th* class could be classified as belonging to the *j-th* class. Thus, the more the CM is similar to the identity matrix, the better classification performance is. The other performance factors that are used to assess the SVM classifier are classification accuracy and precision.

The 103 defects have been used to obtain different training and testing patterns. Table 7.4 shows the resulting CM of the developed SVM classifier for three different tests, while Table 7.5 shows the resulting CA and CP. It can be seen from these tables that after applying the built SVM classifier using 23%, 37% and 47% of the available defect samples for training, classification rates of 82%, 92% and 100% were obtained, respectively. The obtained classification rate is rather good for such excercise and shows the potential of the developed SVM classifier.

In the case of flaws that can be classified according to the categories recognised by European Standard ENV $583-6$ [63], a data set of 70 defects is used to test the algorithm, and all the defects are classified correctly using the sizing and positioning information, achieving a 100% classification rate. For crack-like flaws that are classified according to the categories recognised by ASME XI codes [20],

a data set of 46 cracks (24 UC, 16 IC and 6 LC) is used, which contains cracks open to one of the surfaces or clear internal cracks categories. All the cracks in the data set are classified correctly using the sizing and positioning information, achieving a 100% classification rate.

TABLE 7.4: Characterisation tests with the resulting confusion matrix (CM)

	Defect	**Training samples**	**Testing samples**	**Total**	**Confusion matrix (CM)**
Test 1	IC	4	12	16	$\begin{bmatrix} 0.8 & 0.1 & 0.1 & 0.0 & 0.0 & 0.0 \\ 0.1 & 0.8 & 0.1 & 0.0 & 0.0 & 0.0 \\ 0.1 & 0.2 & 0.7 & 0.0 & 0.0 & 0.0 \\ 0.0 & 0.0 & 0.0 & 0.8 & 0.1 & 0.1 \\ 0.0 & 0.0 & 0.0 & 0.0 & 0.9 & 0.1 \\ 0.0 & 0.0 & 0.0 & 0.1 & 0.0 & 0.9 \end{bmatrix}$
	LOF	3	11	14	
	LOP	2	6	8	
	SL	9	35	44	
	TL	2	4	6	
	PO	4	11	15	
Test 2	IC	6	10	16	$\begin{bmatrix} 0.9 & 0.1 & 0.0 & 0.0 & 0.0 & 0.0 \\ 0.0 & 0.9 & 0.1 & 0.0 & 0.0 & 0.0 \\ 0.1 & 0.0 & 0.9 & 0.0 & 0.0 & 0.0 \\ 0.0 & 0.0 & 0.0 & 0.9 & 0.0 & 0.1 \\ 0.0 & 0.0 & 0.0 & 0.0 & 0.9 & 0.1 \\ 0.0 & 0.0 & 0.0 & 0.0 & 0.0 & 1.0 \end{bmatrix}$
	LOF	6	8	14	
	LOP	4	4	8	
	SL	14	30	44	
	TL	2	4	6	
	PO	6	9	15	
Test 3	IC	8	8	16	$\begin{bmatrix} 1.0 & 0.0 & 0.0 & 0.0 & 0.0 & 0.0 \\ 0.0 & 1.0 & 0.0 & 0.0 & 0.0 & 0.0 \\ 0.0 & 0.0 & 1.0 & 0.0 & 0.0 & 0.0 \\ 0.0 & 0.0 & 0.0 & 1.0 & 0.0 & 0.0 \\ 0.0 & 0.0 & 0.0 & 0.0 & 1.0 & 0.0 \\ 0.0 & 0.0 & 0.0 & 0.0 & 0.0 & 1.0 \end{bmatrix}$
	LOF	8	6	14	
	LOP	5	3	8	
	SL	18	26	44	
	TL	3	3	6	
	PO	6	9	15	

TABLE 7.5: Characterisation tests with the resulting classification accuracy and performance

	Training data size	**Classification accuracy (CA)**	**Classification performance (CP)**
Test 1	23%	82%	82%
Test 2	37%	92%	94%
Test 3	47%	100%	100%

7.5.1 Post processing and output representation

Post processing is required in order to generate a simple visual output representation from the developed algorithms that provides flaw detection, sizing and characterisation information to the users (operators).

A visual defect report can be generated after rescaling the axes of the D-scan image. Generally, the axes of the output presentations are related to measurements in the image domain, the horizontal axis is in units of scans and the vertical axis is in samples, and not to the actual depth and width of the scans. Accordingly, these axes are rescaled so that the vertical axis represents the depth whereas the horizontal axis represents the distance, both in millimetres.

The vertical axis can be rescaled to express the actual depths and heights of the flaws by using the mathematical model for time-to-depth conversion which is represented by the equation [2, 5]:

$$d = \sqrt{\frac{c^2 t_r^2}{4} + sct_r - \Delta y^2 + \left(\frac{\Delta y s}{s + \frac{1}{2}ct_r}\right)^2} \tag{7.1}$$

where t_r is the referenced lateral wave time explained previously in Section 4.4.6. This equation is non-linear, and accordingly rescaling the vertical axis to represent depth results is a non-linear scale too.

The horizontal axis is rescaled using values from TOFD acquisition system's parameters, which can be retrieved from the TOFD scan file header. These values are the collection step (the number of collected A-scans per millimetre) and the averaging factor. With a collection step of 10 scans/mm and an averaging factor of 5, each pixel in the horizontal axis represents 0.5 mm.

All information from automatic detection, sizing and positioning and characterisation stages are combined in one simple output image which represents a final visual defect report that is readily understood by people who are not routinely involved in ultrasonic NDT technology. An illustration of this output is shown in Figure 7.5, with all potential defects being highlighted, sized and charcterised, along with an estimate of the exact positions of the lateral wave and the backwall echo. Actual types and sizes of defects in the original scan used to show this output are given in Table 7.6 for comparison purposes.

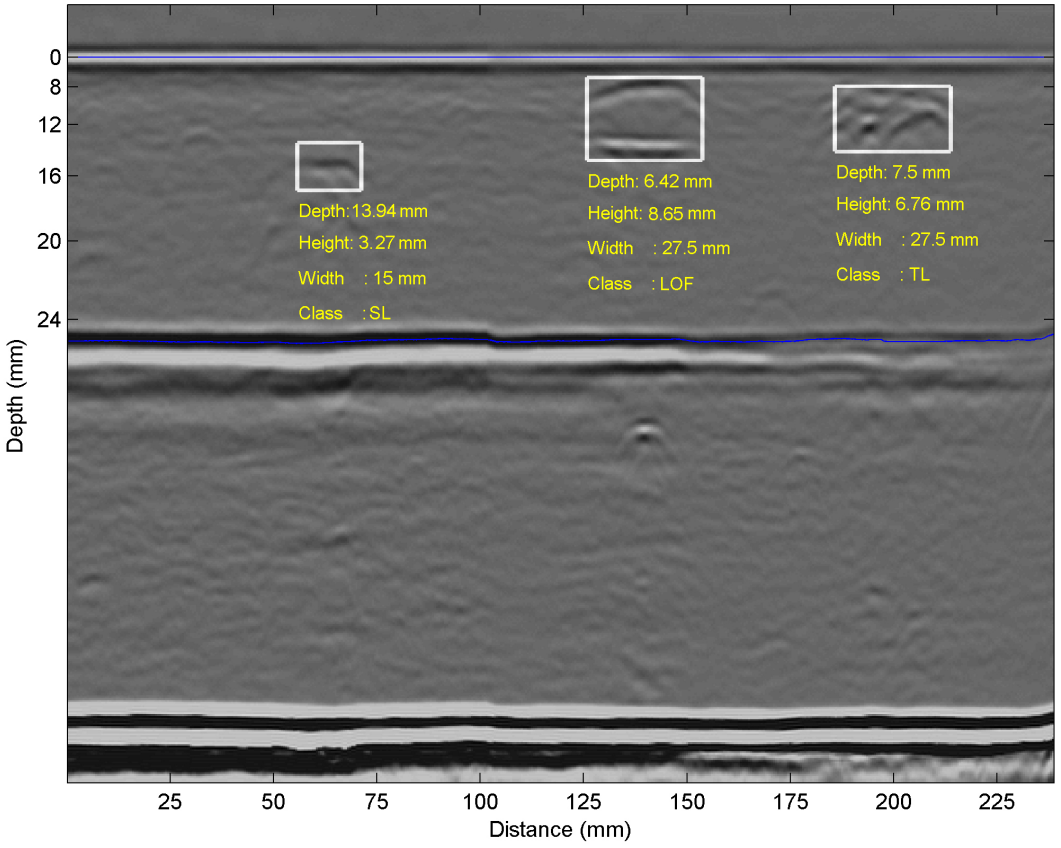

FIGURE 7.5: Final representation of the interpretation results

TABLE 7.6: Actual types and sizes of defects in the original scan used to show the output of Figure 7.5 versus the estimated and computed by the proposed algorithms

		Defect 1	**Defect 2**	**Defect 3**
Class	**Actual**	SL	LOF	TL
	Estimated	SL	LOF	TL
Depth (mm)	**Actual**	14.00	6.50	8.00
	Computed	13.94	6.42	7.50
Height (mm)	**Actual**	3.50	8.70	6.90
	Computed	3.27	8.65	6.76
Width (mm)	**Actual**	16.00	28.00	28.00
	Computed	15.00	27.50	27.50

7.6 The automatic interpretation tool

The available commercial software that is used for TOFD scans interpretation (e.g. TomoView^{TM} and TD-Scan^{TM}) does not provide the facility of automatic interpretation, but rather it helps the operators (inspectors) to open the scan files, detect, size and locate flaws manually by means of cursors and decide on the type of flaws by expert judgment. This interpretation is therefore prone to human error and a time consuming process. Figure 7.6 illustrates an example for an existing commercial software that is used as a tool for manual interpretation. This software, likewise other commercial TOFD software, does not provide any automatic interpretation results or help to the operator, and all sizing and position measurements are performed manually. Section 2.5.12 has provided a list of the capabilities of such software.

One of the important and valuable outputs of this project is an interpretation tool that is very convenient to the inspectors. In contrast to the commercially available software, the developed tool provides automatic interpretation results in a user-friendly GUI environment that offers many capabilities. It has been

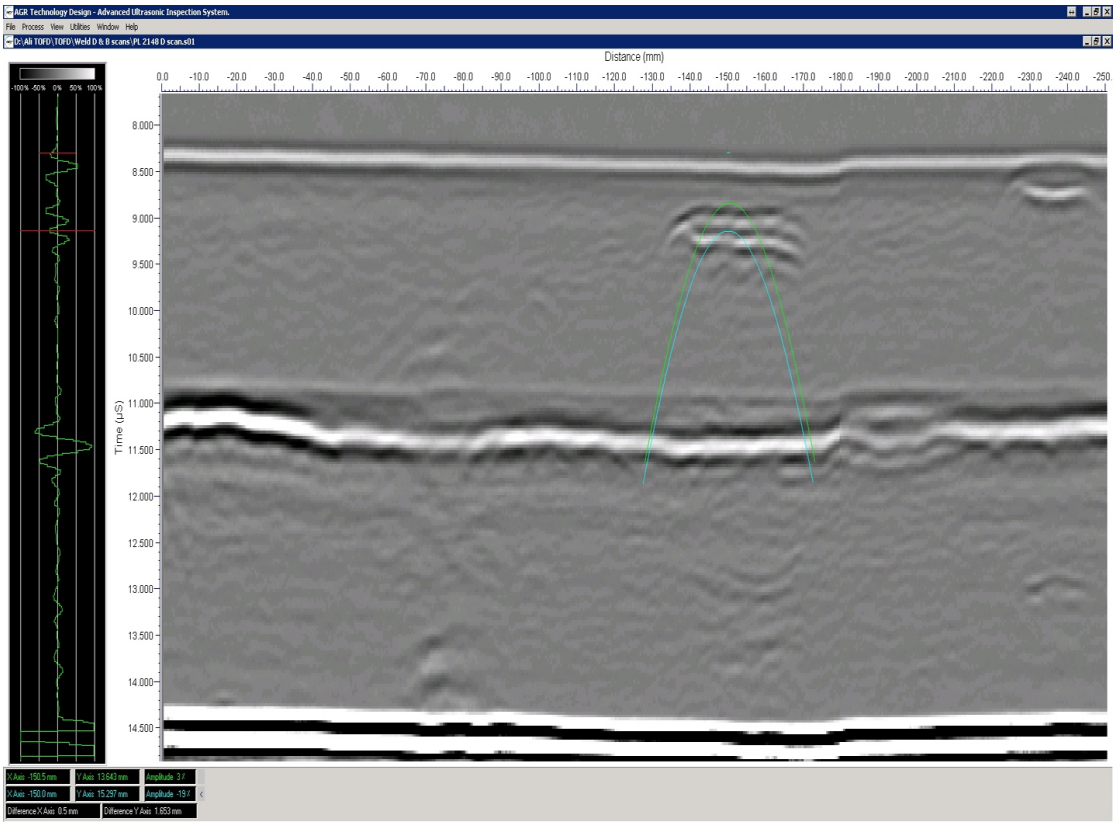

FIGURE 7.6: AGR TD-Scan software screenshot

implemented using MATLAB GUIDE tool in order to facilitate executing the developed algorithms (MATLAB functions).

The tool has a main GUI that shows the available options (6 as shown in Figure 7.7). These options are:

a) Pre-processing,

b) Detection,

c) Sizing,

d) Classification,

e) Mode-converted analysis, and

f) Reporting.

The user needs to load a D-scan data file (by pressing 'Load Data' button), which should be in format readable by MATLAB (.mat for example). When selecting 'Pre-Processing' option, another GUI pops up, which contains different pre-processing functions (Figure 7.8). These are:

a) Wavelet de-noising,

b) Wiener de-noising,

c) Thresholding,

d) Normalising,

e) Alignment,

f) Averaging,

g) Background removal,

h) Cross-correlation analysis,

i) Hilbert transformation,

j) Natural logarithm analysis,

k) Trend removal,

l) Variance image, and

m) Mask image.

It should be mentioned that these pre-processing functions are added to aid visual interpretation and found to be helpful when assessed by inspectors and operators. Recall that in Section 3.2, some pre-processing procedures are explained and they

are in favour of the automatic interpretation, so they are implemented as default pre-processing steps. Figures 7.9 to 7.15 show output examples of the provided pre-processing functions.

Figures 7.16 to 7.20 show the result of executing other options of the tool (namely, detection, sizing, characterisation and reporting). For convenience, a cursor option (Figure 7.18) is also added so that some manual readings can be obtained and verified against automatic results. Besides this option, all GUIs are equipped with facilities like load, reload (refresh), reset and simulation (which shows a report output example).

The built GUI tool provides an output that is more readily understood by people not routinely involved in ultrasonic TOFD inspection, and remarkable performance and user-friendliness. Other options and capabilities can be added to the GUI easily in the future like the ability to provide some recommendations to the inspectors (e.g. performing rescan or additional B-scan), in addition to generating a textual report (along with the visual) automatically based on one of the followed TOFD standards.

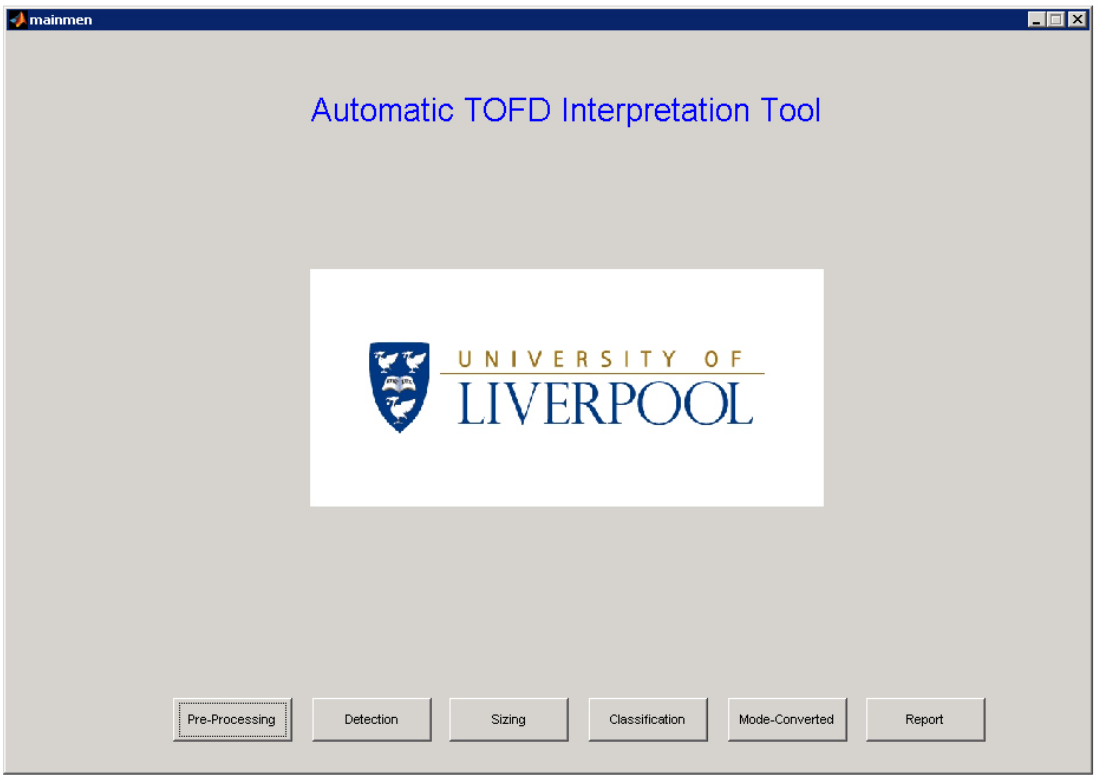

FIGURE 7.7: GUI tool main window

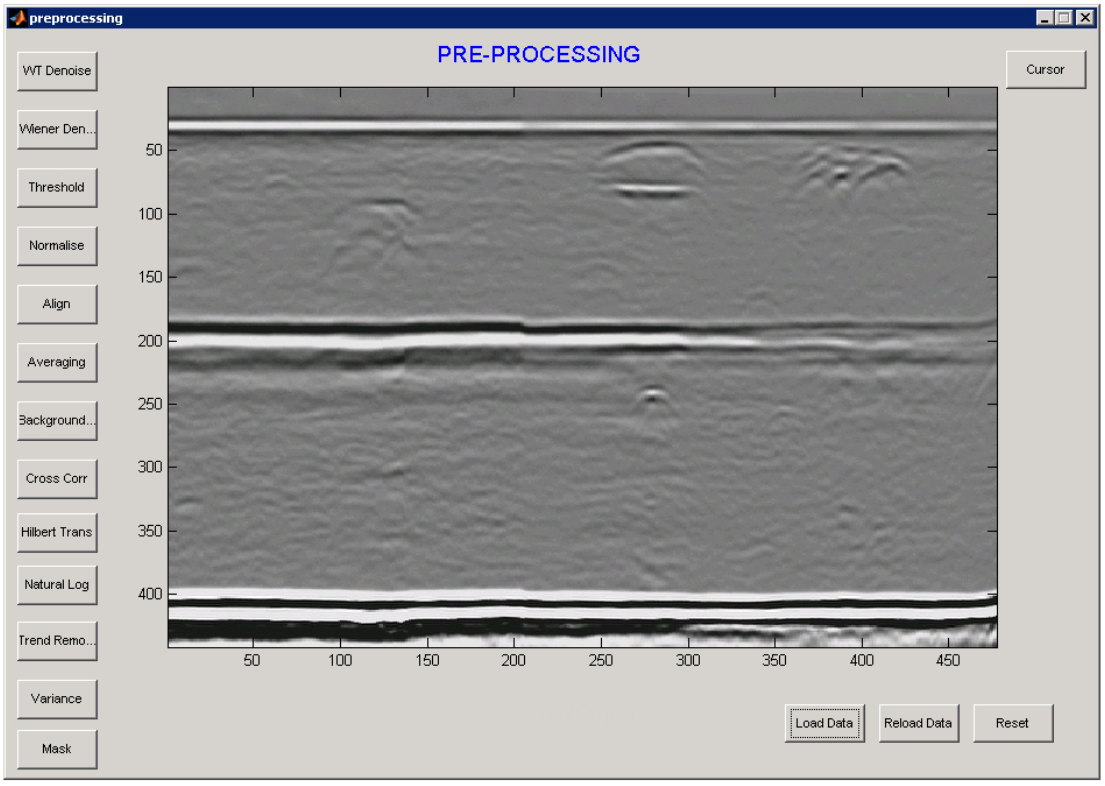

FIGURE 7.8: Pre-processing GUI

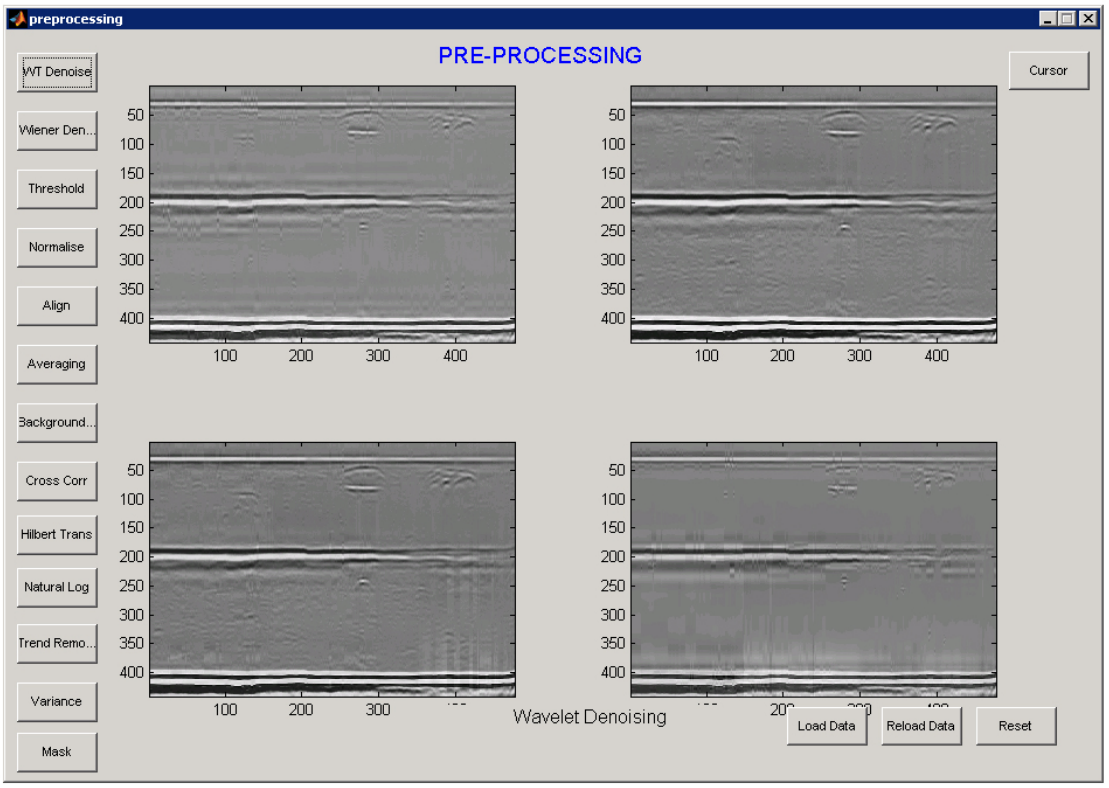

FIGURE 7.9: Wavelet de-noising pre-processing window

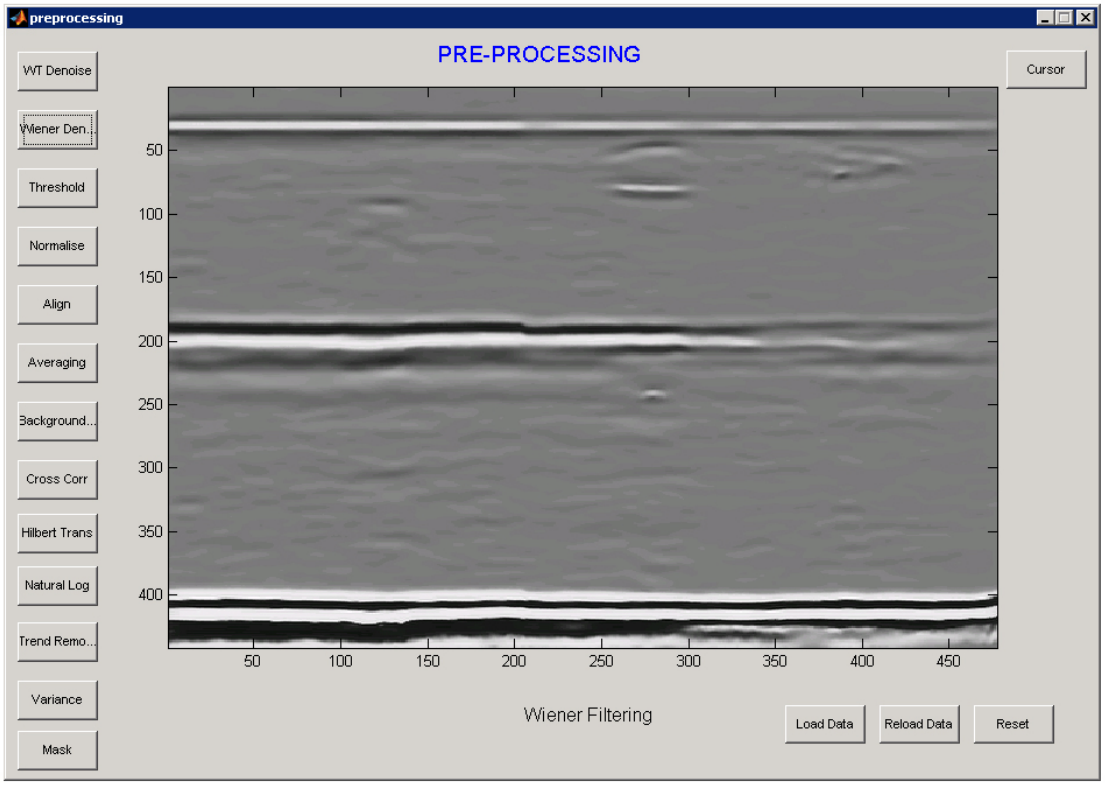

FIGURE 7.10: Wiener filter de-noising pre-processing window

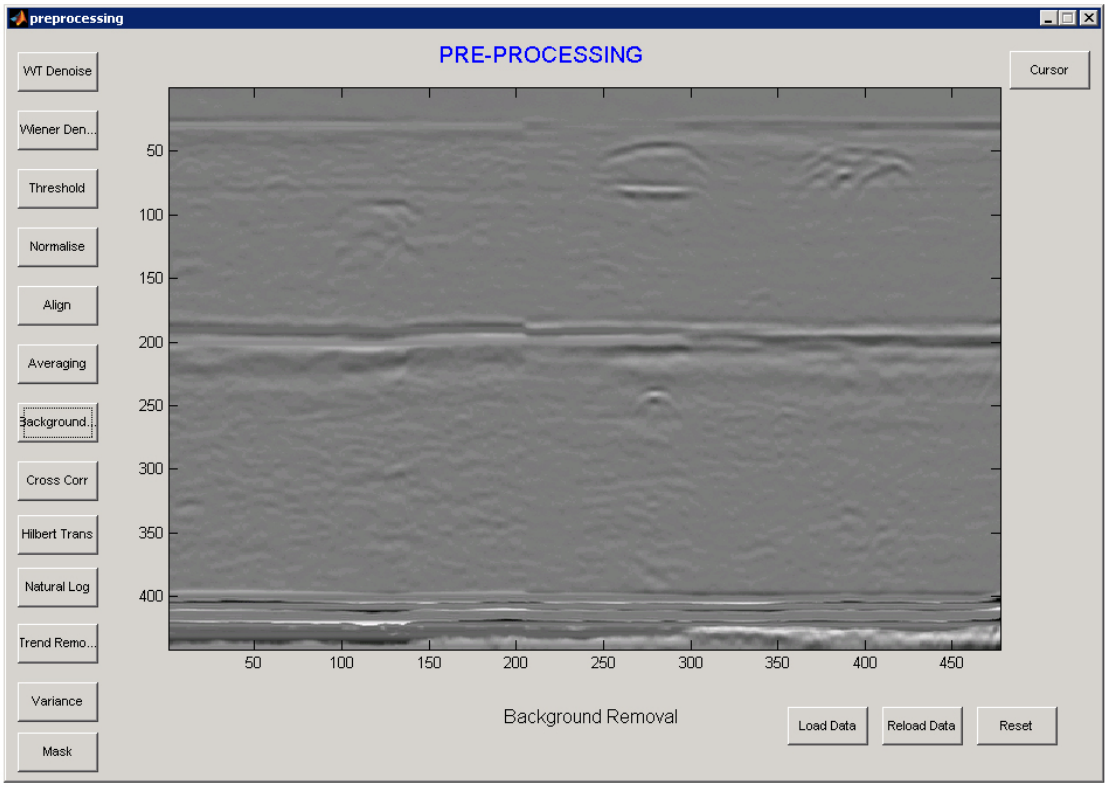

FIGURE 7.11: Background removal pre-processing window

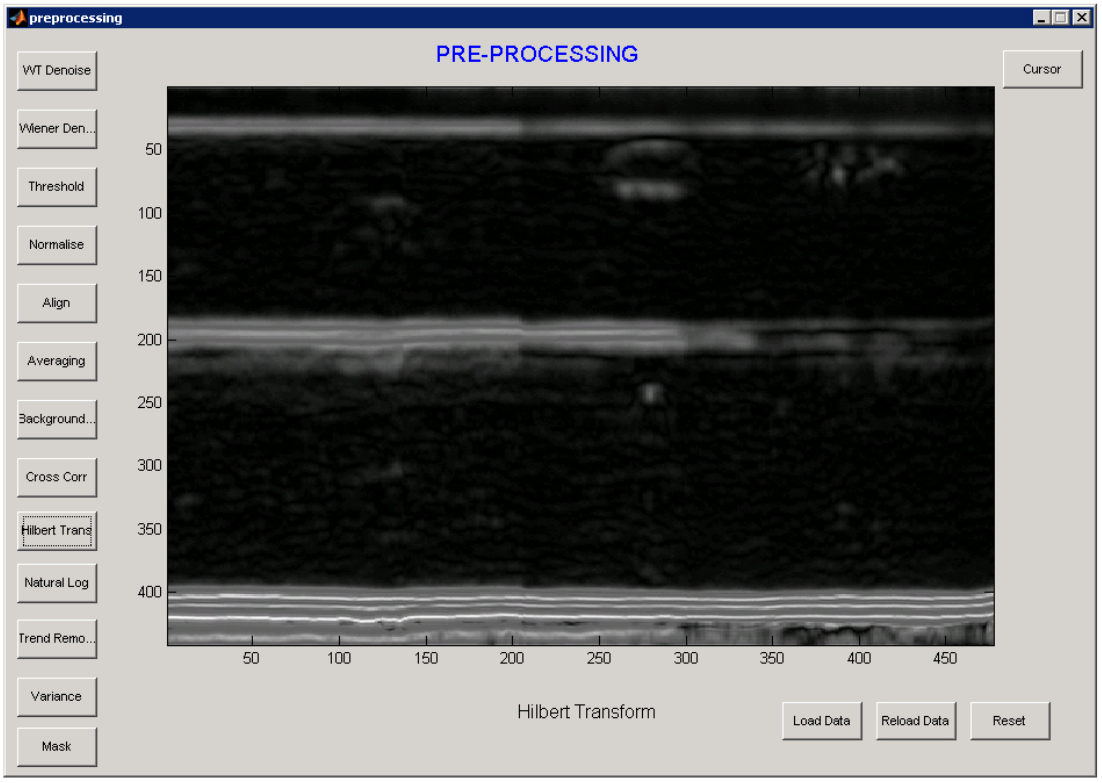

FIGURE 7.12: Hilbert transform pre-processing window

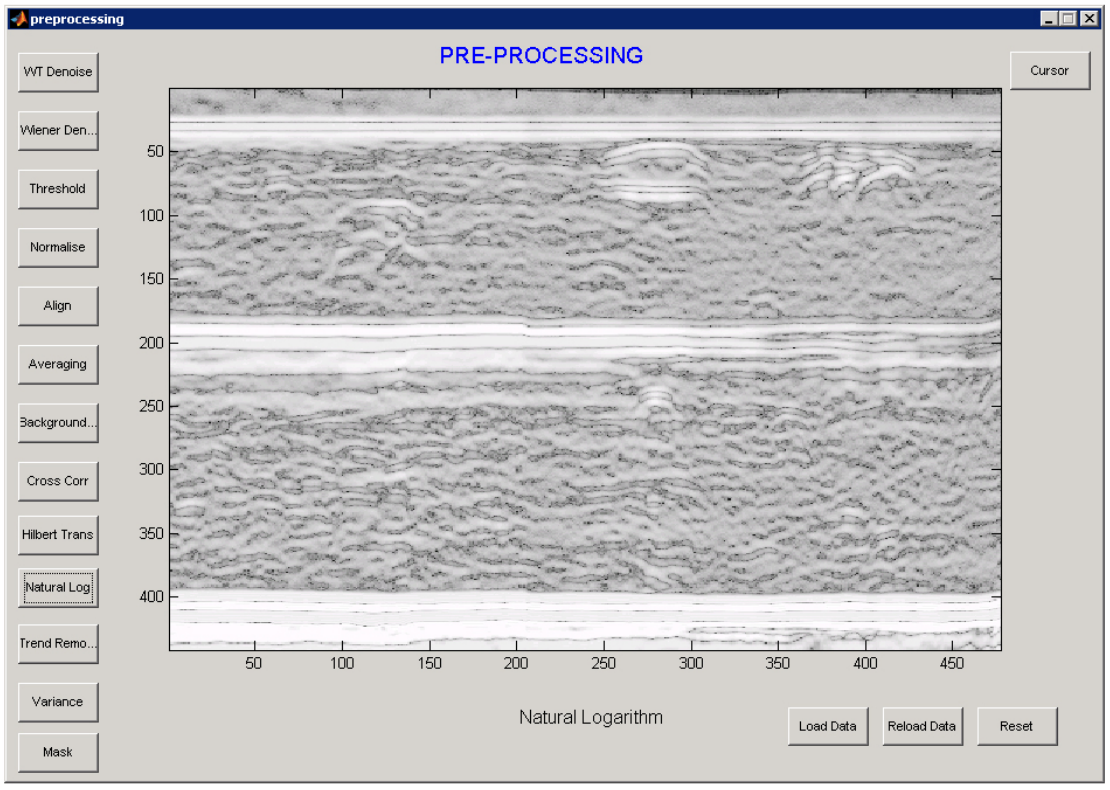

FIGURE 7.13: Natural logarithm pre-processing window

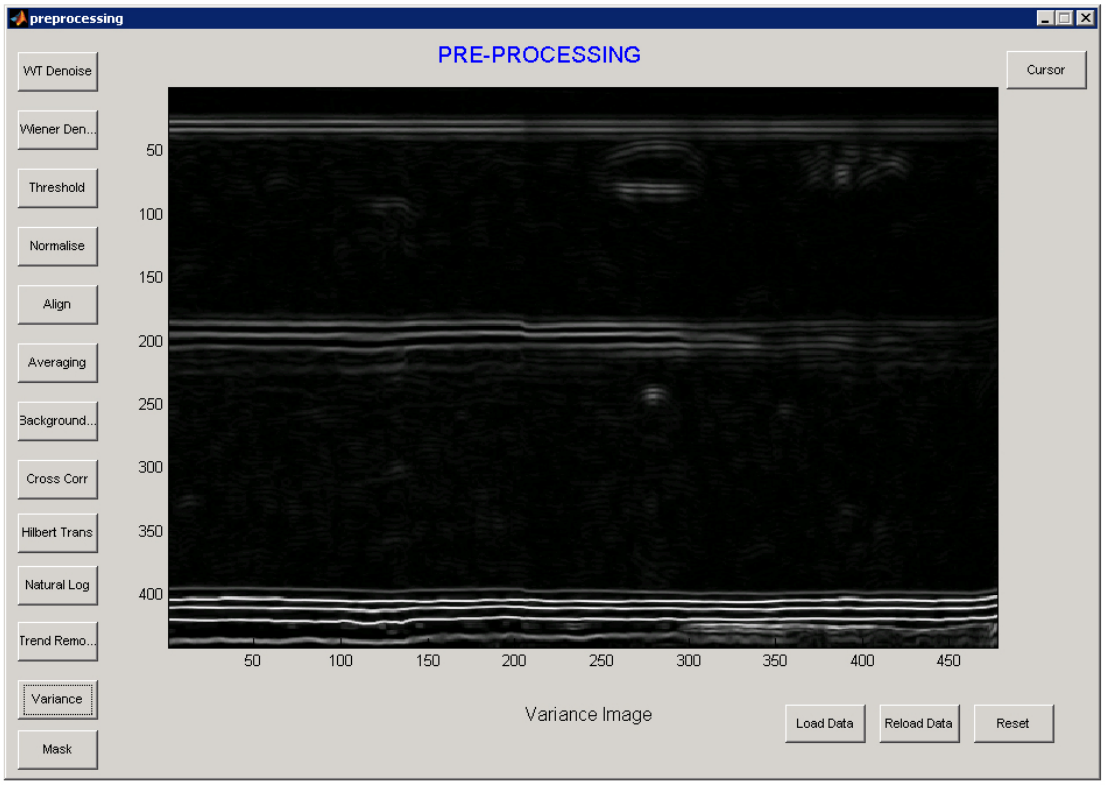

FIGURE 7.14: Variance image pre-processing window

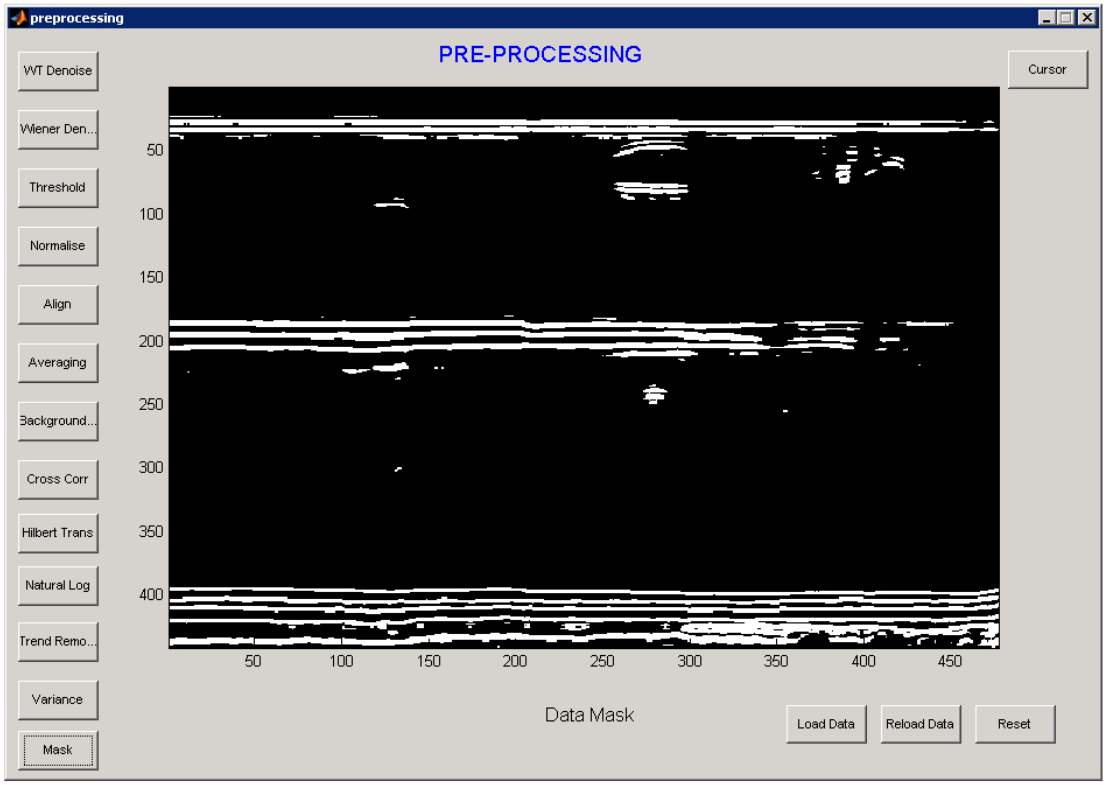

FIGURE 7.15: Mask image pre-processing window

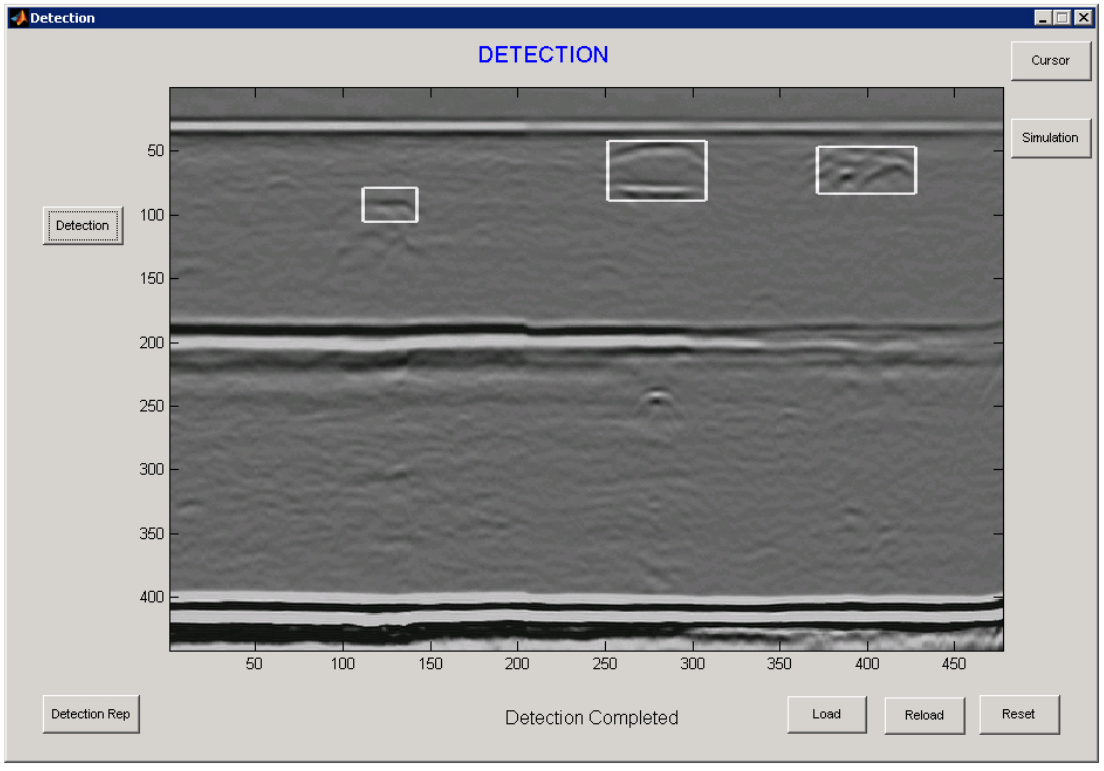

FIGURE 7.16: Detection GUI

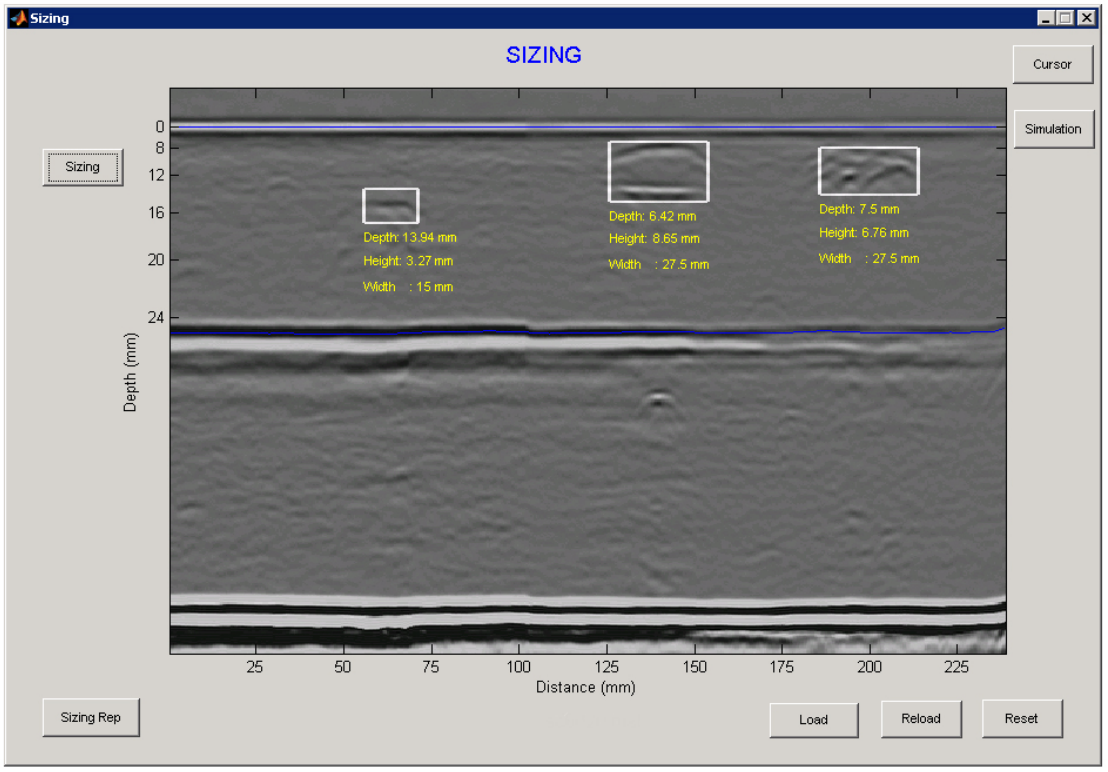

FIGURE 7.17: Sizing GUI

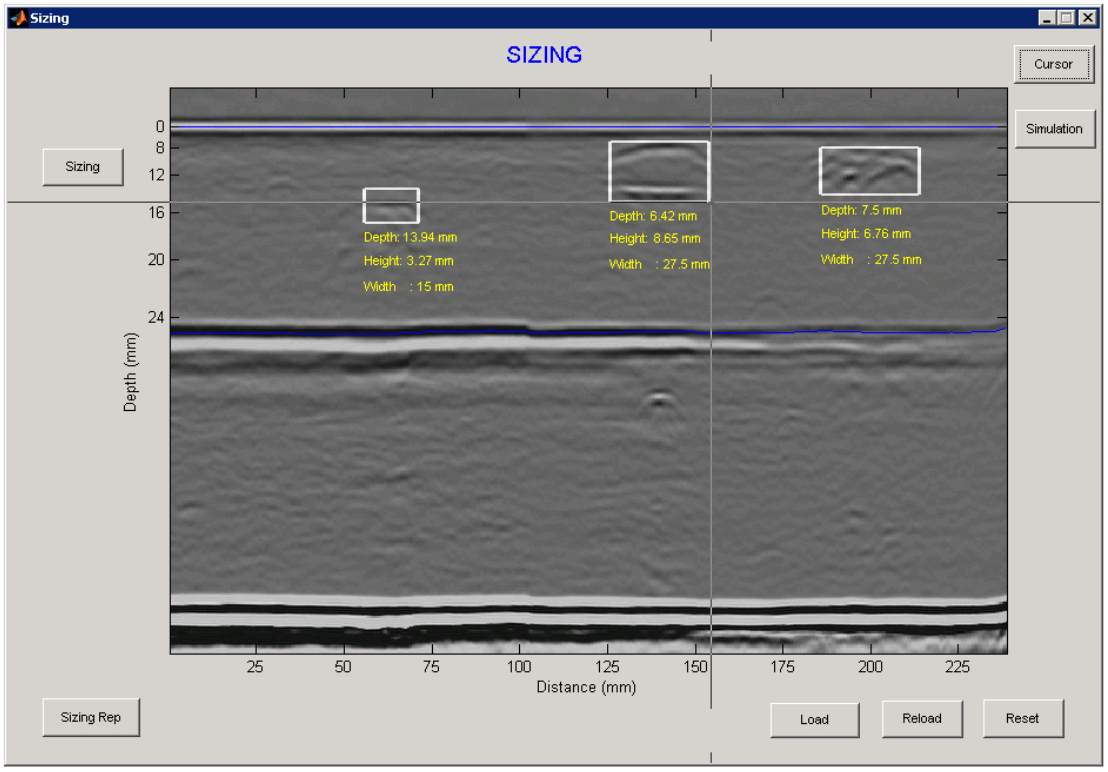

FIGURE 7.18: Sizing GUI with linear cursor option

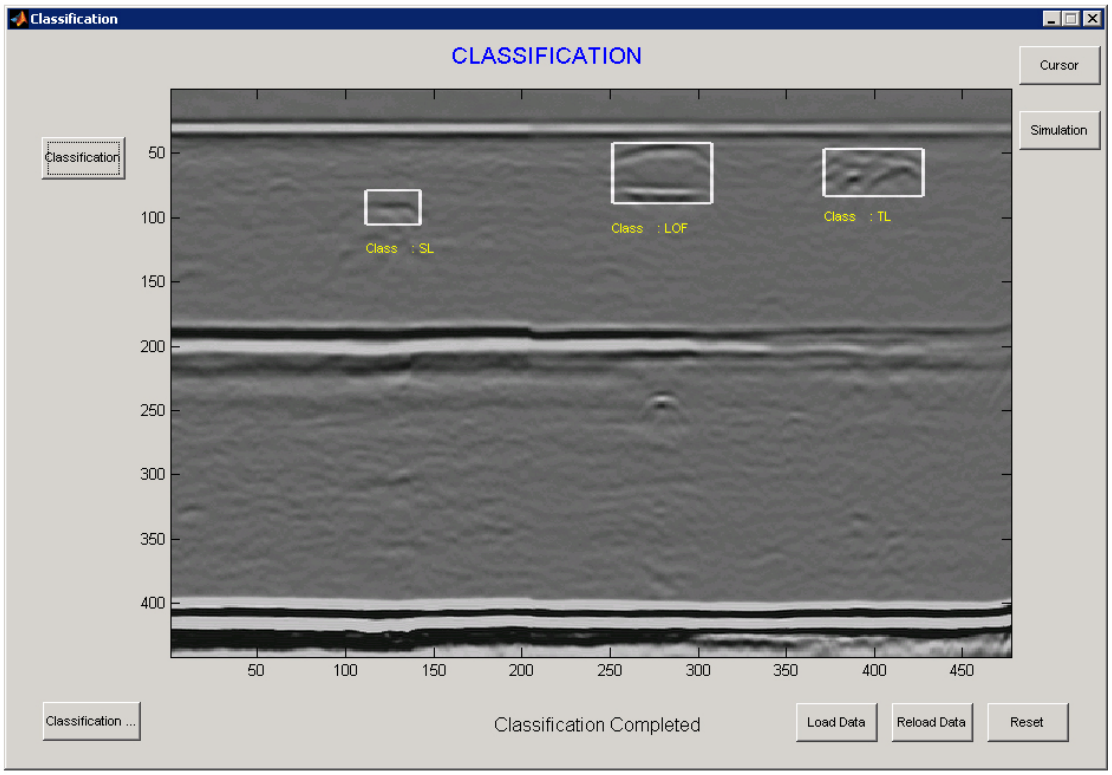

FIGURE 7.19: Classification GUI

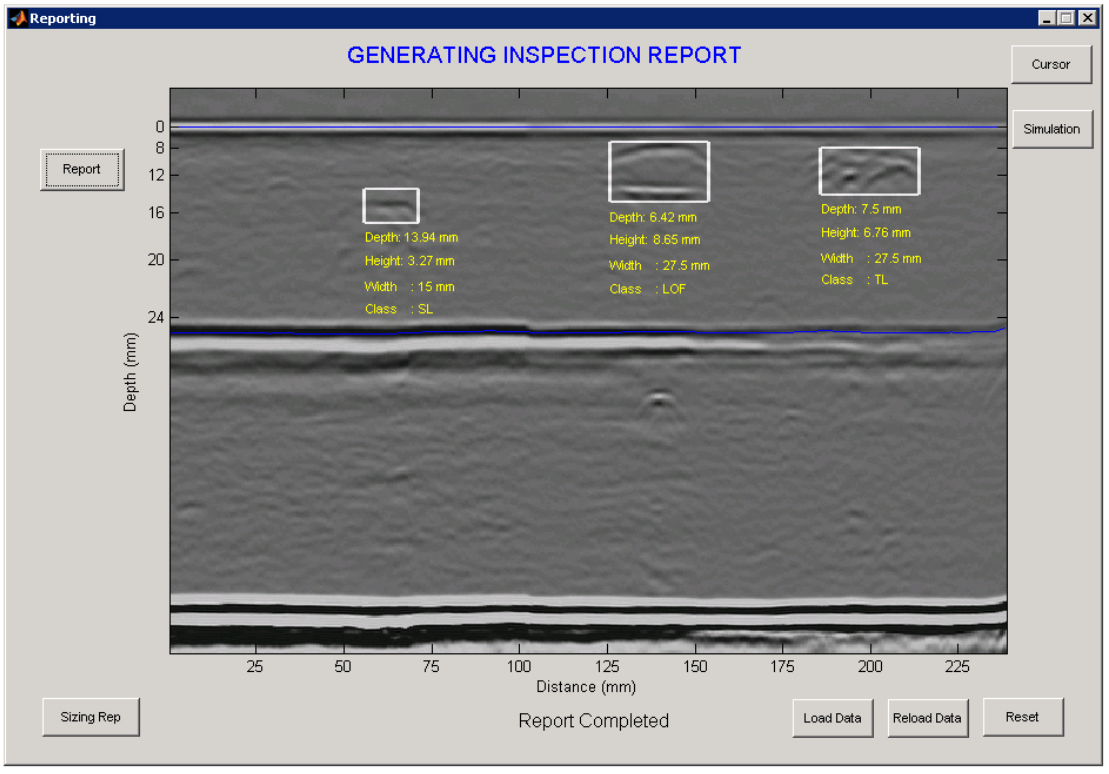

FIGURE 7.20: Visual report GUI

7.7 Interpretation software prototype

It is worth mentioning that another interpretation tool is built, using Visual C++, as a prototype of a bespoke automatic TOFD data interpretation software. Figures 7.21 and 7.22 show screenshots of that tool. The complete software is still under development and it will be packaged as installable application using Visual Studio with all MATALAB functions made available as C/C++ code using MATLAB MEX compiler. Details of the progress in building this software will be published in a future context.

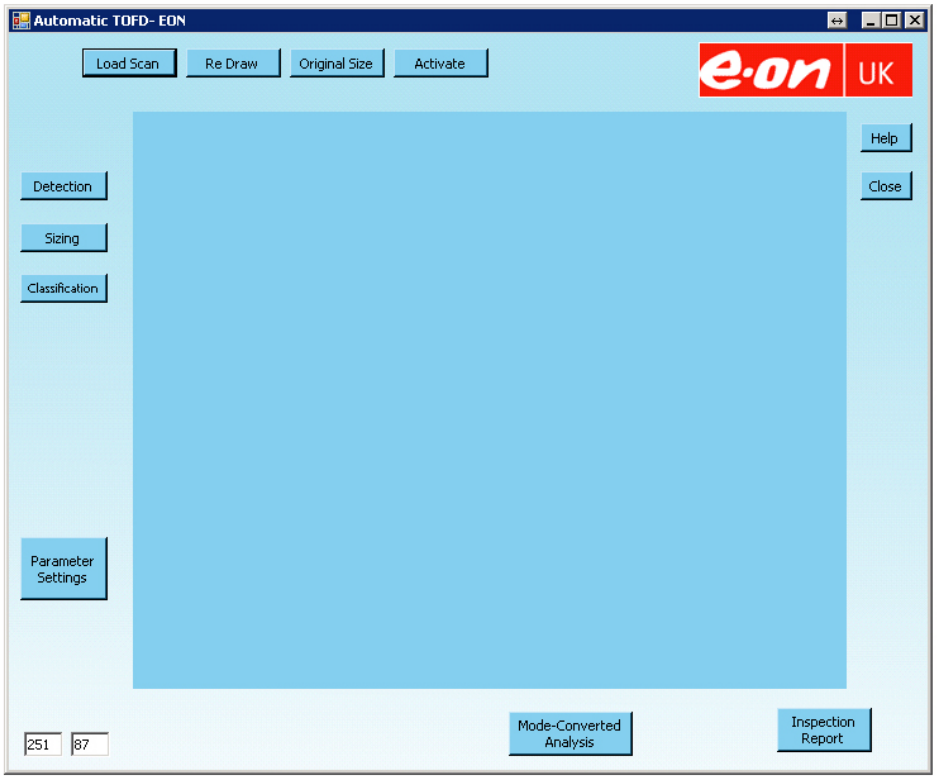

FIGURE 7.21: The prototype software main window

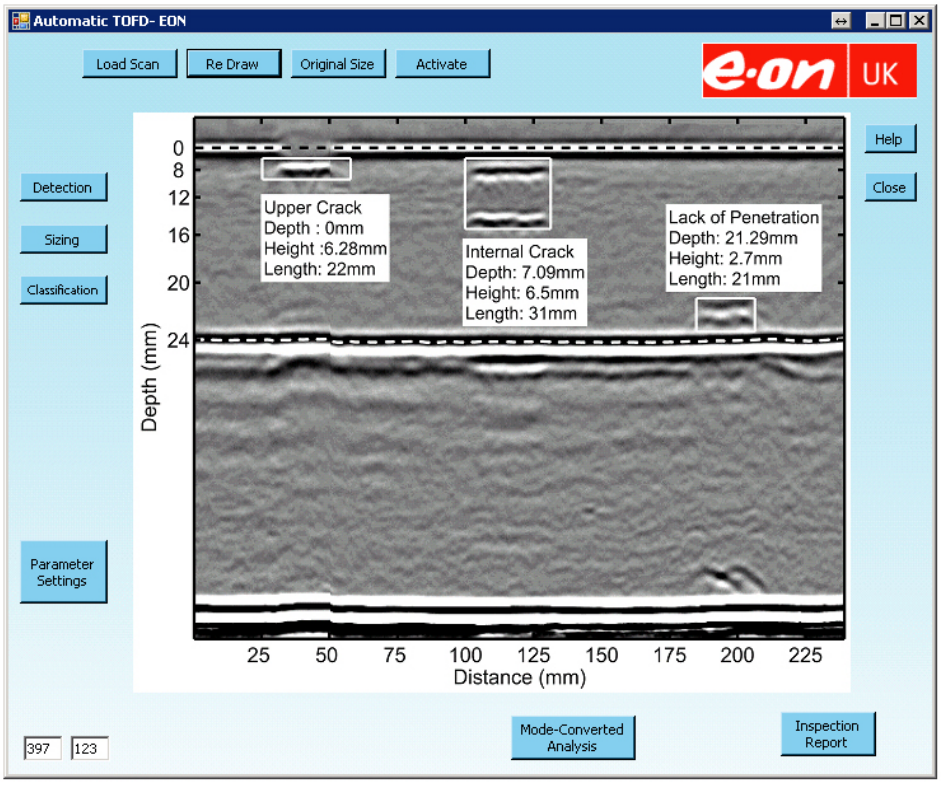

FIGURE 7.22: The prototype software visual report result

7.8 Summary and conclusions

This chapter has shown the results after testing the proposed algorithms and methods to automatically detect, size, locate and characterise weld flaws. All algorithms were implemented using MATLAB as functions, and in oder to facilitate the execution of these functions, a GUI tool was built. The developed algorithms have been verified against variety of documented TOFD D-scan files of steel plates, and different defect classes have been successfully detected, sized and characterised with a consistency and accuracy greater than that of an expert operator and in a fraction of time.

The results obtained so far after using these methods have been extremely promising in terms of speed, robustness, accuracy, error reduction and reliability when

dealing with highly variable data. This would make the proposed techniques suitable in situations requiring automatic (or semi-automatic) near real-time processing and interpretation of large volumes of data, hence, greatly reducing time and human and experimental errors. Valuable results have been obtained from D-scans, hence precluding the need for further B-scans, which is considered as a major achievement in terms of reducing the total inspection time and cost. The main reasons behind this are the use of powerful pre-processing techniques and the utilisation of the mode-converted waves data.

A prototype for an interpretation software has been presented (still under development) which features the use of Visual C++ and MATLAB MEX compiler to create an installable package using Microsoft Visual Studio environment.

Chapter 8

Conclusions and Future Work

8.1 Conclusions

This research has proposed several novel and promising methods to aid in the automation of detection, sizing and positioning and classification of flaws in TOFD D-scan data as part of a comprehensive computer-aided interpretation tool.

A complete automatic interpretation system has been developed to process TOFD data scan files and generate a visual defect report. The system starts by pre-processing the D-scan image as an essential stage to prepare the data for subsequent processing. One of the pre-processing procedures is data de-noising using MRA-WT which was found to impact positively flaw detection and classification accuracy. Scan alignment and lateral wave detection are among other pre-processing steps. Some of the used pre-processing methods have shown visual enhancement to the data, which is in favour of not only automatic interpretation but also manual interpretation by a human operator.

The next stage is automatic flaw detection, which relies on image segmentation, and for that purpose MRA-WPT texture analysis was used along with FCMI algorithm. It should be mentioned that the results of the automatic flaw detection are subject to operator verification and evaluation. Hence, it can be considered as a way to help the operator focusing on specific areas of interest in scan image to aid in making a final decisions regarding potential flaws. Automatic flaw detection provides an important input to the subsequent stages, namely, flaw sizing and characterisation. The complete D-scan image data may not be needed, but rather, defect blobs are processed further in subsequent stages.

Several novel methods have been proposed and accurate flaw sizing and positioning results were achieved. The limitation of off-axis flaws in TOFD data acquisition model has been addressed and enhanced to take account of the possibility of a lateral offset, and this has been accurately modelled using D-scans alone. Furthermore, the ignored and discarded mode-converted portion of the data has been manipulated for the first time to determine the relative flaw displacement, exploiting the inherent asymmetry of the transverse wave propagation path. This is a major breakthrough that may revolutionise TOFD data interpretation regimes. Also, a curve fitting method was used to measure accurately the transverse position of a defect when performing an ultrasonic D-scan by studying how the arcs of a defect indication vary with scan position. This information would normally be obtained only from a B-scan image.

Several techniques and methods have been proposed and implemented successfully to aid in the automation of TOFD flaw classification. The SVM classifier is used to classify pure internal flaws, and it proved to be robust and promising. Features

taken from the Wavelet transform have been used and they seem to be very powerful as inputs to the SVM classifier. Wavelet features have reduced the complexity of the process of feature extraction, and accordingly, no feature reduction methods were needed. For other defect categories, classification based on dimensionality (sizing and positioning information) is used and integrated with the SVM classifier to have a comprehensive automatic classification tool that aid human operators in decision-making process.

The overall response time of performing the above processes using the proposed methods is remarkable. This is because of the inherent data compression ability of Wavelet transform that has been used in different stages of detection and characterisation. The processed images are smaller in size due to this compression, leading to less computations and, accordingly, less processing time.

Overall, the obtained results after using the proposed system have demonstrated remarkable improvements in terms of speed, robustness, accuracy, error reduction and reliability when dealing with highly variable data. This would make the proposed system a preferable option in situations requiring automatic near real-time processing and interpretation of large volumes of data, hence, significantly reducing time and human errors. More valuable results have been obtained from D-scans, hence precluding the need for further B-scans, which is considered as a major achievement in terms of reducing the total inspection time and cost. The main reasons behind this are the use of powerful pre-processing techniques and the utilisation of the mode-converted waves data. The novel utilisation of the mode-converted waves in accurate sizing looks promising and can be thoroughly investigated to explore its potential further.

An intuitive GUI tool was built, offering many capabilities to the inspectors. The

built GUI tool provides an output that is more readily understood by people not routinely involved in ultrasonic TOFD inspection, and shows very good performance and user-friendliness.

The developed TOFD interpretation algorithms have been verified against variety of documented TOFD D-scan files from steel plates, and different defect classes have been successfully detected, sized and positioned and characterised with a consistency and accuracy greater than that of an expert operator and in a fraction of time.

An improved accuracy of sizing and positioning measurements have been demonstrated from D-scans only (comparable to B-scans), and consequently, new inspection regimes and TOFD standards must take this result into consideration. A single good quality D-scan can provide enough information to inspect a component accurately rather than having many D- and B-scans.

Available TOFD standards do not have codes and definitions for an automatic TOFD data interpretation system, and there is a need to develop such codes to provide acceptance criteria and verification and validation processes. The system proposed in this research and the obtained results can definitely feed in to this purpose.

Automation of TOFD data interpretation is a challenging task, yet not impossible. The tools presented in this work are not meant to replace human operators but rather help in minimising time, aiding in decision-making and reducing errors.

Next generation of ultrasonic TOFD needs to deal with thick wall stainless steel

plates and high-pressure, high-temperature pipes (that will be used in power generation field for example). This would definitely lead to complicated inspection routines. Hence, advanced signal processing and computational intelligence techniques to detect, size and characterise flaws will be needed, and the proposed methods in this work are expected to play a vital role in this case.

8.2 Summary of contribution

This research offers many contributions to the field of ultrasonic TOFD data processing and interpretation. These contributions can be summarised as follows:

a) Proposes for the first time that the mode-converted data can be used to find the depth, length and position of flaws accurately.

b) Proposes for the first time that D-scans can provide sizing accuracy for off-axis flaws that is comparable to that of B-scans, hence reducing the time and cost of inspection and interpretation.

c) Proposes a complete automatic TOFD data interpretation system that relies on D-scans only.

d) Proposes novel methods for flaw detection and characterisations.

e) Proposes outstanding TOFD data pre-processing methods that are based on the use of multi-resolution analysis.

f) Proposes a user-friendly automatic interpretation tool with a graphical user interface that offers many capabilities to the users.

8.3 Future work

During the course of work in this research, several important and potential ideas were originated. These can be integrated with the current findings and lead to further research initiatives. The following is a list of suggestions for further work that are applicable to ultrasonic TOFD:

a) **Application of the proposed automatic method to complex geometries**. This can be achieved by adapting the proposed automatic TOFD techniques to cope with complicated shapes like nozzles, T-joints and thick cylindrical components.

b) **Improving the quality and consistency of the input data through advanced initial processing**. This can be met by considering more compensation for acquisition effects such as the missing scan lines caused by high scanning speed, loss of signal due to lack of couplant and probe-lift off which results in improvements in the subsequent stages.

c) **Advanced defect sizing and positioning techniques:**

- Investigating the relationship between timing measurements and phase relationship between different defect echoes.
- Analysing the defects in orientation by detecting the profile of defect echoes in B-Scan.
- Proposing smart analysis technique of the distinctive hyperbolic signature representation in B-Scan images which can provide valuable sizing information.

d) **Continuing the study of the mode-converted (shear) waves region and its potential:**

- The use of advanced image processing techniques to utilise even further the information in the mode-converted waves area.
- Detecting the profile of start and backwall signals of mode-converted waves area in order to involve it further in the subsequent interpretation stages.
- Achieving a high POD and confirming the existence of defects and automatic segmentation and outlining of defect zones in the mode-converted waves area to benefit from the exceptional resolution for shallow flaws, which may help in detecting some hidden defects in the compressional wave area.
- Involving the analysis of defect signature in the mode-converted waves area which can provide valuable and exceptional information about each defect class.

e) **Enhancing output representation:**

- Generating automatic textual defect report based on one of TOFD standards.
- Providing recommendation to the inspectors (e.g. rescan, further B-scans, increase sampling frequency, choose another probe angle, reduce the PCS...etc.).
- Representing results interpretation and providing mapping of detected defects in 3-D.

- Generating a knowledge base or database that can show and store different defect cases to be used as on-shelf data for training and comparisons.

f) **Commercial implementation of an automatic interpreter**. This can be achieved by implementing the final system in a stand-alone robust software form for an on-site use on a standard portable computer or handheld device. That is, finishing the proposed software prototype introduced before.

g) **TOFD and phased array for raster combined scans:**

- Developing algorithms to process data of a combined scan through the marriage between TOFD and the phased array. This combination provides the scan in a single pass, and hence scanning time will be less. Also, the surface and near-surface defects can be detected in more accuracy, and the focus depth is easily adjustable.
- Applying the idea of sectoral scans (S-scans) which is the ability to scan a complete sector of volume without any probe movement.

h) **Multi-probe TOFD systems**. As more than two probes are likely to be used in future TOFD schemes, it will be necessary to integrate the information from these probes. Image fusion technique is a possible candidate in this regard to interpret the resulting TOFD images.

Bibliography

[1] A Al-Ataby and W Al-Nuaimy. *Advanced signal processing techniques in NDT. In (Applied signal and image processing, multidisciplinary advancements)*, chapter 8, pages 127–146. IGI Global, 2011.

[2] O Zahran. *Automatic ultrasonic Time-of-flight diffraction interpretation, fundamentals and applications*. VDM, 2010.

[3] British Standards Institution. Guide to calibration and setting-up of the ultrasonic time of flight diffraction (TOFD) technique for the detection, location and sizing of flaws. *BS 7706*, December 1993.

[4] Lavender International NDT Ltd. Time-of-flight diffraction. *PCN L2 course theory notes*.

[5] J Charlesworth and J Temple. *Engineering applications of ultrasonic time-of-flight diffraction*. RSP, 2nd edition, 2001.

[6] C Matthews. *ASME engineer's data book*. ASME Press, 2001.

[7] M G Silk and B H Lidington. Defect sizing using an ultrasonic time delay approach. *British Journal of NDT*, 17(2):33–36, March 1975.

[8] M G Silk and B H Lidington. Defect sizing using the time delay of diffracted ultrasound. *Oxidation of Metals*, pages 7–11, 1976.

[9] M G Silk, B H Lidington, and G F Hammond. A time delay approach to crack location and sizing in austenitic welds. *British Journal of NDT*, 22(2):55–61, March 1980.

[10] M G Silk. The propagation of ultrasound in anisotropic weldments. *Materials Evaluation*, 39(5):462–467, April 1981.

[11] M G Silk. The ultrasonic inspection of difficult materials. In *4th European conference on NDT*, pages 1647–1660. Pergamon Press, 1987.

[12] M G Silk. *The capabilities and limitations of NDT*, volume 5, chapter Ultrasonic testing - special techniques. The British Institute of Non-Destructive Testing, December 1988.

[13] M G Silk. Some modern non-destructive testing techniques and thier application. *Quality Assurance*, 4(3):92–97, September 1978.

[14] M G Silk. The propagation of polarised shear waves in steel. United Kingdom Atomic Energey Authority - Harwell AERE-R 9423, The British Institute of Non-Destructive Testing, March 1979.

[15] M G Silk. Defect sizing using ultrasonic diffraction. *British Journal of NDT*, pages 12–15, January 1979.

[16] M G Silk. The fundamental accuracy of ultrasonic time-of-flight testing techniques. *Inistitute of Mechanical Engineering conference publications*, pages 125–133, 1982.

[17] M G Silk. The use of diffraction-based time-of-flight measurements to locate and size defects. *British Journal of NDT*, 26:208–213, May 1984.

[18] M G Silk. Weld inspection methods. *Metals and Materials*, 5(4):192–196, April 1989.

[19] M G Silk. Flaw size distributions in pressure vessels and flaw detection probabilities in NDT. *British Journal of NDT*, 33(10):491–494, October 1991.

[20] American Society of Mechanical Engineering. Asme boiler and pressure vessel code. *Section XI*, Division 1 1983.

[21] L Xu, E Oja, and P A Kultanen. A new curve detection method: randomised Hough transform RHT. *Pattern Recognition Letters*, 11(5):331–338, May 1990.

[22] M G Silk. Benefits of signal processing in ultrasonic inspection. *Insight*, 36(10):776–781, October 1994.

[23] M G Silk. Estimation of the probability of flaw in TOFD data with varing levels of noise. *Insight*, 38(1):31–36, January 1996.

[24] N Trimborn. The time-of-flight-diffraction-technique. *UTonline (www.ndt.net/article/tofd/trimborn/trimborn.htm)*, 2(9), September 1997.

[25] S Mondal and T Sattar. An overview TOFD method and its mathematical model. *NDTnet (www.ndt.net/article/v05n04/mondal/mondal.htm)*, 5(4), April 2000.

[26] B Browne. Time of flight diffraction, its limitation - actual and perceived. *UTonline (http://www.ndt.net/article/tofd/browne/browne.htm)*, 2(2), September 1997.

[27] S Geus, F Dijkstra, and T Bouma. Advances in TOFD inspection. *UTonline (http://www.ndt.net/article/wcndt00/papers/idn073/idn073.htm)*, 2000.

[28] T Just and G Csapo. Ultrasonic crack depth measurement of surface bracking cracks in piping. *UTonline journal(http://www.ndt.net/article/tofd/just/-just.htm)*, 2(9), September 1997.

[29] A Erhard, E Schulz, G Brekow, H Wustenberg, and P Kreier. Critical assessment of the TOFD approach fpr ultrasonic weld inspection. *http://www.ndt.net/article/v03n10/erhard/erhard.htm*, 3(10), October 1998.

[30] A Erhard and U Ewert. The TOFD method between radiography and ultrasonic in weld testing. *http://www.ndt.net/article/v04n09/erhard/erhard.htm*, 4(9), September 1999.

[31] A Hecht. Time of flight diffraction TOFD - an ultrasonic testing method for all application. *UTonline (http://www.ndt.net/article/tofd/hecht/hecht.htm)*, 2(9), September 1997.

[32] P Kreier and G Brekow. Critical argument regarding the European TOFD draft standard. *UTonline (http://www.ndt.net/news/tofd1297/tofd.htm)*, 3(4), April 1998.

[33] B Browne. The stunted growth of TOFD - and its cost to industry. *Insight*, 39(9):658–659, September 1997.

[34] B Browne. TOFD 2 - a case of a little learning. *Insight*, 39(12):908–909, December 1997.

[35] F Betti, G Zappavigna, C Pedrinzani, G Nardoni, and P Nardoni. Accuracy capability of TOFD technique in ultrasonic examination of welds. *UTonline (http://www.ndt.net/article/wcndt00/papers/idn634/idn634.htm)*, 2001.

[36] F Betti, A Guidi, B Raffarta, G Nardoni, P Nardoni, and L Nottingham. TOFD - the emerging ultrasonic computerized technique, for heavy wall pressure vessel welds examination. *UTonline (http://www.ndt.net/article/-v04n09/nardoni/nardoni.htm)*, 9(4), September 1999.

[37] N Trimborn. The performance of the time of flight diffraction (TOFD) technique in various international round robin trails and the continuing research work underway. *UTonline (http://www.ndt.net/article/tofd/silk/silk.htm)*, 3(10), October 1998.

[38] S Webber. Five years of testing using the semi-automated ultrasonic time of flight diffraction system. *UTonline (http://www.ndt.net/article/apcndt01/-papers/898/898.htm)*, 2001.

[39] R Krutzen. Evaluation of currently applied ultrasonic sizing techniques for stress corrosion cracks in steam generator tubes. *17th EPRI Steam Generator NDE Workshop*, August 1998.

[40] S Baby, T Balasubramanian, R J Pardikar, M Palaniappan, and R Subbaratnam. Time-of-flight diffaction (TOFD) technique for accurate sizing of cracks embedded in sub-cladding. *Insight*, 45(9):600–604, September 2003.

[41] S Baby, T Balasubramanian, and R J Pardikar. Estimation of the height of surface breaking cracks using ultrasonic timing methods. *Insight*, 44(11):679–683, November 2002.

[42] S Baby, T Balasubramanian, and R J Pardikar. Time-of-flight diffaction (TOFD) technique for accurate sizing of surface breaking cracks. *Insight*, 45(6), June 2003.

[43] S Lawson. *Automatic defect detection in industerial radioscopic and ultrasonic images*. Phd thesis, The University of Surrey, April 1996.

[44] S Lawson. Artificial neural networks for defect detection. *(http://robots.surrey.ac.uk/activities/NDT/annxray.html)*, 1995.

[45] S Lawson and G Bonser. Ultrasonic time of flight diffraction (TOFD) image processing. *(http://robots.surrey.ac.uk/activities/NDT/tofd.html)*, 1995.

[46] S Lawson and G Bonser. Defect detection of partially complete SAW and TIG welds using the ultrasonic time of flight diffraction method. *SPIE*, 3399(9):161–172, 1998.

[47] S Lawson. Automatic detection of defects in industrial ultrasound images using a neural network. *Proc. of Int. Symposium on Lasers, Optics, and Vision for Productivity in Manufacturing, Vision Systems: Applications*, 2786:37–47, June 1996.

[48] S Lawson. Recent developments for automatic on-line TOFD inspection. *Ultrasonic Testing On-Line Journal, http://www.ultrasonic.de/*, September 1997.

[49] S Lawson. Ultrasonic testing and image processing for in progress weld inspection. *UT online journal (http://www.ndt.net/article/shaun/shaun.htm)*, April 1996.

[50] S Lawson. Final ultrasonic TOFD trails held at Nordon (FR). *(http://robots.surrey.ac.uk)*, October 1997.

[51] L Voon, P Bolland, P Gorria, E Renier, F Truchetet, B Gremillet, and L Pillet. Application of digital image processing techniques in ultrasonic inspection of engineering structures. *Proceeding of the 1998 International Conference on Quality Control by Artificial Vision - QCAV 98, Japan*, pages 521–528, November 1998.

[52] K Maalmi, A El Ouaazizi, R Benslimane, L F C Lew Yan Voon, A Diou, and P Gorria. Detecting parabolas in ultrasound B-scan images with genetic-based inverse voting Hough transform. *IEEE*, pages 3337–3340, 2002.

[53] G Baskaran, K Balasubramaniam, C V Krishnamurthy, and C Lakshmana Rao. Ultrasonic TOFD flaw sizing and imaging in thin plates using embedded signal identification technique (ESIT). *Insight*, 46(9):537–542, September 2004.

[54] G Baskaran, K Balasubramaniam, C V Krishnamurthy, and C Lakshmana Rao. Development of an advanced ultrasonic TOFD system. *Journal of Nondestructive Testing and Evaluation*, 3:24–32, 2004.

[55] G Baskaran, G Swamy, K Balasubramaniam, C V Krishnamurthy, and C Lakshmana Rao. *Application of TOFD technique to thin sections using ESIT and PSCT*, volume 24 of *Review of Progress in QNDT*. AIP Melville, 2004.

[56] G Swamy, G Baskaran, , and B Krishnan. A point source correlation technique for automatic discontinuity identification and sizing using time-of-flight diffraction. *Material Evaluation*, 63(4):425–429, April 2005.

[57] E Moura, M Siqueira, R Silva, J Rebello, and Caloba L. Welding defect patteran recognition in TOFD signals - part 1. linear classifiers. *Insight*, 47(12):777–782, December 2005.

[58] E Moura, M Siqueira, R Silva, and Rebello. Welding defect patteran recognition in TOFD signals - part 2. non-linear classifiers. *Insight*, 42(5):306–311, May 2000.

[59] O Zahran. *Automatic detection, sizing and characterization of weld defects using ultrasonic time-of-flight diffraction*. Phd thesis, University of Liverpool, Liverpool, UK, February 2006.

[60] Y Zhang, Y Wang, M Zuo, and X Wang. Ultrasonic time-of-flight diffraction cracck size identification based on cross-correlation. *Canadian Conference on Electrical and Computer Engineering CCECE*, pages 1797 – 1800, 2008.

[61] A Al-Ataby, W Al-Nuaimy, and O Zahran. Towards automatic flaw sizing using ultrasonic time-off light diffraction. *Insight - Non-Destructive Testing and Condition Monitoring (The Journal of the British Institute of Non-Destructive Testing)*, 52(7):336–371, July 2010.

[62] A Al-Ataby and W Al-Nuaimy. Enhancing the accuracy of off-axis flaw sizing and positioning in TOFD D-scans using mode-converted waves. *NDTMS, Springer, RILEM Bookseries*, Vol. 6, August 2011.

[63] British Standards Institution. Non-destructive testing - ultrasonic examination - part 6: time-of-flight diffraction as a method for detection and sizing of discontinuties. *European prestandard BS EN 583-6*, March 2008.

[64] British Standards Institution. Non-destructive testing of welds - time-of-flight diffraction technique (TOFD) - acceptance levels. *European prestandard BS EN 15617*, April 2009.

[65] International Organization for Standardization. Non-destructive testing of welds - ultrasonic testing - use of time-of-flight diffraction technique (TOFD). *ISO/DIS 10863*, September 2011.

[66] British Standards Institution. Welding - use of time-of-flight diffraction technique (TOFD) for examination of welds. *European prestandard CEN/TS 14751*, November 2004.

[67] American Standards. Standard practice for mechanized ultrasonic examination of girth welds using zonal discrimination with focused search units. *ASTM - E1961-98, 1998.*

[68] American Petroleum Institute (API). Welding of pipelines and related facilities. *API-Standard 1104*, 19th Edition, September 1999.

[69] V Rallabandi. Enhancement of ultrasound images using stochastic resonance-based wavelet transform. *Computerized Medical Imaging and Graphics Journal*, 32:316–320, February 2008.

[70] M Cacciola, F C Morabito, and M Versaci. *Ultrasonic and advanced methods for nondestructive testing and material characterisation*, chapter 21, pages 493–516. World Scientific, 2007.

[71] A Abbate, J Koay, and J Frankel. Signal detection and noise suppression using a Wavelet transform signal processor: application to ultrasonic flaw detection. *IEEE transactions on Ultrasonics, Ferroelectrics, and Frequency Control*, 44(1):14–25, 1997.

[72] F Bettayeb, S Haciane, and S Aoudia. Improving the time resolution and signal noise ratio of ultrasonic testing of welds by the Wavelet packet. *NDT&E International*, 38:478–484, 2005.

[73] A Kechida, R Drai, and A Benammar. Image processing and Wavelet transform for sizing of welds defects using ultrasonic TOFD images. *Acoustics'08*, pages 609–614, 2008.

[74] A L Graps. An introduction to wavelets. *IEEE Computational Sciences and Engineering*, 2(2):50–61, 1995.

[75] V Matz, M Kreidl, and R Smid. Classification of ultrasonic signals. *The 8th International Conference of the Slovenian Society for Non-Destructive Testing*, pages 27–33, September 2005.

[76] M C Robini, I E Magnin, H Cattin, and A Baskurt. Two-dimensional ultrasonic flaw detection based on the wavelet packet transform. *IEEE transactions on Ultrasonics, Ferroelectrics, and Frequency Control*, 44(6):1382–1394, 1997.

[77] E Oruklu and J Saniie. Ultrasonic flaw detection using discrete wavelet transform for NDE applications. *IEEE transactions on Ultrasonics, Ferroelectrics, and Frequency Control*, 2(6):1054–1057, 2004.

[78] K Kaya, N M Bilgutay, and R Murthy. Flaw detection in stainless steel samples using wavelet decomposition. *IEEE ultrasonic symposium*, pages 1271–1274, 1994.

[79] F Bettayeb, T Rachedi, and H Benbartaoui. An improved automated ultrasonic NDE system by wavelet and neuron networks. *Ultrasonics*, 42:853–858, 2004.

[80] R Haralick, K Shunmugam, and I Dinstein. Textural features for image classification. *IEEE Transactions on Systems, Man Cybernetics*, SMC-3(1):610–621, 1973.

[81] M Kociolek, A Materka, M Strzelecki, and P Szczypinski. Discrete wavelet transform derived features for digital image texture analysis. *Proceeding of International conference on Signals and Electronic Systems*, pages 163–168, 2001.

[82] V Kecman. *Learning and soft computing: Support Vector Machines, Neural Networks, and Fuzzy Logic Models*. MIT Press, 2001.

[83] M Friedman and A Kandel. *Introduction to pattern recognition, statistical, structural, Neural and Fuzzy logic approaches*. Machine Perception and Artificial Intelligence. World Scientific, 1999.

[84] F Wong, R Nagarajan, S Yaacob, A Chekima, and N. E. Belkhamza. An image segmentation method using fuzzy-based threshold. *International Symposium on Signal Processing and Its Applications (ISSPA)*, 1:144–147, August 2001.

[85] M G Silk. An evaluation of the performance of the TOFD technique as a means of sizing flaws, with particular reference to flaws with curved profiles. *Insight*, 38(4):280–287, April 1996.

[86] V N Vapnik. *Statistical Learning Theory*. Wiley, 1998.

[87] V N Vapnik. *The Nature of Statistical Learning Theory*. Springer, 2nd edition, 2000.

[88] K M Rajpoot and N M Rajpoot. Wavelets and support vector machines for texture classification. *Proceedings of INMIC 2004, 8th International Multitopic Conference*, pages 328–333, December 2004.

[89] N Cristianini and J Shawe-Taylor. *An introduction to support vector machines and other kernel-based learning methods*. Cambridge University press, 2000.

[90] M Khelil, A Kechida, R Dari, and M Boudraa. Classification of defects by the SVM method and the principal component analysis (PCA). *European Federation for Non-Destructive Testing conference ECNDT 2006, Germany*, September 2006.

[91] B-Y Sun and D-S Huang. Texture classification based on support vector machine and wavelet transform. *Proceedings of the 5th World Congress on Intelligent Control and Automation, Hangzhou, China*, pages 1862–1864, June 2004.

[92] K Huang and S Aviyente. Wavelet feature selection for image classification. *IEEE Transaction on Image Processing*, 17(9):1709–1720, September 2008.

[93] R Lakes. Meaning of Poisson's ratio. *University of Wisconsin, (http://silver.neep.wisc.edu/ lakes/PoissonIntro.html).*

[94] A Al-Ataby and W Al-Nuaimy. Mode-converted waves and D-scans for flaw sizing and characterisation in ultrasonic time-of-flight diffraction (TOFD). *Proceedings of the 50th Annual Conference of the British Institute for Non-Destructive Testing - NDT11, Telford, UK*, 2011.

[95] A Al-Ataby, W Al-Nuaimy, C R Brett, and O Zahran. Automatic detection and classification of weld flaws in TOFD data using wavelet transform and support vector machines. *Insight - Non-Destructive Testing and Condition Monitoring (The Journal of the British Institute of Non-Destructive Testing)*, 52(11):336–371, November 2010.

Appendices

Appendix A

BS 7706 Flaw Types

The British Standard BS 7706 gives an excellent step-by-step guide to the characterisation of TOFD flaw echoes and lists the types of flaws which are generally recognised. The following sections explain the categories that are generally referred to in BS 7706.

A.1 Planar flaws category

This category includes cracks and lack of fusion between the weld and the base surface, and it is very critical [3].

Cracks They could be upper surface, internal or lower surface cracks.

An upper crack (UC) is a crack that is opened to the upper surface or very close to it. It returns only one echo from the bottom tip of the crack (which is 45° out of phase with the lateral wave), while the upper echo is masked in the lateral wave. Upper cracks may appear as a short straight line in the D-scan image, and may

be accompanied by a loss or a weakening of the lateral wave signal. Its depth, height and the phase relationship with respect to the lateral wave can be used to recognise this class, along with some regional features. A B-scan is recommended to determine the accurate height and depth of this class. In D-scans, signals from the near surface region can often be seen better after the backwall (as a shear wave signal in the mode-converted region) because of the lower velocity and the time scales are effectively increased. Figure 1 shows an example of an upper crack.

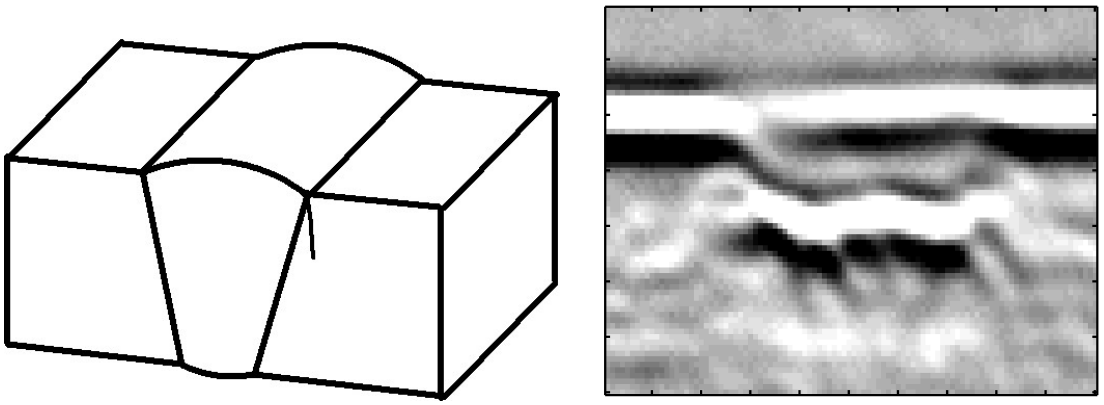

FIGURE 1: Upper crack illustration [2]

For the case of an internal crack (IC), two echoes with a distinct 180° phase difference and some small irregularities can be recognised. The phase of the upper tip echo is 45° out of phase with the backwall echo while the lower one is 45° out of phase with the lateral wave. Internal cracks may appear as two lines above each other in the D-scan image. The defect height, statistical and regional features can be used to recognise this class. Figure 2 shows an example of an internal crack.

A lower crack (LC) is a crack that is opened to the lower surface or very close to it. It returns only one echo from the top tip of the crack (which is 45° out of phase with the backwall echo), while the bottom echo is masked by the backwall signal. Lower cracks do not show any interruption to the backwall echo, and it is very difficult to classify this type of cracks because there are many alternatives (e.g. a

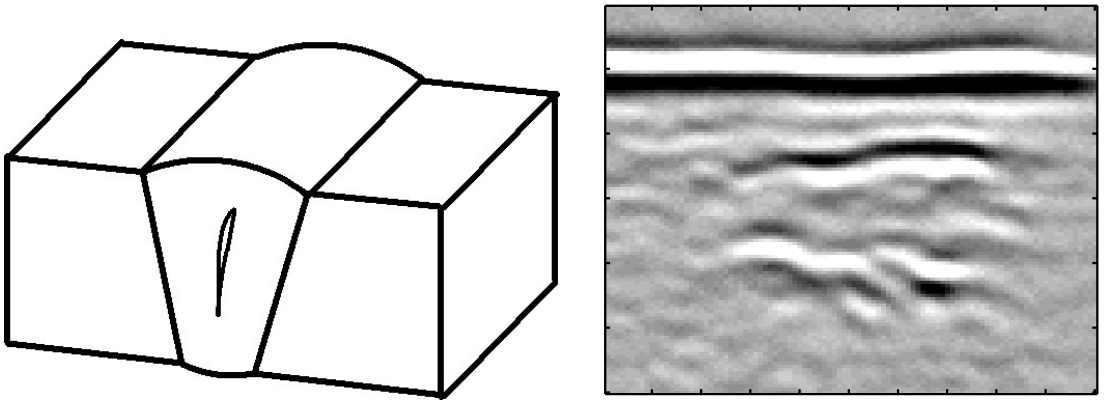

FIGURE 2: Internal crack illustration [2]

slag line or a lack of penetration). Therefore, B-scans are highly recommended to classify and size this defect accurately. Lower cracks may appear as a single line in the D-scan image. The distance from the backwall echo, the defect height, the phase relationship with the backwall wave and the regional features can be used to recognise this class. Figure 3 shows an example of a lower crack.

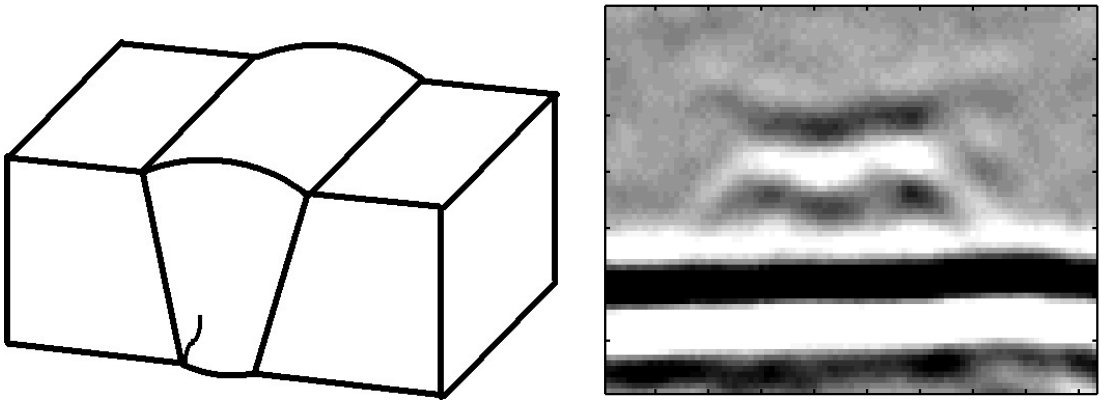

FIGURE 3: Lower crack defect illustration [2]

Lack of fusion Lack of fusion (LOF) is a weld condition when there is no complete fusion between the weld material and the base metal. This may occur mainly because of fast welding, incorrect torch or gun angle or poor edge preparation. LOF looks similar to an internal crack in the D-scan image (two lines above

each other), with the same phase relationship but without irregularities between the two echoes. Both echoes have similar amplitude. The statistical features, the regional features and the defect height can be used to recognise this class. Figure 4 shows an example of a LOF case.

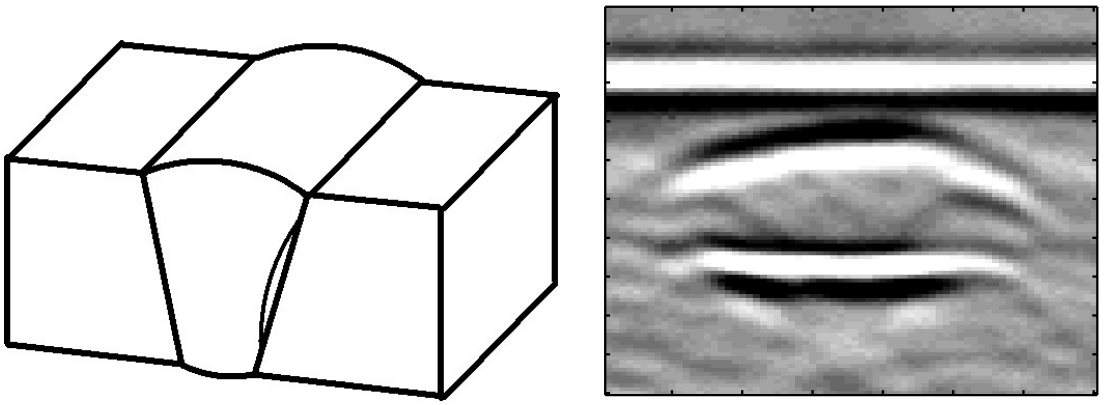

FIGURE 4: LOF defect illustration [2]

A.2 Volumetric flaws category

This category includes lack of penetration and large slag lines.

Lack of penetration Lack of penetration (LOP) is a weld condition when the weld material may not penetrate the entire thickness of the base metal. LOP shows two echoes. There is an unclear 180° phase difference between these two echoes, with the upper tip echo being out of phase with the backwall echo by 45° while the lower one being out of phase with the lateral wave by 45°. The echo from the upper tip is larger in size and much brighter than the echo from the bottom tip. There is more than one defect signature for LOP. The statistical and the regional features can be used to recognise this class. Figure 5 shows an example of LOP case.

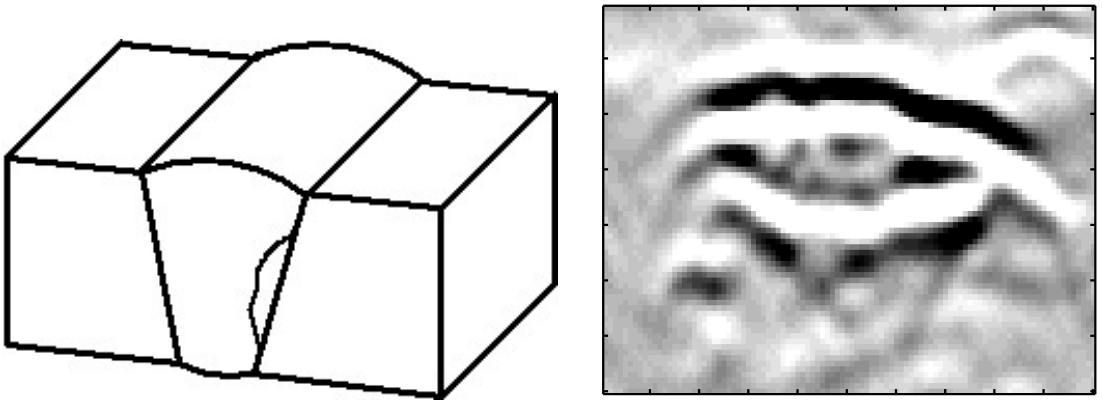

FIGURE 5: LOP defect illustration [2]

Slag lines A slag line (SL) occurs in the weld because the residue after welding process cools and forms a glasslike substance, called a slag, which is trapped in the weld. A SL returns two echoes. There is an unclear 180° phase difference between these two echoes from the top and the bottom tips of the flaw, with the phase of the upper tip echo is out of phase with the backwall echo by 45° while the lower one is out of phase with the lateral wave by 45°. The echo from the upper tip is larger in size and brighter than the echo from the bottom tip. Occasionally, a SL produces a signal of larger amplitude than a crack. There is more than one defect signature for a SL. Sometimes it looks like a straight line or has multiple segmented parts, in which case sizing considers the total length and not for each part. A SL is often reportable beyond a minimum length, and B-scans are recommended to determine the exact length. The statistical and the regional features can be used to recognise this class. Figure 6 shows an example of a SL flaw.

If a small SL is positioned very close to the surface of the material, it shows only one echo in the proximity of the lateral wave similar to an UC (Figure 1) with the exception that it has a phase difference of 135° with the lateral wave. Accordingly, the best way to discriminate this type of defect from an UC is by comparing the

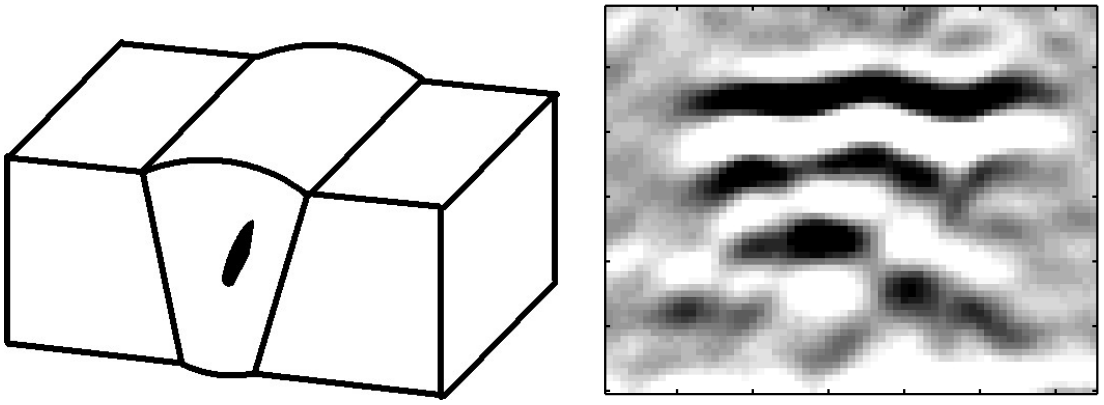

FIGURE 6: SL defect illustration [2]

phase difference with the lateral wave. Figure 7 shows an example of a small surface SL flaw.

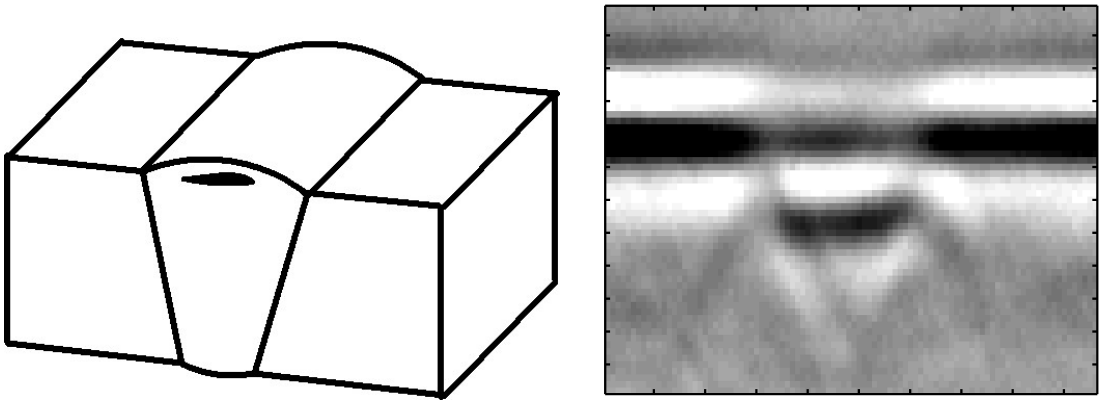

FIGURE 7: Surface SL defect illustration [2]

A.3 Threadlike flaw category

Threadlike (TL) category includes flaws with significant length but little through-wall extent (height). In general, a threadlike flaw shows an upper tip echo and no lower tip (sometimes, the upper and lower tip echoes can be resolved). This echo is 45° out of phase with the backwall echo. Threadlike flaws appear to be a

cluster of point flaws. The geometrical and the statistical features can be used to recognise this class. Figure 8 shows an example of a threadlike defect.

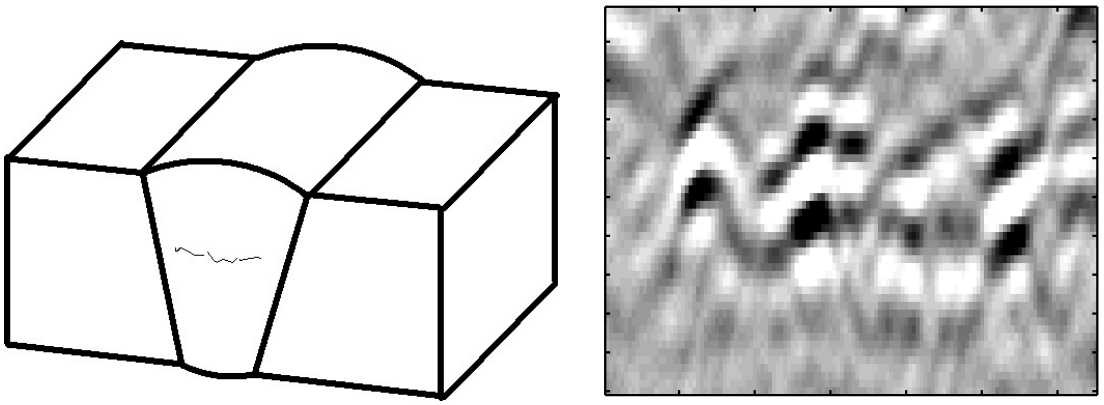

FIGURE 8: Threadlike defect illustration [2]

A.4 Point flaw category

This category includes pores and small pieces of slag which are most common in welds.

Porosity Porosity (PO) is formed due to trapped air or gas bubbles in the metal during welding process that can not escape to the surface of the weld. PO is a cluster of closely pores that have a group of similar echoes with no resolvable length. Each echo shows only the upper tip without the lower tip. This echo is 45° out of phase with the backwall echo. PO pattern is similar to patterns of acoustic noise and appears as a group of small arcs. The regional, the statistical and the geometrical features can be used to recognise this class. Figure 9 shows an example of a PO defect.

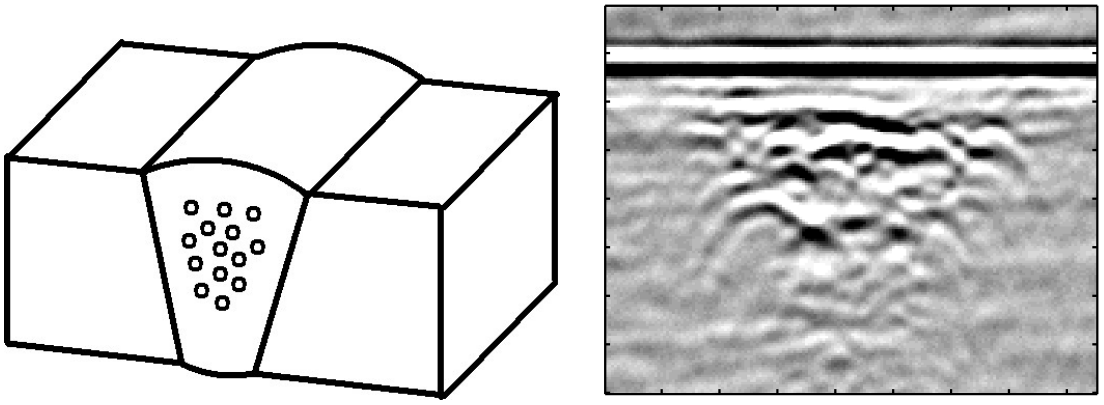

FIGURE 9: PO defect illustration [2]

Small piece of slag or pores Small pieces of slag or small pores produce echoes with no resolvable length. It can be considered as one point flaw which shows only the upper tip echo without a lower tip. This echo is 45° out of phase with the backwall echo. This defect appears as an arc in the D-scan image.

Usually, it is not necessary to report these flaws and they are often eliminated from the final reporting, but associations of such flaws may be reportable in some instances. The regional, the statistical and the geometrical features can be used to recognise this class. Figures 10 and 11 show examples of a small piece of slag and pores defects.

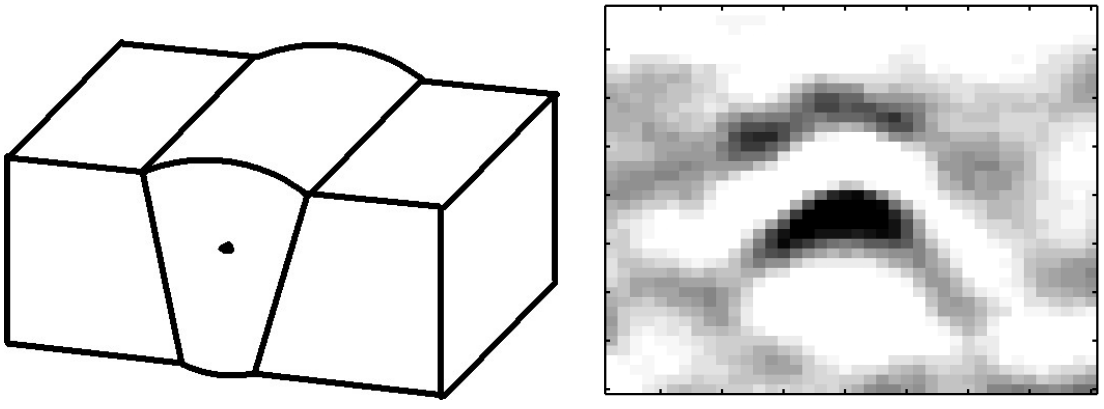

FIGURE 10: Small pieces of slag defect illustration [2]

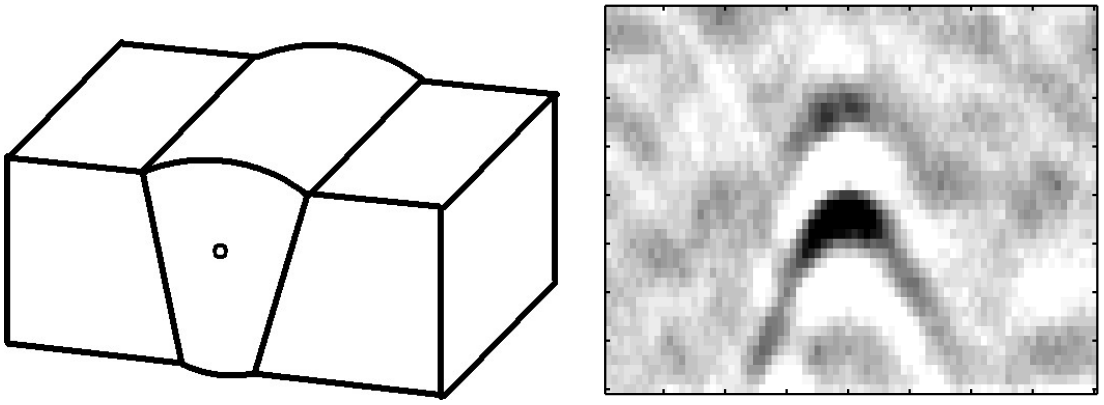

FIGURE 11: Pores defect illustration [2]

A.5 Uncategorised flaws

Flaws may not be categorised by examination. Reasons behind this may be due to flaws with jagged profiles, complex shapes or some other type of reflector. Such indications should be treated as cracks until more detailed examinations can be carried out to confirm their type more precisely [3]. An example of an uncategorised flaw which is classified as an IC is shown in Figure 12.

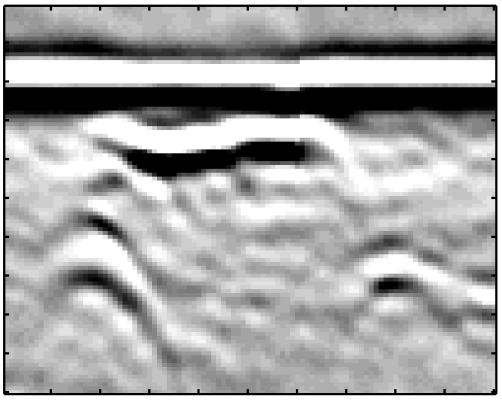

FIGURE 12: Uncategorised defect illustration

Appendix B

The Test Data

The developed algorithms have been applied to a data set of 76 D-scans from steel plates containing 163 weld defects representing different classes, with the majority being off-axis. The D-scans are collected using a 5 MHz TOFD system and 60° probes with 100 MHz sampling frequency. The plates have thicknesses between 20 and 30 mm, with different defect sizes and depths, all characterised and documented by the manufacturer of the steel plates. They are used for training and examination purposes at Lavender International Ltd, UK, and the scans are independently verified by a trained expert using one of the available commercial TOFD software. Figure 13, 14 and 15 show three examples from this data set. A complete list of the data set is as shown in Table 1.

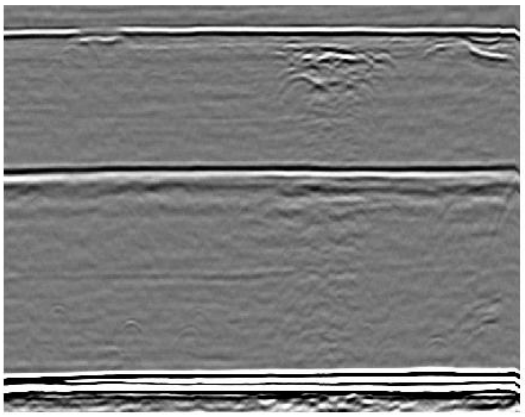

FIGURE 13: Scan sample 1

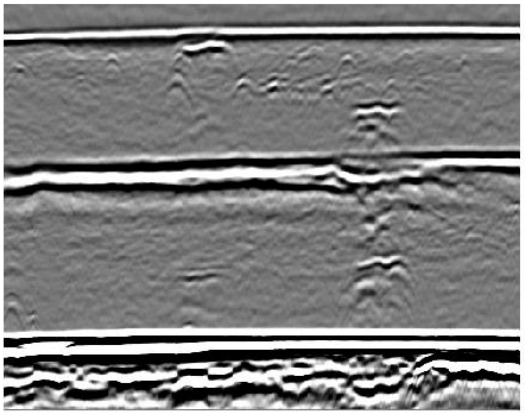

FIGURE 14: Scan sample 2

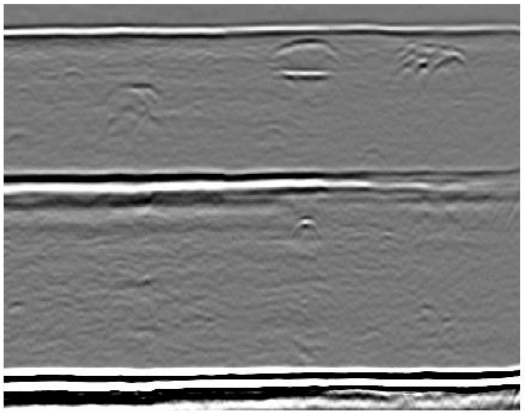

FIGURE 15: Scan sample 3

TABLE 1: Summary of the tested plates

Scan sample	**Plate thickness (mm)**	**Defect 1**	**Defect 2**	**Defect 3**
1	30	UC	PO	SL
2	24	SL	LC	-
3	20	LOF	TL	SL
4	25	SL	SL	-
5	24	PO	-	-
6	20	SL	-	-
7	25	UC	IC	-
8	25	SL	LC	-
9	25	LOF	LOF	SL
10	20	LOP	UC	LOF
11	24	UC	LOF	LOP
12	24	IC	SL	-
13	20	-	LOP	-
14	24	IC	SL	-
15	30	UC	PO	SL
16	24	SL	LC	-
17	20	LOF	TL	SL
18	25	SL	SL	-
19	24	PO	-	-
20	20	SL	-	-

Continued on next page

Table 1 – continued from previous page

Scan sample	**Plate thickness (mm)**	**Defect 1**	**Defect 2**	**Defect 3**
21	25	UC	IC	-
22	25	SL	-	-
23	25	LOF	LOF	SL
24	20	LOP	UC	LOF
25	24	UC	LOF	LOP
26	24	IC	SL	-
27	20	-	LOP	-
28	30	UC	PO	SL
29	24	SL	LC	-
30	20	LOF	TL	SL
31	24	PO	-	-
32	25	UC	IC	-
33	25	LOF	LOF	SL
34	24	UC	LOF	LOP
35	24	IC	SL	-
36	30	UC	PO	SL
37	24	SL	LC	-
38	20	LOF	TL	SL
39	25	SL	SL	-
40	24	PO	-	-
41	20	SL	-	-

Continued on next page

Table 1 – continued from previous page

Scan sample	**Plate thickness (mm)**	**Defect 1**	**Defect 2**	**Defect 3**
42	25	UC	IC	-
43	25	SL	-	-
44	25	LOF	LOF	SL
45	20	LOP	UC	LOF
46	24	UC	LOF	LOP
47	24	IC	SL	-
48	20	-	LOP	-
49	30	UC	PO	SL
50	24	SL	LC	-
51	20	LOF	TL	SL
52	25	SL	SL	-
53	24	PO	-	-
54	20	SL	-	-
55	25	UC	IC	-
56	25	SL	LC	-
57	25	LOF	LOF	SL
58	20	LOP	UC	LOF
59	24	UC	LOF	LOP
60	24	IC	-	-
61	20	-	LOP	-
62	30	UC	PO	SL

Continued on next page

Table 1 – continued from previous page

Scan sample	**Plate thickness (mm)**	**Defect 1**	**Defect 2**	**Defect 3**
63	24	PO	-	-
64	24	IC	SL	-
65	30	UC	PO	SL
66	24	SL	LC	-
67	20	LOF	TL	SL
68	24	PO	-	-
69	25	UC	IC	-
70	25	SL	-	-
71	25	LOF	LOF	SL
72	24	UC	LOF	LOP
73	24	IC	SL	-
74	30	UC	PO	SL
75	24	IC	SL	-
76	24	IC	SL	-